MODELING AND EXPERIMENTAL STUDY OF BULK ACOUSTIC WAVE RESONATOR SENSOR

by

Lifeng Qin

BS, Zhejiang University, P. R. China, 2002

MS, Zhejiang University, P. R. China, 2005

Submitted to the Graduate Faculty of

Swanson School of Engineering in partial fulfillment

of the requirements for the degree of

Doctor of Philosophy

University of Pittsburgh

2010

UNIVERSITY OF PITTSBURGH

SWANSON SCHOOL OF ENGINEERING

This dissertation was presented

by

Lifeng Qin

It was defended on

April 16, 2010

and approved by

Dr. William S. Slaughter, Associate Professor, Department of Mechanical Engineering and Materials Science

Dr. Jeffrey S. Vipperman, Director of Graduate Studies and Associate Professor, Department of Mechanical Engineering and Materials Science

Dr. Patrick Smolinski, Associate Professor, Department of Mechanical Engineering and Materials Science

Dr. Guangyong Li, Assistant Professor, Department of Electrical and Computer Engineering

Dissertation Director: Qing-Ming Wang, Associate Professor, Department of Mechanical Engineering and Materials Science

MODELING AND EXPERIMENTAL STUDY OF BULK ACOUSTIC WAVE RESONATOR SENSOR

Lifeng Qin, PhD

University of Pittsburgh, 2010

Bulk acoustic wave (BAW) resonator as one of the simplest acoustic device, has been proven a most powerful tool for sensor applications with the advantage of precise frequency counting in electronic measurement. Meanwhile, with the improvement of device fabrication and material growth techniques, the resonator can be made with very small size, especially thin film bulk acoustic wave resonators (FBARs) based on ZnO and AlN have been attracted much interest for sensor application due to their high sensitivity induced by high resonance frequency. In this thesis, research focus is on the modeling and experimental study of bulk acoustic wave resonator sensor.

Quartz thickness shear mode (TSM) resonator is adopted to characterize the viscoelastic properties of polymer nanocomposite thin films deposited on the resonators surface. The input electric admittance of multilayer loaded TSM acoustic wave resonator is firstly derived using transfer matrix method by taking into account the acoustic wave impedance of the polymeric layer. Nanocomposite thin films of multi-wall carbon nanotubes (MWCNTs) in copolymers of polyvinylidene fluoride-trifluoroethylene (PVDF-TrFE) are deposited on TSM resonators through spin-on coating processing. The electric impedance spectra of the unloaded and loaded acoustic wave resonators are measured experimentally, and a data fitting approach is applied to extract the properties of the polymer nanocomposites films. It has been found that the thickness of the polymer layer plays a very important role in the extraction of the viscoelastic properties of the films through data fitting, and the reinforcement of the elastic shear modulus of polymer nanocomposite films is not significant.

Quartz TSM resonator is also investigated for in-situ and real time detection of liquid flow rate. A 5MHz TSM quartz resonator is edge-bonded to the sensor mounting port of a special flow chamber with one side exposed to the flowing liquid and other side exposed to air. The fundamental, 3rd, 5th, 7th, and 9th resonant frequency shift due to flow pressure is found to be around 920 (Hz), 3572 (Hz), 5947 (Hz), 8228 (Hz) and 10300 (Hz) for flow rate variation from 0 to 3000 ml/min, which has a corresponding Reynolds number change from 0 to 822. Both theoretical and experimental investigation shows the resonant frequency shifts of different modes are quadratic with flow rate. The results indicate that quartz TSM resonators can be used for flow sensors with characteristics of simplicity, fast response, and good repeatability.

FBARs based on c-axis tilted ZnO and AlN thin films have been theoretically analyzed. Material properties including elastic, dielectric and piezoelectric coefficients, bulk wave properties including acoustic velocity and electromechanical coupling coefficient, and impedance of FBARs are calculated and show strong dependence on the tilt angle of c-axis. Besides 90^0, pure thickness shear mode occurs at 43^0 for ZnO and 46.1^0 for AlN, besides 0^0, pure thickness longitudinal mode occurs at 65.4^0 for ZnO and 67.1^0 for AlN. The electromechanical coupling coefficient of shear mode has a maximum value 13.1% at $\theta=33.3^0$ for ZnO, and 6.5% at $\theta=34.5^0$ for AlN; the maximum electromechanical coupling coefficient of longitudinal mode occurs at $\theta=0^0$ with a value of 8.5% for ZnO, and 6% for AlN. The simulation results show that c-axis tilted ZnO and AlN thin films can provide more options for filter design and sensor application.

TABLE OF CONTENTS

TABLE OF CONTENTS VI

LIST OF TABLES IX

LIST OF FIGURES X

ACKOWLEGEDMENTS XIII

1.0 INTRODUCTION 1

- 1.1 PIEZOELECTRICITY 3
- 1.2 ACOUSTIC WAVE IN ELASTIC MEDIA 5
- 1.3 QUARTZ TSM RESONATOR 6
- 1.4 THIN FILM BULK ACOUSTIC WAVE RESONATOR (FBAR) 14
  - 1.4.1 Basic concept of FBAR 14
  - 1.4.2 Application of FBAR 16

2.0 RESEARCH OBJECTIVE 22

3.0 CHARACTERIZATION OF POLYMER NANOCOMPOSITE FILMS USING QUARTZ TSM ACOUSTIC WAVE RESONATOR 23

- 3.1 INTRODUCTION 23
- 3.2 INPUT ELECTRIC ADMITTANCE OF A FOUR-LAYER TSM RESONATOR 26
- 3.3 MATERIALS AND METHOD 30
  - 3.3.1 Materials preparation and experimental setup 30

3.3.2 Characterization of uncoated TSM resonator sensor 31

3.3.3 Extraction of the complex viscoelastic modulus 33

3.4 RESULTS AND DISCUSSION 34

3.5 CONCLUSION 38

4.0 FLOW SENSOR BASED ON QUARTZ TSM RESONATOR 40

4.1 INTRODUCTION 40

4.2 MATERIAL AND METHOD 43

4.3 METHOD OF FLOW MEASUREMENT 46

4.4 RESULTS AND DISCUSSION 52

4.5 CONCLUSION 62

5.0 ANALYTICAL STUDY OF DUAL MODE RESONATORS BASED ON ZNO AND ALN FILMS WITH TILTED C-AXIS ORIENTATION 63

5.1 INTRODUCTION 63

5.2 THEORY 66

5.2.1 Dual mode FBARs 66

5.2.2 Material properties of ZnO and AlN films 67

5.2.3 Impedance of FBARs 67

5.3 RESULTS AND DISCUSSION 73

5.3.1 Dependence of ZnO and AlN material properties on the tilt angle θ 73

5.3.2 Bulk acoustic wave properties of ZnO and AlN 80

5.3.3 Simulation of electric impedance spectra of FBARs based on c-axis tilted ZnO and AlN films 85

5.3.4 Sensitivity of ZnO and AlN FBAR for mass sensor application 91

5.4 CONCLUSION 99

6.0 CONCLUSIONS AND FUTURE WORK 101

6.1 MAJOR ACCOMPLISHMENTS 101

6.2 FUTURE WORK 103

BIBLIOGRAPHY 106

LIST OF TABLES

Table 1.1. Surface mechanical impedance (Z_L) for different surface perturbations.................... 14

Table 3.1 The effective parameters of quartz thickness shear mode resonator 36

Table 5.1. Material properties of ZnO and AlN.. 79

Table 5.2. Bulk acoustic wave properties of ZnO 83

Table 5.3. Bulk acoustic wave properties of AlN.. 83

Table 5.4. Parameters for calculation of $f_{sL}(\theta)$ and $f_{sS}(\theta)$ 96

Table 5.5. Mass sensitivity of FBAR based on c-axis tilted ZnO... 97

Table 5.6. Mass sensitivity of FBAR based on c-axis tilted AlN.. 98

LIST OF FIGURES

Figure 1.1. A quartz plate is cut with an angle of 35.10 degrees with respect to the optical z-axis. (A) Circular TSM quartz resonator of thickness *dq* coated with electrodes of radius R (B) [3] 6

Figure 1.2. Shear displacement profiles across the Quartz TSM resonator thickness for the fundamental (N=1) and the third harmonic (N=3) resonances [4] 8

Figure 1.3. The Trans mission line presentation. (a) The three-port equivalent circuit of the uncoated quartz crystal. (b) The two-port transmission line of a non-piezoelectric layer. Within the transmission line mode the number of such layers is not restricted (c) [6] 9

Figure 1.4. BVD equivalent circuit of unperturbed TSM resonator near the series resonant frequency (A); Modified BVD circuit of TSM resonators with small loadings (B)..................... 13

Figure 1.5. FBAR (a) the configuration of FBAR [9]; (b) the BVD equivalent circuit of FBAR 15

Figure 1.6. (a) Topology of a ladder filter; (b) Working principle of a ladder filter [12] 17

Figure 1.7. schematic of ZnO FBAR [13] 18

Figure 1.8. (a) frontside photograph ZnO FBAR; (b) backside photograph of ZnO FBAR; (C) schematic setup of FBAR testing [14] 18

Figure 1.9. (a) Cross structure of AlN FBAR; (b) SEM photograph of the etched Si and membrane [15] 19

Figure 1.10. (a) Impedance magnitude vs. frequency for an AlN shear mode FBAR operated in air. Clearly seen are the resonances of the shear mode at 1.25 GHz and the longitudinal mode at 2.15 GHz; (b) Impedance magnitude vs. frequency for an AlN shear mode FBAR operated with one side in contact with water. Clearly seen are the resonances of the shear mode at 1.25 GHz and the almost totally damped longitudinal mode at 2.15 GHz. (c) Schematic illustration of a shear mode FBAR resonator together with a microfluidic transport system [21] 20

Figure 3.1. A schematic four-layer TSM resonator 26

Figure 3.2. Transfer matrix model of TLM for TSM resonator.. 26

Figure 3.3. Schematic of PVDF-TrFE/MWCNTs nanocomposite thin film coating process and experimental setup 30

Figure 3.4. (A) Rel (Y) of uncoated TSM resonator; (B) Img (Y) of uncoated TSM resonator .. 34

Figure 3.5. Rel (Y) of coated TSM resonator; (B) Img (Y) of coated TSM resonator 35

Figure 3.6. (a) Storage modulus of PVDF-TrFE/MWCNTs nanocomposite thin films; (b) Loss modulus of PVDF-TrFE/MWCNTs nanocomposite thin films 38

Figure 4.1. Schematic of flow chamber: (a) Top and bottom plate, (b) Cross section 44

Figure 4.2. The experiment setup for flow rate measurement 44

Figure 4.3. Cross sections of the flow channel: (a) yz plane, (b) xz plane 46

Figure 4.4. The normal pressure difference and wall shear stress versus volumetric flow rate ... 48

Figure 4.5. Deflection of a quartz resonator disk subjected to normal pressure caused by fluid flow: (a) Lateral view, (b) Top view 49

Figure 4.6. Admittance (Y=G+jB) spectrum near fundamental resonant frequency in the air and water: (a) Conductance G; (b) Susceptance B 52

Figure 4.7. Typical electrical admittance (Y=G+jB) spectra of quartz resonator flow sensor: (a) Without average; (b) After 5 time average 53

Figure 4.8. Frequency shift of quartz resonator conductance spectrum under different flow rates (a) 1st mode; (b) 3rd mode; (c) 5th mode; (d) 7th mode; (e) 9th mode. Along the arrow direction, the flow rate increases from 0 to 3000 ml/min, and the conductance spectrum moves from left to right accordingly. 56

Figure 4.9. Resonant frequency shifts of fundamental mode and overtones versus flow rate (a) absolute frequency shift; (b) fractional frequency shift 57

Figure 4.10. Repeatability of fundamental resonant frequency change under nine different flow rate levels 58

Figure 5.1. The schematic of FBAR and coordinate systems. (a) Schematic of FBAR and $(x_1^{'}, x_2^{'}, x_3^{'})$ coordinate system; (b) (x_1, x_2, x_3) coordinate system; (c) the relation of $(x_1^{'}, x_2^{'}, x_3^{'})$ and (x_1, x_2, x_3) coordinate system 66

Figure 5.2. ZnO material properties and effective parameters in $(x_1^{'}, x_2^{'}, x_3^{'})$ coordinate system. (a) $c_{33}^{E'}$, $\overline{c_{33}^{E'}}$, $c_{55}^{E'}$ and $\overline{c_{55}^{E'}}$; (b) $c_{35}^{E'}$ and $\overline{c_{35}^{E'}}$; (c) $\varepsilon_{33}^{S'}$; (d) α; (e) $e_{33}^{'}$ and e_L; (f) $e_{35}^{'}$ and e_S 75

Figure 5.3. AlN material properties and effective parameters in $(x_1^{'}, x_2^{'}, x_3^{'})$ coordinate system. (a) $c_{33}^{E'}$, $\overline{c_{33}^{E'}}$, $c_{55}^{E'}$ and $\overline{c_{55}^{E'}}$; (b) $c_{35}^{E'}$ and $\overline{c_{35}^{E'}}$; (c) $\varepsilon_{33}^{S'}$; (d) α; (e) $e_{33}^{'}$ and e_L; (f) $e_{35}^{'}$ and e_S 78

Figure 5.4. Bulk acoustic wave properties of ZnO. (a) acoustic velocity ; (b) electromechanical coupling coefficient 81

Figure 5.5. Bulk acoustic wave properties of AlN. (a) acoustic velocity ; (b) electromechanical coupling coefficient 82

Figure 5.6. Impedance spectrum simulation of FBAR based on c-axis tilted ZnO film (S: Shear mode, L: Longitudinal Mode). (a) $\theta = 0^0, 15^0, 33.3^0, 43^0$; (b) $\theta = 60^0, 65.4^0, 75^0, 90^0$ 88

Figure 5.7. Impedance spectrum simulation of FBAR based on c-axis tilted AlN film (S: Shear mode, L: Longitudinal Mode). (a) $\theta = 0^0, 15^0, 34.5^0, 46.1^0$; (b) $\theta = 60^0, 67,1^0, 75^0, 90^0$ 90

Figure 5.8. The schematic of FBAR for mass sensor application 91

Figure 5.9. Resonant frequency shift of FBAR based on c-axis tilted ZnO film vs thickness of mass loading. (a) $\theta = 0^0, 43^0, 65.4^0, 90^0$; (b) $\theta = 15^0, 30^0$ 95

Figure 5.10. Resonant frequency shift of FBAR based on c-axis tilted AlN film vs thickness of mass loading. (a) $\theta = 0^0, 46.1^0, 67.1^0, 90^0$; (b) $\theta = 15^0, 30^0$ 96

Figure 6.1. Schematic of a flow sensor based on SAW device 103

Figure 6.2. Schematic of ZnO/AlN FBAR for thin film characterization 105

ACKOWLEGEDMENTS

During my Ph. D. study, I received a lot of help and support from many people in numerous ways. Let me try to thank them without, I hope, forgetting anyone.

First and foremost, I would like to thank my advisor, Dr. Qing-Ming Wang, for supporting me, encouraging me and guiding me throughout my whole Ph. D. study and research work with his brilliant advice, patience and kindness. I am grateful to have an opportunity of being his graduate student to work on piezoelectric material and acoustic wave device, which attracts me much and will continue to play an important role in my future research.

I am very thankful to Dr. William S. Slaughter, Dr. Patrick Smolinski, Dr. Jeffrey S. Vipperman and Dr. Guangyong Li for their kindly consenting to be my committee members, helpful suggestion and useful discussion. I also would like to thank the faculty and staff members in the Department of Mechanical Engineering and Materials Science. It is them who provided me an excellent academic and research environment, which made my studies here valuable and enjoyable.

My thesis could not be possibly completed without the help of my group members. Dr. Hongbin cheng helped me to go through the hard beginning of my research in Pitt. Dr. Qingming Chen gave a lot of help in micro fabrication and useful knowledge on thin film bulk acoustic wave resonator. Dr. Cenglian Sun worked with me on energy harvesting device, which greatly improved my understanding of piezoelectric device. Dr. Fang Li did a great favor in my study of acoustic wave sensor, and her encourage and opinions helped me a lot in my study and research in Pitt. My thanks also go to Zijing Zeng in Mechanical Engineering, who has made a great contribution in the flow sensor design, which was very helpful for my later research.

Special thanks go to Dr. Huinan Liang, my best friend and classmate. Dr. Liang and his wife were always willing to help me out of the difficulties of living and studying in a foreign country.

I also would like to thank all the friends I made at Pitt: Jie Bao, Peng Yuan, Chunhua Fu, Di Xu, Liming Liu, Yunjun Zhao, Fei Gao, Dalong Li, Junhang Luo, Yue Ke, Fei Yan, Guang Xiang, Mengyuan Zhao, and Qian Chen. These people made my life in Pittsburgh easy and happy.

Finally, I reserve my sincere thank to the most important people in my life: my father Peicou Qin, my mother Xianhua Jin, my brother Shunsong Qin and Shunli Qin, who have patiently encouraged and supported me to pursuit higher education for many years. Without you, I could accomplish nothing.

1.0 INTRODUCTION

With the development of acoustic wave technology including bulk acoustic (BAW) and surface acoustic (SAW), advent of novel piezoelectric materials and improvement of fabrication, in the past years acoustic devices have been widely used for frequency stand and filters, underwater sonar, piezoelectric motors and actuators, energy harvesting and vibration reduction, sensor applications and so on. Acoustic wave device are so named because their mechanism is based on mechanical, or acoustic wave. For example, in an acoustic wave sensor, an acoustic wave is excited and propagates through or on the surface of the device; any changes to the characteristics of the wave propagation path affect the velocity and/or amplitude of the wave. Changes in velocity can be monitored by measuring the frequency or phase characteristics of the sensor and can then be correlated to the corresponding physical quantity being measured.

Especially, as one of the simplest acoustic device, BAW resonator is proven to a most powerful tool for sensor application, and has been regarded as the most sensitive sensor platforms that take the advantage of precise frequency counting in electronic measurement. Commonly, a bulk acoustic resonator consists of one thin piezoelectric layer with two metal electrodes deposited on both sides. For sensor application, usually a sensitive layer is coated on the top electrode. When an AC voltage is applied between two electrodes, acoustic waves are generated due to piezoelectricity and travel back and forth in normal direction through the coating layer. Amplitude and phase of the acoustic wave is determined by a set of parameters including the thickness, density and complex shear modulus of the coating layer and the intrinsic properties of uncoated resonator. The electrical impedance of resonator is affected by the superposition of the wave reflected off the boundary to the coating layers and the wave transmitted into the piezoelectric layer through this interface. Resonators become pressure/ force detectors under an applied stress that changes the dynamics of the propagating medium. When specific chemical/physical molecules are adsorbed on the surface of coating layer, they become mass sensors. If the coating layer adsorbs/ reacts with specific biological chemicals in liquids, the resonator becomes a biosensor. Also the resonator can be used to measure materials properties of thin film, when they are coated on the resonator surface.

Of all the acoustic wave sensor configurations, quartz BAW resonator is preferable in many sensor applications due to its high sensitivity, simple structure, and easy interconnection with electronic measurement systems. Quartz resonator originally was used to monitor thin film thickness in the vacuum system or air, where the resonance frequency of resonator is proportional to thin film thickness. With the advent of oscillator circuit, the thickness shear mode (TSM) resonator could be operated in liquid, and widely used as chemical/bio sensor now.

Meanwhile, thin film BAW resonators (FBARs) have attracted a great attention due to the potential applications in the RF and microwave frequency control and signal processing fields. As its name, FBAR has one very thin piezoelectric layer with thickness ranging from several micrometres down to tenth of micrometres, which makes the resonance frequency of FBAR roughly 100 MHz to 10 GHz or even more. PZT, AlN and ZnO thin films are the most popular piezoelectric materials for FBARs designs and applications due to their excellent piezoelectric and mechanical material propertie. Especially AlN thin films with high acoustic velocity and low insertion loss are perfect materials for high frequency resonators and bandpass filters. An important application of FBAR is radio frequency (RF) filter for use in cell phones and other wireless communication system. The filters can be made of FBARs in half-ladder, full-ladder, lattice or stacked topologies and are designed to remove unwanted frequencies signal. FBARs also can be used by microwave oscillators and sensor applications.

In this dissertation, we did two parts of work. The first part was experimentally investigation of quartz BAW resonator for new sensor applications, and the second part was theoretical analysis of FBARs based on ZnO and AlN. In this chapter, background information on these two topics will be briefly introduced.

1.1 PIEZOELECTRICITY

Piezoelectricity is one property of some materials, where an electric potential is generated through an onset of electrical polarization when it is subject to mechanical stress, and a deformation (strain) is produced when an electrical filed is applied. The first case is termed the direct piezoelectric effect, and the second is termed inverse piezoelectric effect. Piezoelectricity is intimately attributed to the crystal structure of materials. For the materials without a center of inversion symmetry, the distribution of the charge on the atoms and bonds in the crystal due to the applied stress/strain will be changed, thus a net electrical polarization is induced. When it is applied an electrical field, the crystal is strained to keep the balance between the coulomb forces and the elastic restoring forces.

The relations between electrical and mechanical variables need to be addressed for operation and design of piezoelectric sensors. For this sake, the piezoelectric constitutive equations have been well developed and they can be written as follow [1]:

$$\begin{cases} S = \left[s^E\right]T + \left[d\right]^T E \\ D = \left[d\right]T + \left[\varepsilon^T\right]E \end{cases} \tag{1.1a}$$

$$\begin{cases} S = \left[s^D\right]T + \left[g\right]^T D \\ E = -\left[g\right]T + \left[\beta^T\right]^T D \end{cases} \tag{1.1b}$$

$$\begin{cases} T = \left[c^E\right]S + \left[e\right]^T E \\ D = \left[e\right]S + \left[\varepsilon^S\right]E \end{cases} \tag{1.1c}$$

$$\begin{cases} T = \left[c^D\right]S - \left[h\right]^T D \\ E = -\left[h\right]S + \left[\beta^s\right]D \end{cases} \tag{1.1d}$$

where the matrixes with superscript "$^{\mathrm{T}}$" is transpose of these matrixes, T is the stress tensor, S is the strain tensor, D is the electrical displacement tensor, and E is the electric-field intensity tensor. c^D and c^E are the stiffness coefficient tensors under the condition of a constant electric displacement and electric-field intensity, respectively; s^D and s^E are compliance coefficient tensors under the condition of a constant electrical displacement and electric-field intensity, respectively; h is the piezoelectric charge coefficient tensor; d is the piezoelectric strain coefficient tensor; g is the piezoelectric voltage coefficient tensor; e is the piezoelectric stress coefficient tensor; ε^T and ε^S are permittivity tensors under the condition of a constant stress and strain respectively; and β^T and β^S are permittivity tensors under the condition of a constant stress and strain respectively. These parameters are related by

$$d_{mi} = \varepsilon^T_{nm} g_{ni} = s^E_{ji} e_{mj} = \varepsilon^S_{nm} s^E_{ji} h_{nj} \tag{1.1e}$$

1.2 ACOUSTIC WAVE IN ELASTIC MEDIA

Since acoustic wave device is based on the transduction mechanism between electrical and acoustic energies, it is necessary to understand the acoustic wave propagation in the device, which commonly has both piezoelectric and non-piezoelectric materials. Based on the Newton's second law of motion and the elastic constitutive equation, the wave equation for a non-piezoelectric solid can be derived as follow [2]:

$$C_{ijkl}u_{k,li} + \eta_{ijkl}\dot{u}_{k,li} = \rho_m \ddot{u}_j \tag{1.2}$$

where C_{ijkl} and η_{ijkl} are the fourth-rank elastic coefficient tensor and the fourth-rank viscoelastic coefficient tensor.

For piezoelectric materials, the wave equation becomes

$$e_{ijk}\varphi_{,ki} + C_{ijkl}u_{k,li} + \eta_{ijkl}\dot{u}_{k,li} = \rho_m \ddot{u}_j \tag{1.3}$$

where e_{ijk} is the third-rank piezoelectric stress coefficient tensor.

From the equation (1.2) and (1.3) we can see that the wave propagation is affected by the material properties including the density, elastic coefficient and viscosity. The material properties can be changed by many factors such as temperature, external force and the adsorption of external material, which make the acoustic wave sensor capable to measure a lot of input. Generally these equations combined with boundary conditions are used to solve the wave propagation in the acoustic wave sensor and model the sensor performance. However it is not easy to solve, especially when the material is anisotropic and the propagation is in an arbitrary direction. Thus, in the sensor design, the size of sensor structure is commonly designed to reduce the problem in low dimensions and the sensor materials are chosen to make the wave propagation in a certain direction. For example, for AT-quartz TSM resonators, the ratio between the lateral dimensions and the thickness is so high that the physical properties can be assumed to constant along the lateral directions of the resonator. Thus, it can be simplified to a one-dimension problem: the generated acoustic wave can be thought to just have one mode (shear wave), and it propagates along the thickness direction.

1.3 QUARTZ TSM RESONATOR

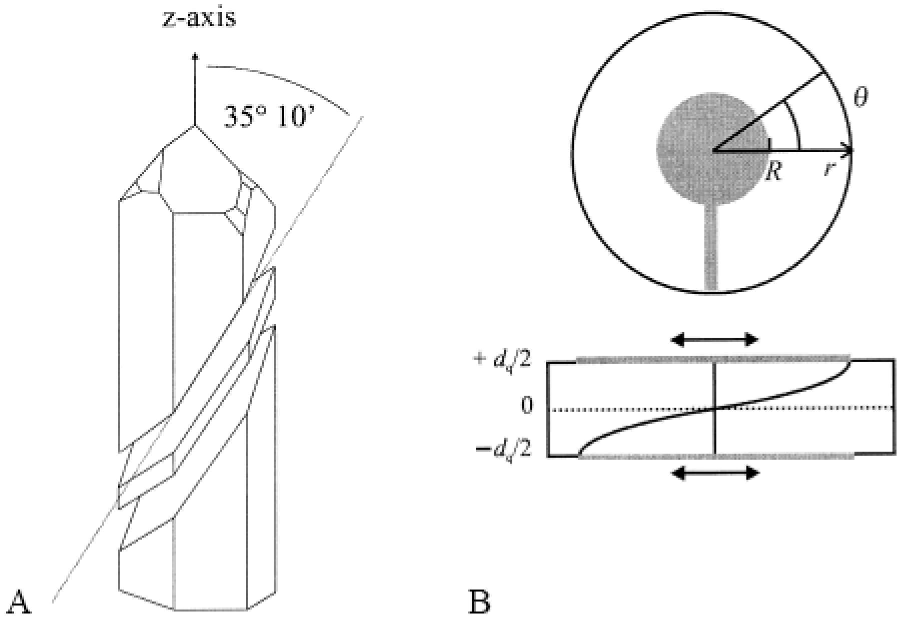

Figure 1.1. A quartz plate is cut with an angle of 35.10 degrees with respect to the optical z-axis. (A) Circular TSM quartz resonator of thickness *dq* coated with electrodes of radius R (B) [3]

Due to the piezoelectricity, when a voltage is applied on a piece of quartz crystal, a stress is produced, and if the voltage is alternating with a certain frequency, the crystal will begin vibrating and produce a steady signal. The mode of vibration depends upon the way the crystal was cut, i.e., an X cut exhibits an extensional vibration mode. For the AT-cut which is cut at 35.10 degrees off the optical z-axis (Figure 1.1 A), the application of a voltage between the two electrodes produces a shear deformation in plane with the crystal surface (Figure 1.1 B), which shows the common structure of a quartz TSM resonator: one layer AT-cut quartz with two thin electrodes; and for the alternative voltage, shear waves of opposite polarity are generated at the either side of the crystal. It is well known that mechanical resonance is the tendency of a mechanical system to absorb more energy when the frequency of its oscillations matches the system's natural frequency of vibration (resonance frequency or resonant frequency) than it does at other frequencies. The resonant condition for the TSM resonator can be determined by tracing the path of one propagating shear wave, which may be thought to start at the top electrode, propagate through the thickness of the quartz thickness, reflect at the bottom surface with phase shift of π, and then return to their origin where it reflects again with phase shift of π. Therefore, the resonant frequency is expressed as [2]:

$$f_N = Nv_s / 2d_q \tag{1.4}$$

$$v_s = (\mu_q / \rho_q)^{1/2} \tag{1.5}$$

where N: odd integers, d_q: thickness of resonator, μ_q: shear stiffness and ρ_q: mass density of resonator. The profile of shear wave is shown in Figure 1.2 [4].The maximum values of the displacement occurs at the crystal surface, which makes the device sensitive to surface perturbations. When a rigid and thin film is coated on the quartz TSM resonator, the resonant frequency shift (Δf_s) due to the deposited mass can be precisely described by Sauerbrey equation [5]:

$$\Delta f_N = \frac{2 f_N^2}{NA\sqrt{\rho_q \mu_q}} \Delta m \tag{1.6}$$

where Δm is mass change; and A is area between two electrodes. This equation is the principle base of quartz TSM resonator for mass sensor application, which has been widely used in vacuum and air. However, Sauerbrey's equation only applies to systems where the following three conditions are satisfied: the deposited mass must be very rigid, the deposited mass must be distributed evenly and the frequency change should be less than 0.05.

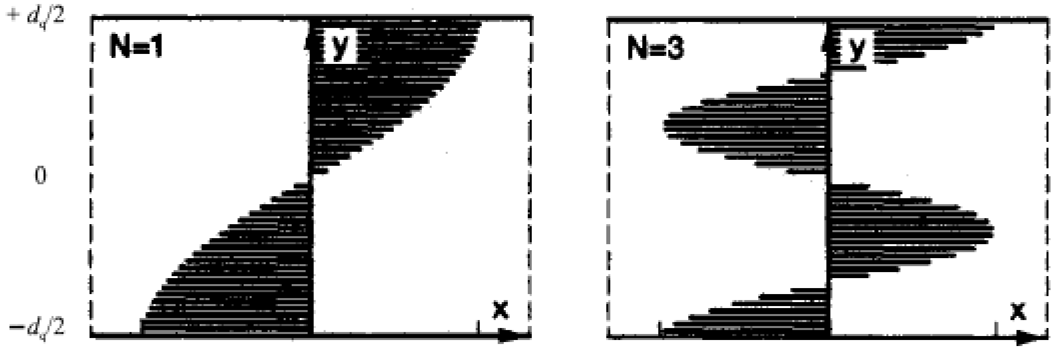

Figure 1.2. Shear displacement profiles across the Quartz TSM resonator thickness for the fundamental (N=1) and the third harmonic (N=3) resonances [4]

Since it only extracts the mass information from Sauerbrey equation, in order to fully exploit the capability of TSM resonator, it is necessary to look at conversion between the mechanical and electric parameters, considering the mechanical resonances are electrically excited. So far, two types of models are used to describe the resonators: the distributed or transmission line model, and the lumped-element model.

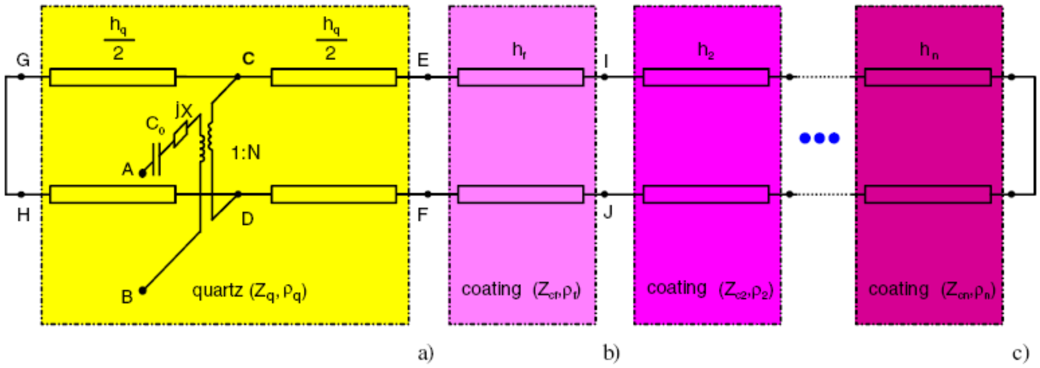

Figure 1.3. The Transmission line presentation. (a) The three-port equivalent circuit of the uncoated quartz crystal. (b) The two-port transmission line of a non-piezoelectric layer. Within the transmission line mode the number of such layers is not restricted (c) [6]

A transmission line model (TLM) is based on a one-dimensional electromechanical model of acoustic wave generation and propagation in piezoelectric and non-piezoelectric layers [6]: A piezoelectric material is described by a three-port element, one electric port and two acoustic ports. KLM model [7] is one of representations of TLM, which is presented in Figure 1.3(a) for quartz resonator:

$$jX = \frac{1}{j\omega C_0}\frac{K^2}{\alpha}\sin\alpha \tag{1.7a}$$

$$\frac{1}{N^2} = \frac{1}{\omega C_0}\frac{4K^2}{\alpha}\frac{1}{Z_{cq}}\sin^2\frac{\alpha}{2} \tag{1.7b}$$

$$Z_{AB} = \frac{1}{j\omega C_0} + jX + \frac{1}{N^2}Z_{CD} \tag{1.7c}$$

$$K^2 = \frac{e_q^2}{\varepsilon_q c_q} \tag{1.7d}$$

$$\alpha = \omega h_q\sqrt{\rho_q / c_q} \tag{1.7e}$$

$$Z_q = \sqrt{\rho_q c_q} \tag{1.7f}$$

$$C_0 = \varepsilon_q \frac{A}{h_q} \tag{1.7g}$$

$$e_q \equiv e_{26} \tag{1.7h}$$

$$\varepsilon_q \equiv \varepsilon_{22} \tag{1.7i}$$

$$c_q \equiv c_{66} + \frac{e_{26}^2}{\varepsilon_{22}} + j\omega\eta_q \tag{1.7j}$$

where K^2 is the electromechanical coupling coefficient of quartz, α is the acoustic phase shift in the quartz crystal and Z_q is the characteristic acoustic impedance of the quartz crystal, Z_{AB} is the impedance at port A and B, Z_{CD} is the acoustic signal at port CD. C_0 is the static quartz crystal capacitance. c_{66} , e_{26} and ε_{22} are the components of the material property tensors for mechanical stiffness, piezoelectric constant and permittivity, respectively, η_q is the quartz viscosity, and the index has been replaced by q to denote material properties of the quartz crystal.

For a common case (shown in Figure 1.3(c)), the resonator is loaded on one side, one acoustic port is considered as a short circuit and the other acoustic port is loaded with acoustic impedance Z_{EF} . After some calculation, the input electric impedance of resonator can be obtained as

$$Z = Z_{AB} = \frac{1}{j\omega C_0}\left(1 - \frac{K^2}{\alpha}\frac{2\tan\frac{\alpha}{2} - j\frac{Z_L}{Z_q}}{1 - j\frac{Z_L}{Z_q}\cot\alpha}\right) \tag{1.8a}$$

$$Z_L = Z_{EF} \tag{1.8b}$$

According to TLM mode, the acoustic impedance transformation performed with layer *i* can be written as follows:

$$Z_i = Z_{ci} \frac{Z_{i+1} + j\sqrt{\rho_i G_i}\tan(\omega\sqrt{\frac{\rho_i}{G_i}}h_i)}{Z_{ci} + jZ_{i+1}\tan(\omega\sqrt{\frac{\rho_i}{G_i}}h_i)} \tag{1.9a}$$

$$Z_{ci} = \sqrt{\rho_i G_i} \tag{1.9b}$$

where ρ_i is the density, G_i is the shear modulus and Z_{ci} is the characteristic impedance of layer *i*. G_i is a complex value in the case of a coating with viscoelastic properties: $G_i = G_i^{'} + G_i^{"}$, where $G_i^{'}$ is the so-called shear storage modulus accounting for acoustic energy storage and $G_i^{"}$ is the shear loss modulus accounting for acoustic energy dissipation. The overall acoustic impedance Z_L or Z_{EF} is equal to $Z_i\left(i=1\right)$.

The electrical impedance can be separated into a parallel circuit consisting of the static capacitance C₀ and motional impedance Z_m . According to equation (1.8), the motional impedance Z_m can be written as follows:

$$Z_m = \frac{1}{j\omega C_0}\left(\frac{\frac{\alpha}{K^2}}{2\tan\frac{\alpha}{2}} - 1\right) + \frac{1}{\omega C_0}\frac{\alpha}{4K^2}\frac{Z_L}{Z_q}\frac{1}{1 - j\frac{Z_L}{Z_q \times 2\tan\frac{\alpha}{2}}} = Z_m^0 + Z_m^L \tag{1.10}$$

Z_m^0 and Z_m^L represent the unloaded quartz and the load respectively. By taking the approximation of $\tan\frac{\alpha}{2} \approx 4\alpha / ((N\pi)^2 - \alpha^2)$, the unloaded quartz near the resonant frequency is expressed as

$$Z_m{}^0 = \frac{1}{j\omega C_q} + j\omega L_q + R_q \tag{1.11a}$$

$$C_q = \frac{8Ae_q^2}{\pi^2 h_q c_{q0}} \frac{1}{1 - \frac{8K_0^2}{\pi^2}} \tag{1.11b}$$

$$L_q = \frac{\rho_q h_q^3}{8Ae_q^2} \tag{1.11c}$$

$$R_q = \frac{\eta_q \pi^2}{8C_0 K_0^2 c_{q0}} \tag{1.11d}$$

where c_{q0} and K_0^2 is the form of c_q and K^2 ignoring loss. For small loads ($\frac{Z_L}{Z_q} << 2\tan\frac{\alpha}{2}$), Z_m^L simplifies to

$$Z_m{}^L = \frac{1}{\omega C_0} \frac{\alpha}{4K^2} \frac{Z_L}{Z_q} \tag{1.12}$$

Therefore, for resonators with small loadings, TLM can be transformed into the equivalent circuit with lumped elements near the resonance frequency, which is called Butterworth-Van-Dyke (BVD) circuit (Figure 1.4). For the real application, the parasitic capacitor (C_{ex}) due to the test fixture should be considered. Thus, we use $C_0^* = C_0 + C_{ex}$ instead of C_0.

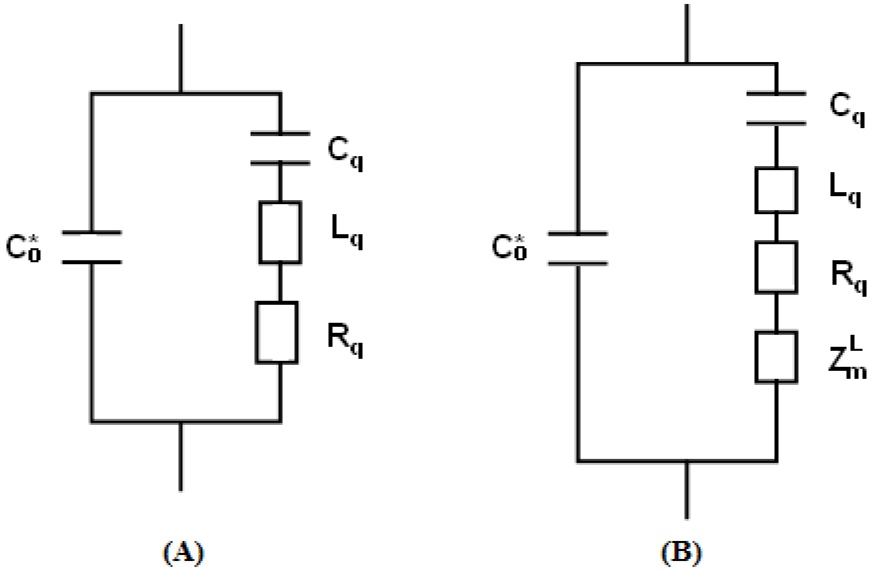

Figure 1.4. BVD equivalent circuit of unperturbed TSM resonator near the series resonant frequency (A); Modified BVD circuit of TSM resonators with small loadings (B)

Resonance frequency is an important parameter for sensor application. The quartz resonator has two important resonance frequencies: The series resonant frequency f_s and the parallel resonance frequency f_p; f_s is defined as the frequency at which the motional reactance is zero, and f_p is defined as the frequency at which the total reactance is zero.

For an unperturbed resonator, f_s and f_p are given

$$f_s = \frac{1}{2\pi (L_q C_q)^{1/2}} \tag{1.13a}$$

$$f_p = \frac{1}{2\pi}\left[\frac{1}{L_q}\left(\frac{1}{C_q} + \frac{1}{C_0 *}\right)\right]^{1/2} \tag{1.13b}$$

For the real measurement, the series resonance frequency is obtained by measuring maximum of the in-phase electrical admittance of the resonator, while the parallel resonance frequency is the characteristic frequency obtained by using the active oscillator.

Equation (1.8) shows the relationship between the input electrical impedance of the resonator and the surface mechanical impedance of the loadings. As shown in Table 1.1, different surface perturbations have different surface mechanical impedance (Z_L). On the other hand, using equation (1.8) and the expression of Z_L, we can extract the acoustic properties of coating systems such as mass of rigid thin film, viscosity of liquid or viscoelastic properties of polymer thin films

Table 1.1. Surface mechanical impedance (Z_L) for different surface perturbations

Surface perturbation	Surface mechanical impedance (Z_L)
Unperturbed	0
Ideal mass layer	$j\omega\rho_s$
semi-infinite Newtonian liquid	$(\omega\rho_L\eta_L/2)^{1/2}(1+j)$
Rigid mass + semi-infinite Newtonian liquid	$j\omega\rho_s+(\omega\rho_L\eta_L/2)^{1/2}(1+j)$
semi-infinite viscoelastic layer	$(G\rho_f)^{1/2}$
Finite viscoelastic layer	$(G\rho_l)^{1/2}\tanh(\gamma h_f)$

1.4 THIN FILM BULK ACOUSTIC WAVE RESONATOR (FBAR)

1.4.1 Basic concept of FBAR

The concept of FBAR was firstly proposed by Lakin and Wang in 1981[8]. FBAR is very simple, in the form of a sandwich structure which has a piezoelectric material for the dielectric layer and suitable top and bottom metal electrodes [9], shown in Figure 1.5(a). The two surfaces of FBAR are exposed to air. It makes the excited wave to be reflected at the surfaces, and the main energy is trapped in the piezo layer, which is helpful to maintain high quality factor Q of resonator. The theory of acoustic wave resonator is still applicable to FBAR. However, to use equation (1.4) for determination of the resonance frequency should be more careful because the thickness of the piezoelectric film is only a few microns, the effect of the electrodes and support layers are considerable increased in the performance of the resonator [10].

The BVD equivalent circuit of FBAR (shown in Figure. 1.5(b)), is same with the unperturbed quartz resonator. C_0 is the geometric capacitance of the structure, R_m, L_m and C_m is called the "motional arm," which counts for the motional loss, the inertia and the elasticity respectively. The piezoelectric layer for FBAR is usually made of ALN, ZnO or PZT. Especially AlN is the preferred material for FBAR due to its electro-mechanical and piezoelectric properties, and the compatibility with CMOS. In addition, wurtzite GaN recently also has been investigated for FBAR fabrication as a new exciting piezoelectric material [11].

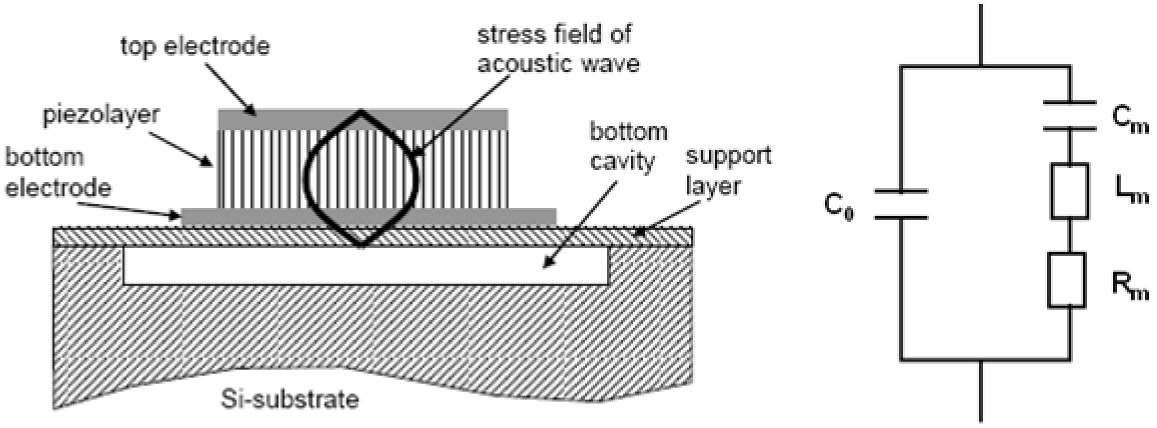

(a) **(b)**

Figure 1.5. FBAR (a) the configuration of FBAR [9]; (b) the BVD equivalent circuit of FBAR

1.4.2 Application of FBAR

An important application of FBAR is radio frequency (RF) filter for use in cell phones and other wireless communication system, including ladder filters, lattice filters, stacked crystal filters (SCF), and coupled resonator filters (CRF). These filters are designed to remove unwanted frequencies signal, while allowing other specific frequencies to be received and transmitted. For example, the ladder filters (Figure 1.6(a)) consist of multiple stages, and each stage is composed of one series resonator and one shunt resonator. Figure 1.6(b) shows the working principle of the ladder filters. f_{detune} is the parallel resonance frequency difference between series resonator and shunt resonator. In the center of the pass band, the impedance of the series resonator is small which allow the RF signal to pass by. On the other hand, the shunt resonator has large impedance which will prevent the signal passing by.

FBARs also have been developed for sensor applications. Gabl et al. [13] presented a biosensor system based on 2GHz longitudinal-mode ZnO FBARs for DNA and protein molecules detection, shown in Figure 1.7; these sensors showed much higher sensitivity and resolution comparable to quartz crystal microbalances. It should be pointed out that it is a little different with FBAR structure (Figure 1.5); here acoustic mirror made of several layers with alternating values of high and low acoustic impedance and a thickness equivalent to quarter wavelength at the main resonance, is designed to reflect the acoustic wave into piezo layer, which can achieve similar performance with air structure while simplifying the fabrication process. This kind of resonators is usually namely solidly mounted resonators (SMRs).

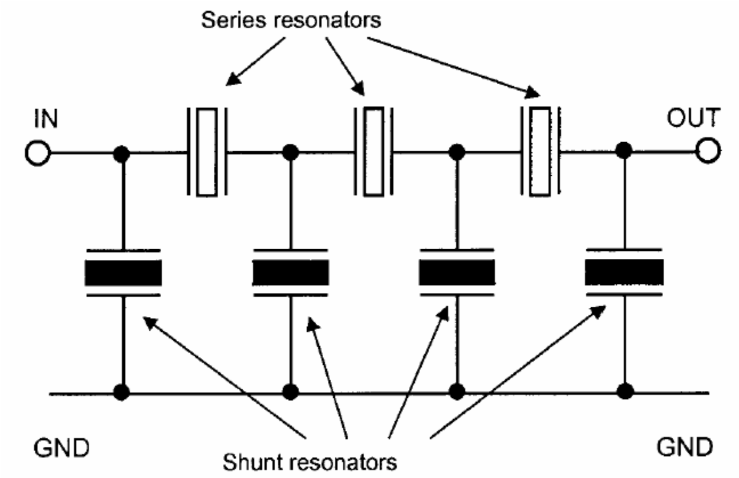

(a)

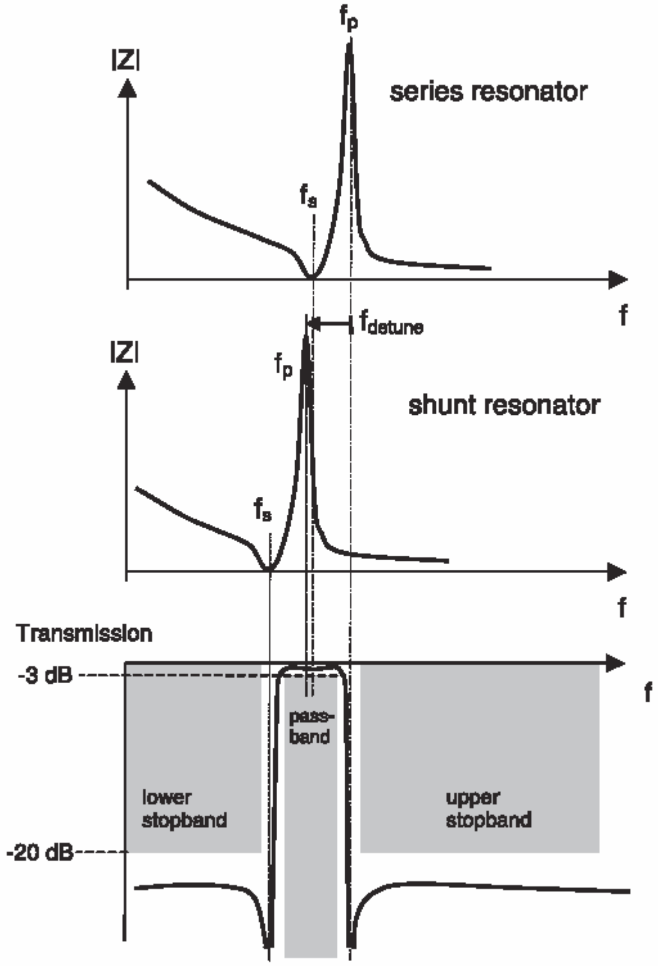

(b)

Figure 1.6. (a) Topology of a ladder filter; (b) Working principle of a ladder filter [12]

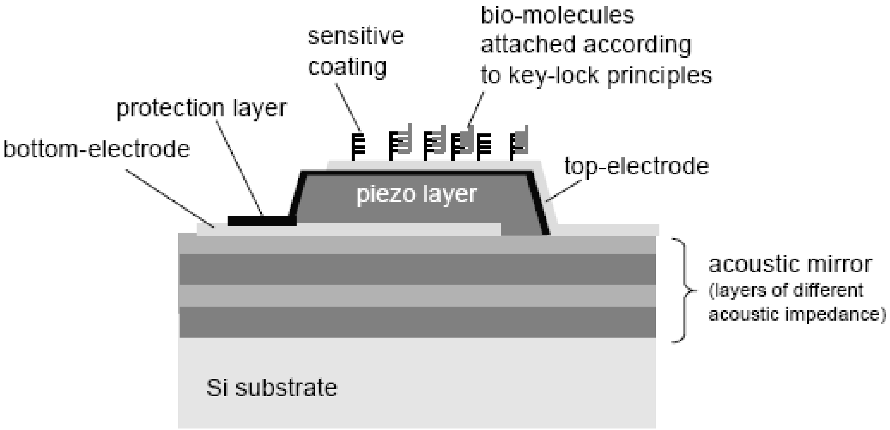

Figure 1.7. schematic of ZnO FBAR [13]

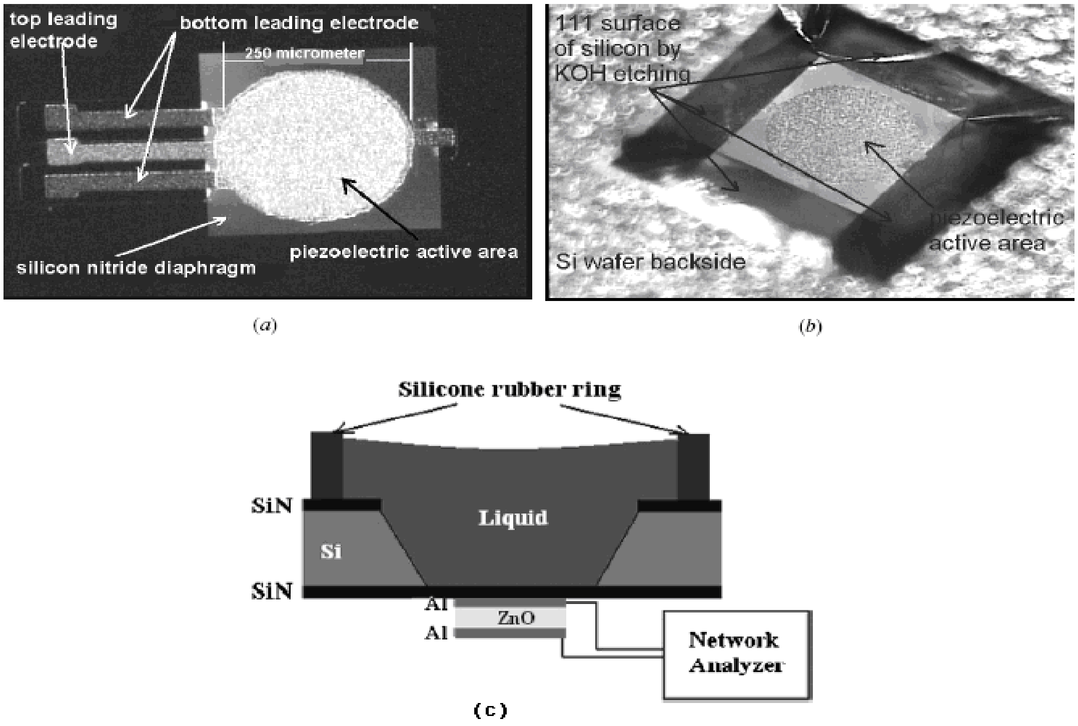

Figure 1.8. (a) frontside photograph ZnO FBAR; (b) backside photograph of ZnO FBAR; (C) schematic setup of FBAR testing [14]

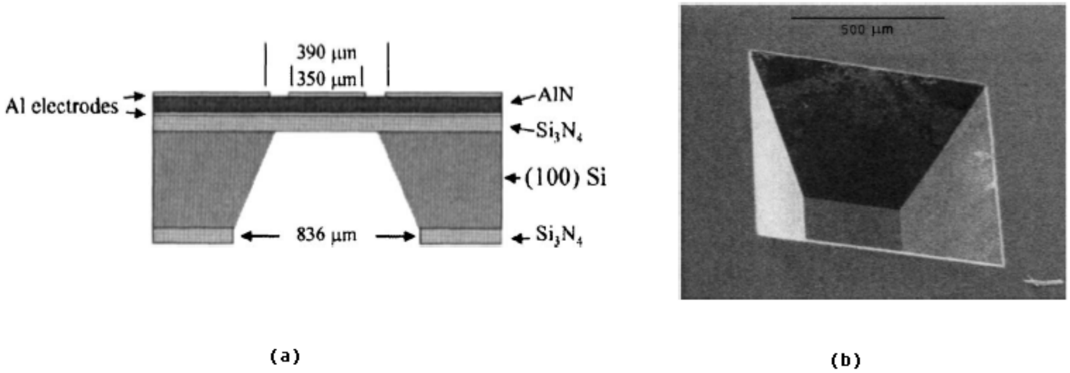

Figure 1.9. (a) Cross structure of AlN FBAR; (b) SEM photograph of the etched Si and membrane [15]

Zhang [14] et al. investigated the effects of liquid nature and conductivity on ZnO FBARs, and TiO2 coated ZnO FBARs with high mass sensitivity were fabricated for metal ion Hg+ detection in liquid environment (shown in Figure 1.8). Benetti et al. [15] reported a chemical sensor based on AlN FBAR (shown in Figure 1.9) with resonance frequency around 1.6 GHz, which was used to detect low concentrations of H_2, CO and ethanol with a fast and repeatable response.

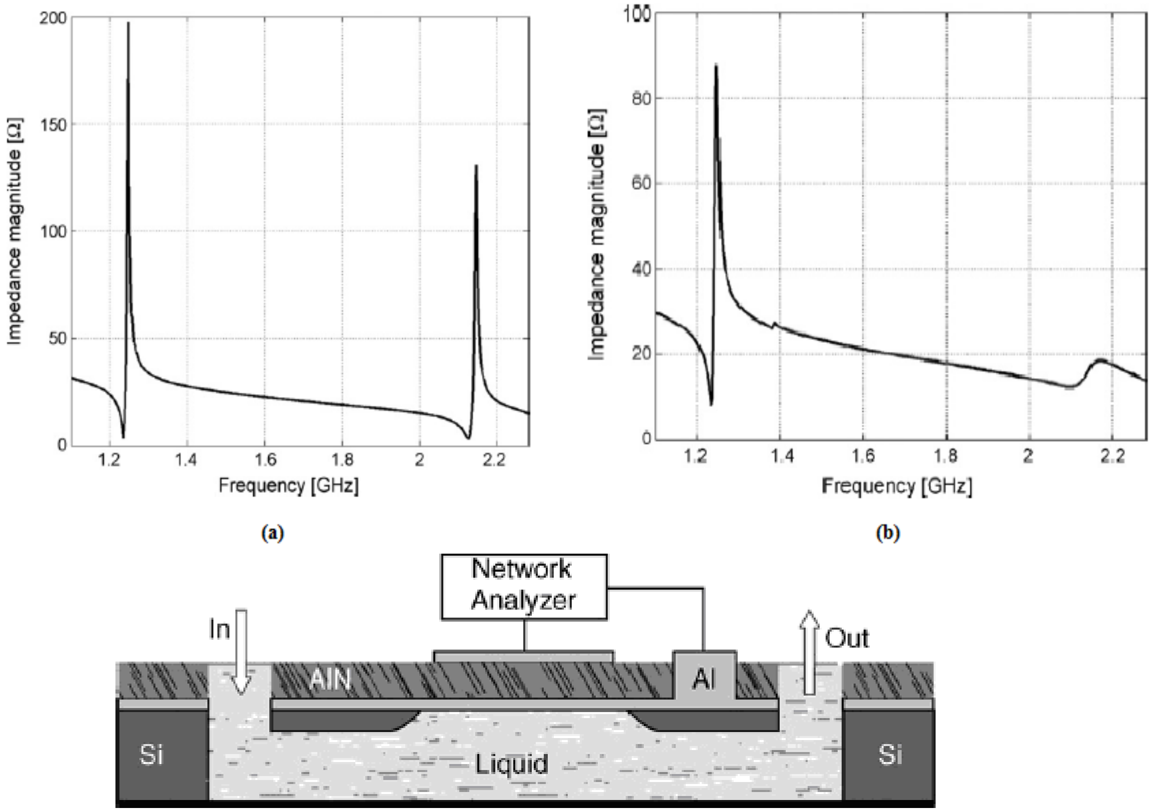

(a) (b)

(c)

Figure 1.10. (a) Impedance magnitude vs. frequency for an AlN shear mode FBAR operated in air. Clearly seen are the resonances of the shear mode at 1.25 GHz and the longitudinal mode at 2.15 GHz; (b) Impedance magnitude vs. frequency for an AlN shear mode FBAR operated with one side in contact with water. Clearly seen are the resonances of the shear mode at 1.25 GHz and the almost totally damped longitudinal mode at 2.15 GHz. (c) Schematic illustration of a shear mode FBAR resonator together with a microfluidic transport system [21]

However, FBARs mentioned above are operated on longitudinal mode. For liquid application, shear mode FBAR is better, because acoustic wave energy is radiated into liquid through compressional motion for longitudinal resonator, while shear wave shear acoustic waves do not produce compressional motion. Fortunately, it has been shown that shear mode can be excited through tilting c-axis of AlN and ZnO thin films. For example, Foster et al. [16] analyzed the excitation of longitudinal and shear wave in ZnO transducer, and they found the shear-wave excitation greatly exceeded the longitudinal wave excitation when the c-axis was inclined at angles near 40^0. Link et al. [17] fabricated SMRs based on 18° c-axis inclined ZnO thin films, and these SMRs have quality factors of 192 in water, making these devices attractive for sensing applications in liquids. Bjurström and Wingqvist et al. developed FBARs based on c-axis tilted AlN films, examined the variation of the electromechanical coupling coefficient and the quality factors of the resonators with tilt angle, and investigated the device performance in liquid [18-21]. From Figure 1.10, we can clearly see the promising potential of shear mode AlN FBAR in liquid application.

2.0 RESEARCH OBJECTIVE

As discussed in chapter 1, acoustic wave device has been proven as a powerful tool for sensor applications in wide area with a characteristic of high sensitivity, simple structure, and easy interconnection with electronic measurement systems, hence, considering its advantage, one objective of this thesis is to experimentally investigate quartz TSM resonator for new applications in the area we are interested in. On the other hand, FBARs has been demonstrated for sensor application with super high sensitivity, and it has been shown that when c-axis of ZnO and AlN is tilted, shear acoustic wave can be excited, which allows FBARs to be operated in liquid for sensor application, however, the theoretical analysis of FBAR base on c-axis tilted ZnO and AlN is less. Therefore, the overall objective of thesis is on the modeling and experimental study of bulk acoustic wave resonator sensor, which has three specific aims:

- To apply quartz TSM resonator for extracting viscoelastic properties of polymer nanocomposite thin films deposited on the resonators surface.
- To investigate quartz TSM resonator to monitor flow rate in liquid.
- To theoretically analyze FBARs based on c-axis tilted ZnO and AlN

3.0 CHARACTERIZATION OF POLYMER NANOCOMPOSITE FILMS USING QUARTZ TSM ACOUSTIC WAVE RESONATOR

3.1 INTRODUCTION

Characterization of thin film materials properties is very important for micro device design and fabrication as well as for many other engineering applications that use the thin films as the structural or functional layers [22]. Up to now, many techniques have been developed to measure the mechanical properties of thin films. However, for the mechanical properties measurement of thin films, small load and high sensitivity of displacement are required, which can't be satisfied by the traditional characterization techniques. Nano-indentation systems can accomplish small load to pico-Newton and measure sub-micro displacement, but they are only suitable for local characterization of thin films. In additional, some other recently developed techniques typically measure the load after imposing a fixed displacement by a nano-position motor [23-26], these techniques may lead to transient load, which can cause failure under displacement control. Hence, Techniques or methods which can be used to characterize thin film are highly desirable.

Meanwhile, as mention in chapter 1, acoustic wave devices are used for many sensor applications, and polymer thin films, as sensitive coating materials are widely used in acoustic wave resonator sensors for chemical and biological applications. The responses of acoustic wave sensors are commonly regarded as the result of mass change. However, it has been found that acoustic wave sensors are also subjected to non-gravimetric effects introduced by changes of viscoelastic properties of the coated thin film materials. Even when a solid film is coated on the resonator surface, the classic Sauerbrey equation that linearly relates the frequency shift verse the film thickness or mass is only valid when the film is very thin and rigid [27, 28]. For example, when the Sauerbrey equation is adopted, and the viscoelastic properties of the coating materials are ignored, errors as big as 50% can be caused. Therefore, the frequency response of acoustic wave resonator sensor contains the overall effect of the coating material, not just mass or thickness. Based on the one-dimensional transmission line model of acoustic wave resonator [29] the overall effect of the coating materials can be described by acoustic impedance, which include the thickness, mass density, and elastic or viscoelastic modulus of the coating materials. Therefore, for a better understanding of the acoustic wave sensor response, the acoustic wave impedance of the coating materials under various application circumstances should be examined. On the other hand, by using the relation between sensor response and the properties of the coating materials, acoustic wave resonator sensor may represents an effective and precise measurement technique in probing the properties of the coating materials [28, 30, 31].

Two methods have been used to identify the relationship between the measurable electrical response of resonators and the mechanical properties of coating layers. As discussed in chapter1, one is TLM, which treats the sensor structure as a combination of a uniform piezoelectric layer and one or more isotropic, homogeneous nonpiezoelectric layers, and assumes that lateral dimensions have no effect on the wave propagation [32]. TLM is the most accurate representation to date for a piezoelectric bulk acoustic wave resonator. The other is LEM, which represents the mechanical effect of coating layers by their equivalent electrical circuit element. LEM is the approximation of TLM and is only valid when surface load impedance is small enough compared to the shear mechanical impedance of the quartz and the resonator must work near the mechanical resonance [33]

PVDF or PVDF-TrFE has been studied extensively because of high piezoelectricity, which makes it an exceptional material for a variety of transducer applications [34-36]. Characterization of the materials properties including elastic shear modulus is important for device design and actuator applications. MWCNTs are important fillers to polymer, which could be dispersed in polymer to significantly affect the matrix's behaviors and properties. So far, many composites of MWCNTs in polymeric matrix have attracted considerable attention due to their unique mechanical and electrical properties [37-40].

In this study quartz TSM resonator is used to characterize the viscoelastic properties of nanocomposites thin films of multi-wall carbon nanotubes (MWCNTs) in copolymers of polyvinylidene fluoride-trifluoroethylene (PVDF-TrFE). Polymer-based carbon nanotube composites are becoming an attractive set of organic-inorganic materials due to their multifunctionality and many potential applications. The combination of superb mechanical, electrical and thermal properties of carbon nanotubes integrated with the lightweight, flexibility, and manufacturability of polymers provides the route for multifunctional materials. While many studies so far on polymer-CNT composites are focused on the mechanical property reinforcement by improving the interfacial property of CNT with the polymer matrix, there is no report on the viscoelastic property measurement of the polymer-CNT composites. It is expected that an accurate characterization of the complex shear modulus of polymer-CNT composites can be achieved by using quartz resonator sensors.

3.2 INPUT ELECTRIC ADMITTANCE OF A FOUR-LAYER TSM RESONATOR

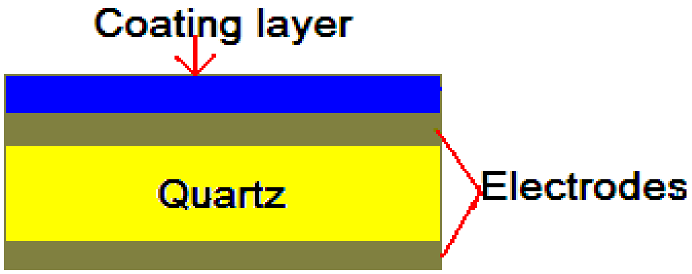

Figure 3.1. A schematic four-layer TSM resonator

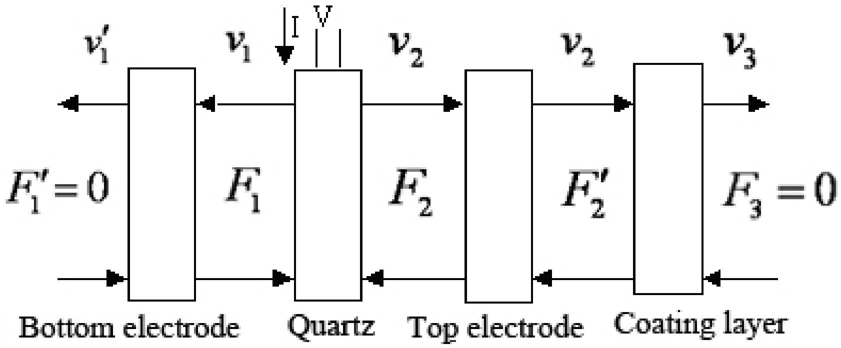

Figure 3.2. Transfer matrix model of TLM for TSM resonator

Figure 3.1 shows the schematic four-layer TSM resonator. The piezoelectric layer is a thin quartz disc, which can be treated a three-port device with one electric port and two acoustic ports. The two electrodes and coating layer are non-piezoelectric layers with two acoustic ports. The transfer matrix technique of the transmission line mode is adopted to calculate the input electric admittance of four-layer TSM resonator (Figure 3.2). Each layer's transformation matrix is shown below.

$$\begin{pmatrix} F_1 \\ v_1 \end{pmatrix} = \begin{pmatrix} \cos(\gamma_{e1}) & jZ_{Ce1}\sin(\gamma_{e1}) \\ j/Z_{Ce1}\sin(\gamma_{e1}) & cos(\gamma_{e1}) \end{pmatrix} \begin{pmatrix} F_1' \\ v_1' \end{pmatrix} \tag{3.1}$$

$$F_1' = 0 \tag{3.2}$$

$$\begin{pmatrix} F_2 \\ v_2 \end{pmatrix} = \begin{pmatrix} \cos(\gamma_{e2}) & jZ_{ce2}\sin(\gamma_{e2}) \\ j/Z_{ce2}\sin(\gamma_{e2}) & cos(\gamma_{e2}) \end{pmatrix} \begin{pmatrix} F_2^{'} \\ v_2^{'} \end{pmatrix} \tag{3.3}$$

$$\begin{pmatrix} F_2^{'} \\ v_2^{'} \end{pmatrix} = \begin{pmatrix} \cos(\gamma_L) & jZ_{CL}\sin(\gamma_L) \\ j/Z_{CL}\sin(\gamma_L) & cos(\gamma_L) \end{pmatrix} \begin{pmatrix} F_3 \\ v_3 \end{pmatrix} \tag{3.4}$$

$$F_3 = 0 \tag{3.5}$$

F , v , Z_C and γ are are the stress, displacement velocity, characteristic impedance and phase delay. $\gamma = \frac{\omega d}{\sqrt{G/\rho}}$, where d , G , ρ are the thickness, complex shear modulus and density. The subscript e_1 , e_2 , L represent the bottom electrode, top electrode and coating layer. From Eqs. (3.1) - (3.5), we can get the acoustic impedance Z_1 , Z_2

$$Z_1 = \frac{F_1}{v_1} = jZ_{Ce1}\tan(\gamma_{e1}) \tag{3.6a}$$

$$Z_2 = \frac{F_2}{v_2} = \sqrt{\rho_{e2}G_{e2}}\,\frac{Z_L + j\sqrt{\rho_{e2}G_{e2}}\tan(\omega\sqrt{\frac{\rho_{e2}}{G_{e2}}}d_{e2})}{\sqrt{\rho_{e2}G_{e2}} + jZ_L\tan(\omega\sqrt{\frac{\rho_{e2}}{G_{e2}}}d_{e2})} \tag{3.6b}$$

where Z_L has the following form,

$$Z_L = \frac{F_2^{'}}{v_2^{'}} = j\sqrt{\rho_L G_L}\tan(\omega\sqrt{\frac{\rho_L}{G_L}}d_L) \tag{3.7}$$

The transfer matrix of the piezoelectric layer is given by

$$\begin{bmatrix} V \\ I \end{bmatrix} = [A]\bullet\begin{bmatrix} F_2 \\ v_2 \end{bmatrix} \tag{3.8}$$

With

$$[A] = \frac{S}{\phi H} \begin{pmatrix} 1 & j\phi^2 / \omega C_0 \\ j\omega C_0 & 1 \end{pmatrix} \bullet A' \tag{3.9}$$

and

$$A' = \begin{pmatrix} \cos\gamma_q + j\frac{Z_1}{Z_{cq}}\sin\gamma_q & Z_{cq}(\frac{Z_1}{Z_{cq}}\cos\gamma + j\sin\gamma_q) \\ j\sin\gamma_q / Z_{cq} & 2(\cos\gamma - 1) + j\frac{Z_1}{Z_{cq}}\sin\gamma_q \end{pmatrix} \tag{3.10a}$$

$$H = \cos\gamma_q - 1 + j\frac{Z_1}{Z_{Cq}}\sin\gamma_q \tag{3.10b}$$

$$\phi = hC_0 \tag{3.10c}$$

$$h = \frac{e_q}{\varepsilon_q} \tag{3.10d}$$

$$C_0 = \varepsilon_q \frac{A}{h_q} \tag{3.10e}$$

$$\gamma_q = \omega d_q / \sqrt{\frac{C_q}{\rho_q}} \tag{3.10f}$$

$$Z_{cq} = \sqrt{\rho_q c_q} \tag{3.10g}$$

$$e_q = e_{26} \tag{3.10h}$$

$$\varepsilon_q = \varepsilon_{22} \tag{3.10i}$$

$$c_q = c_{66} + \frac{e_{26}{}^2}{\varepsilon_{22}} + j\omega\eta_q = \overline{c}_{66} + j\omega\eta_q \tag{3.10j}$$

C_0 is the static capacitance and S is the cross-section area of the quartz. c_{66}, e_{26}, ρ_q, ε_{22} and η_q are the components of the material property tensors for mechanical stiffness, piezoelectric constant, density , permittivity and viscosity of quartz. Using Eqs. (3.1)-(3.10), the input electric impedance of four-layer resonator can be obtained as

$$Z_{in}=\frac{V}{I}=\frac{1}{jwC_0}(1-\frac{K^2}{\gamma_q}\frac{2\tan(\frac{\gamma_q}{2})-j(\frac{Z_1+Z_2}{Z_{Cq}})}{(1+\frac{Z_1Z_2}{Z^2{}_{Cq}})-j(\frac{Z_1+Z_2}{Z_{Cq}})\cot(\gamma_q)}) \tag{3.11}$$

where $K^2=\frac{e_q{}^2}{\varepsilon_q{}^2c_q{}^2}$ is the electromechanical coupling coefficient of quartz. Both two electrodes are acoustically thin layers, their effect is very small. For simplicity, their effect will be taken into account in the effective parameters of resonators. Thus we have

$$Z_1=0 \tag{3.12a}$$

$$Z_2=Z_L \tag{3.12b}$$

From Eqs. (3.11)-(3.12), the input electric impedance of four-layer resonator can be simplified to

$$Z_{in}=\frac{1}{j\omega C_0}\left(1-\frac{K^2}{\gamma_q}\frac{2\tan\frac{\gamma_q}{2}-j\frac{Z_L}{Z_{Cq}}}{1-j\frac{Z_L}{Z_{Cq}}\cot\gamma_q}\right) \tag{3.13}$$

The electrical impedance in Eq. (3.13) can be represented as a static capacitance C_0 in parallel with motional branch Z_m, which can be expressed as:

$$Z_m=\frac{1}{j\omega C_0}\left(\frac{1-j\frac{Z_L}{Z_{Cq}}\cot\gamma_q}{\frac{K^2}{\gamma_q}[2\tan(\gamma_q/2)-j\frac{Z_L}{Z_{Cq}}]}-1\right) \tag{3.14}$$

It is more convinent to analyze the input admittance of a resonator instead of impedance. From Eqs. (3.13) and (3.14), the admittance is given by:

$$\begin{aligned} Y &= {}^{1}\!/\!{}_{Z_{in}} = G + jB \\ &= j\omega C_0^* + \frac{1}{Z_m} \end{aligned} \tag{3.15}$$

where $C_0^* = C_0 + C_{ex}$, with C_{ex} an added parasitic capacitance accounting for packaing ,connecting, etc.

3.3 MATERIALS AND METHOD

3.3.1 Materials preparation and experimental setup

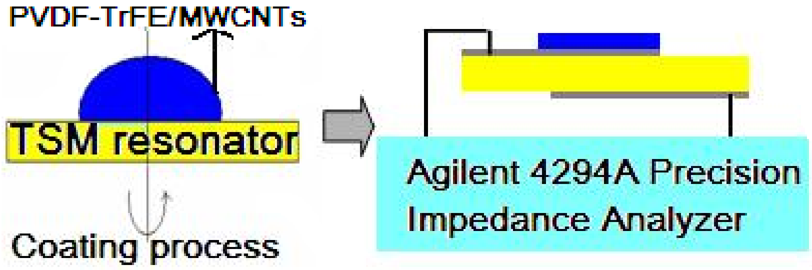

Figure 3.3. Schematic of PVDF-TrFE/MWCNTs nanocomposite thin film coating process and experimental setup

Figure 3.3 shows the experimental setup and coating process for the PVDF-TrFE/MWCNTs nanocomposite thin films on TSM resonators. PVDF-TrFE was dissolved in solvent N, N-Dimethylformamide (DMF) with weight ratio 1:1.9 to form a homogeneous solution. MWCNTs were then added into PVDF-TrFE/DMF with weight ratios (MWCNTS/PVDF-TrFE) of 0%, 1% and 2%. A rigorous sonication is conducted to form homogeneous nanotube suspension in the solution. Two steps of spin coating process were employed in the deposition: the first run was 500 rpm for 10sec and the second run was a high speed for 40 sec according to the desired thickness of films. Before measurement, films were annealed in oven at 65 ^{o}C and 100 ^{o}C each for one hour, and 165 ^{o}C over night.

The admittances of uncoated 10-MHZ TSM resonators were first measured by an Agilent 4294A Precision Impedance Analyzer (Agilent Technologies, Palo Alto, CA), which were recorded for the extraction of effective parameters of resonators. After spin-coating and thermal process, the thicknesses of films were determined by a profilometer (Dektak3 ST surface profiler, Veeco Instruments Inc., Woodbury, NY) and the admittances of the coated resonators were recorded. The effective parameters of uncoated resonators, the thickness of films and the admittance spectra of coating resonators were used in the extraction of the complex viscoelastic modulus of the nanocomposites films.

3.3.2 Characterization of uncoated TSM resonator sensor

As mentioned, before extracting the complex viscoelastic modulus of nanocomposite thin films, a calibration process is carried out to calculate the effective resonator's parameters. The effective parameters include the quartz's thickness (h_q), viscosity (η_q), static capacitance (C_0) and external capacitance (C_0^*). The fitting algorithm is based on a approach developed recently [41], which significantly reduces the computation time while keeping high resolution in comparison with other typical fitting algorithms. The effective parameters obtained with the calibration in the ambient condition with $Z_L = 0$. Then Eq. (3.14) can be simplified as

$$C_0 = \frac{1}{j\omega Z_m}\left(\frac{1}{\frac{K^2}{\gamma_q}\left[2\tan\left(\gamma_q/2\right)\right]} - 1\right) \tag{3.16}$$

The calibration process is as follows:

(a) The admittance spectrum $Y(\omega_i)$ of the uncoated resonator is measured and acquired through by using the impedance analyzer (where i=1 to M with M the number of frequency points). C_0^* is measured at two times of fundamental resonant frequency [41]. Z_m^i is obtained from Eq. (3.15).

(b) In a reasonable range η_q is discretized into η_q^j (where j=1 to n with n is the number of η_q). At first, high range is tried. Then it can be reduced to a lower range for precision requirement after several tries.

(c) For each Z_m^i and η_q^j , the thickness h_q^j is obtained through canceling the imaginary part of Eq.(3.16). A Regula-Falsi based algorithm is applied for getting the values of h_q .

(d) For each (ω_i , η_q^j , h_q^j), the corresponding values of C_0^j are obtained from Eq.(3.16).

(e) The solution of parameters (η_q^{sol} , h_q^{sol} , C_0^{sol}) is obtained as the one that make the smallest admittance spectrum error between theoretical and experimental values. The error function is defined as follow:

$$Error\,|_j = \frac{\sum_{i=1}^{M}\left(G(\omega_i)\,|_{EXP} - G(\omega_i)\,|_j^{TLM}\right)^2 + \sum_{i=1}^{M}\left(B(\omega_i)\,|_{EXP} - B(\omega_i)\,|_j^{TLM}\right)^2}{\sum_{i=1}^{M}\left(G(\omega_i)\,|_{EXP}\right)^2 + \sum_{i=1}^{M}\left(B(\omega_i)\,|_{EXP}\right)^2} \quad (3.17)$$

The conductance $G(\omega_i)\,|_j^{TLM}$ and the susceptance $B(\omega_i)\,|_j^{TLM}$ are calculated from Eq. (3.15), where j is the jth parameter solution; $G(\omega_i)\,|_{EXP}$ and $B(\omega_i)\,|_{EXP}$ are the experimental values of the conductance and susceptance respectively. M is the number of frequency points;

(f) According to $C_{ex}^{sol} = C_0^* - C_0^{sol}$, the external parallel capacitance C_{ex}^{sol} is obtained.

3.3.3 Extraction of the complex viscoelastic modulus

The extraction of the shear storage and loss modulus is similar with the sensor calibration procedure and the fitting algorithm is also based on the approach [41]. From Eq. (3.7), we can get

$$m_s(\omega) = \rho_L d_L = -\frac{\sqrt{\rho_L G_L}}{2j\omega}[\ln(r) + j(\theta + 2k\pi)] \tag{3.18}$$

where

$$r(\omega) = \left| \frac{\sqrt{\rho_L G_L} - Z_L(\omega)|_{EXP}}{\sqrt{\rho_L G_L} + Z_L(\omega)|_{EXP}} \right| \tag{3.18a}$$

$$\theta(\omega) = phase\left(\frac{\sqrt{\rho_L G_L} - Z_L(\omega)|_{EXP}}{\sqrt{\rho_L G_L} + Z_L(\omega)|_{EXP}} \right) \tag{3.18b}$$

with $-\pi \le \theta \le \pi$, $G_L = G' + G''$ and $k = 0, \pm 1, \pm 2, \ldots$. The detail of derivation can be found in literature [41], but there is a little change that in our case $Z_2 = 0$ (where Z_2 is the acoustic load impedance of the air) and $k = 0$. The extraction process includes the following steps.

(a) $Y(\omega_i)$, the admittance spectrum of the coated resonator, is recorded by impedance analyzer. C_0^* is measured at two times of fundamental resonant frequency [41]. $Z_L^i(\omega_i)|_{EXP}$ is obtained according to Eqs. (3.14) and (3.15) (where *i*=1 to *M* with *M* the number of frequency points).

(b) In a reasonable range G'' is discretized into G_j'' (where *j*=1 to *n* with *n* is the number of G_j''). At first, high range is tried. Then it can be reduced to a lower range for precision requirement after several tries.

(c) For each ω_i and G_j'', G_k' is obtained through canceling the function of $m_s(\omega_i, G_j'')$. A Regula-

Falsi based algorithm is applied and the effective parameters from sensor calibration were used to get the values of $G_k^{'}$. Then d_L^k is determined according to Eq.(3.18) with the density from the literature.

(d) The solutions of parameters with the value of Eq. (3.17) over 0.1% are ignored.

(e) The solution of parameters is obtained as the one that makes the smallest error between the extracted and the measured thickness.

3.4 RESULTS AND DISCUSSION

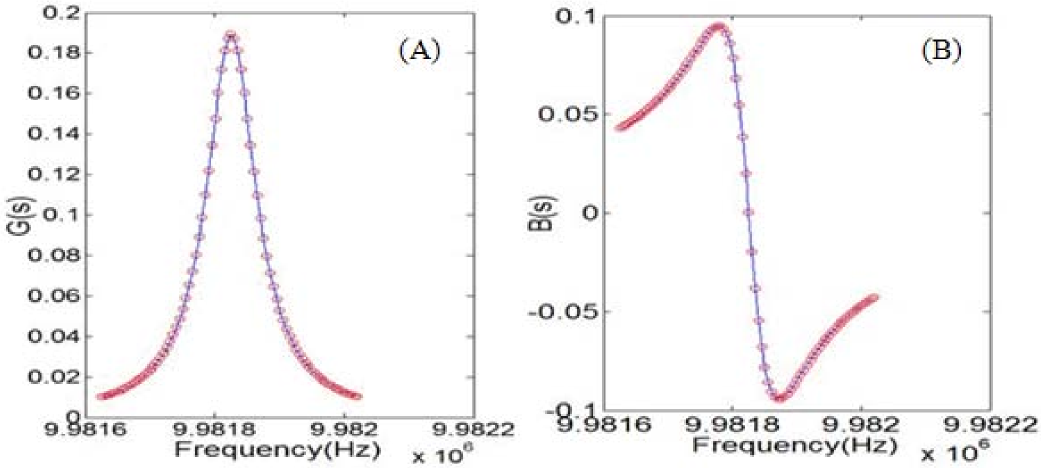

Figure 3.4. (A) Rel (Y) of uncoated TSM resonator; (B) Img (Y) of uncoated TSM resonator

Figure 3.4 shows the fitting result of the typical uncoated 10M-Hz TSM resonator. The average error of one point is 0.002% according to error function, Eq. (3.17), the points of admittance spectrum for calculation is 801, which indicates that the adopted algorithm is efficient and has high resolution.

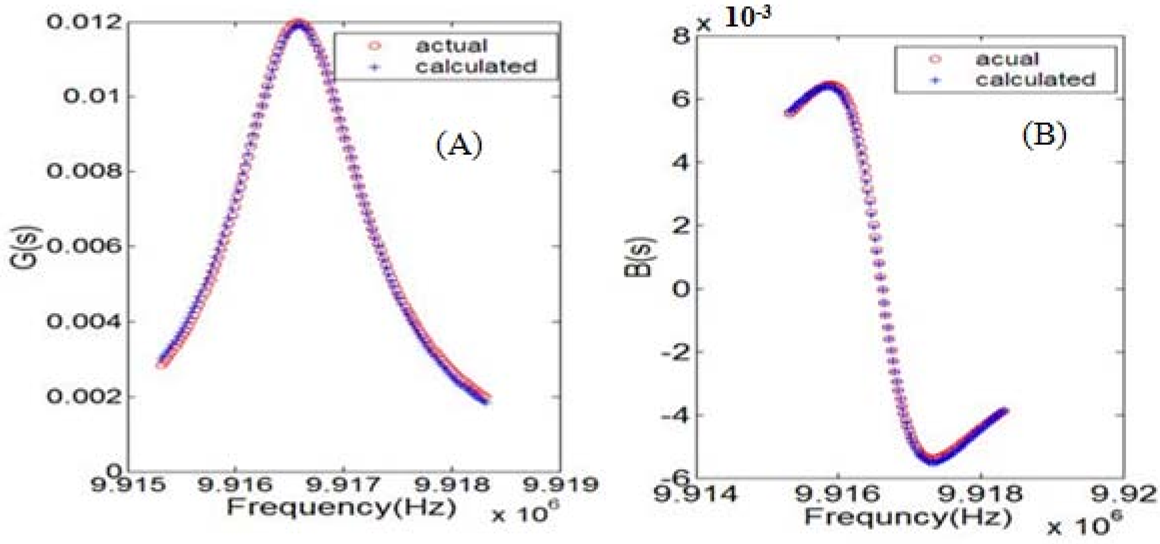

Figure 3.5. Rel (Y) of coated TSM resonator; (B) Img (Y) of coated TSM resonator

Figure 3.5 shows the typical fitting result of the coated TSM resonator, which also indicates the efficiency and reliability of data fitting. The coating film is made of PVDF-TrFE with the thickness of 1.6μm. The admittance spectrum for data fitting has 801 points. The average error of one point is less 0.03%. The main reason is that only one parameter is discredited, and the other one parameter can be obtained through Regula-Falsi algorithm, which assures that only the solutions that satisfy with the physical criterion are selected.

Density $\rho_q = 2651 Kg \cdot m^{-3}$, permittivity $\varepsilon_q = 9.657 \times 10^{-2} A \cdot s \cdot m^{-2}$, piezoelectric coefficient $e = 3.982 \times 10^{-11} A^2 \cdot S^4 \cdot kg^{-1} \cdot m^{-3}$ and piezoelectric stiffened shear modulus $\bar{c}_{66} = 2.947 \times 10^{10}\,\mathrm{N} \cdot \mathrm{m}^{-2}$ are adopted in sensor calibration and shear modulus extraction.

Table 3.1 lists the extracted effective parameters for an uncoated TSM resonator. It is found that the thickness is a little larger than the actual value (165μm), and the viscosity of the resonator is also larger than the reported value ($3.5*10^{-4}$ Pa•S) from literature [7]. This is due to that the measured admittance spectrum includes the effect of the two electrode layers and other damping effects, which are neglected in the theoretical equations used for the parameter extraction. The effective parameters, which accommodate the effect of electrodes and experimental set-up, for the uncoated resonators will then be used in the characterization of the viscoelastic properties of the nanocomposite thin films that are subsequently coated on the resonators.

Table 3.1 The effective parameters of quartz thickness shear mode resonator

C_0 (pf)	h_q (μm)	η_q (Pa·S)	C_{ex} (pf)
4.47	166.48	0.0043	1.58

It has been found in our experimental studies that in the gravimetric regime (films with very thin thickness), the TSM resonator is not sensitive to the viscoelastic properties of coating layers, and even a small error in the thickness will cause a large error in the extracted viscoelastic properties. Thus it is important to extract the parameters in nongravimetric regime, where the viscoelastic contribution is substantial and the error due to thickness change can be greatly reduced [41]. However, the bandwidth of admittance spectrum increases with the thickness and the shear modulus may also be influenced by the frequency, which can lead to errors since it is assumed that the shear modulus is constant during data fitting. The selection of an appropriate thickness range allows the accurate characterization of the viscoelastic properties of the nanocomposite films by using acoustic wave resonator sensors. In our experiments, thickness from 15 to 20 um is found to be the desirable range, which is in the nongravimetric regime and assures a fitting error less than 0.1%.

In our previous study [42], the extracted parameters are those that allow the best curve fitting between the theoretical and experimental admittance spectrum. However, the thickness thus determined is found to be much different with the actual measurement value, which indicates the extracted materials properties for the nanocomposite films can't meet with physical criterion. So a new criterion for parameter selection is added, i.e., the extracted complex shear modulus for the nanocomposite film is the one that make the error function [Eq. (3.17)] less than 0.1% while the extracted film thickness is closest to the measured value.

Considering that the concentration of CNTs in each nanocomposite film is quite low, it is assumed that all the nanocomposite films have the same density value ($1780 Kg \cdot m^{-3}$). Figure 3.6 shows the effect of CNTs on the complex shear modulus of PVDF-TrFE nanocomposite thin films. It is found that both storage modulus and loss modulus don't change much with the amount of CNTs, and the storage modulus actually decreases slightly with the CNTs concentration. However, no viscoelastic property enhancement by using carbon nanotubes is observed for the nanocomposite films. The decrease of the shear modulus of the nanocomposites could be due to the waviness of the nanotubes in the polymer matrix. A recent study on the effects of nanotube waviness on the modulus of nanotube-reinforced polymers has indicated that the nanotube curvature significantly reduces the effective reinforcement when compared to straight nanotubes [43, 44]. The sonication process used in the preparation of a homogenous carbon nanotube suspension in the polymer solution may cause substantial waviness of the carbon nanotubes.

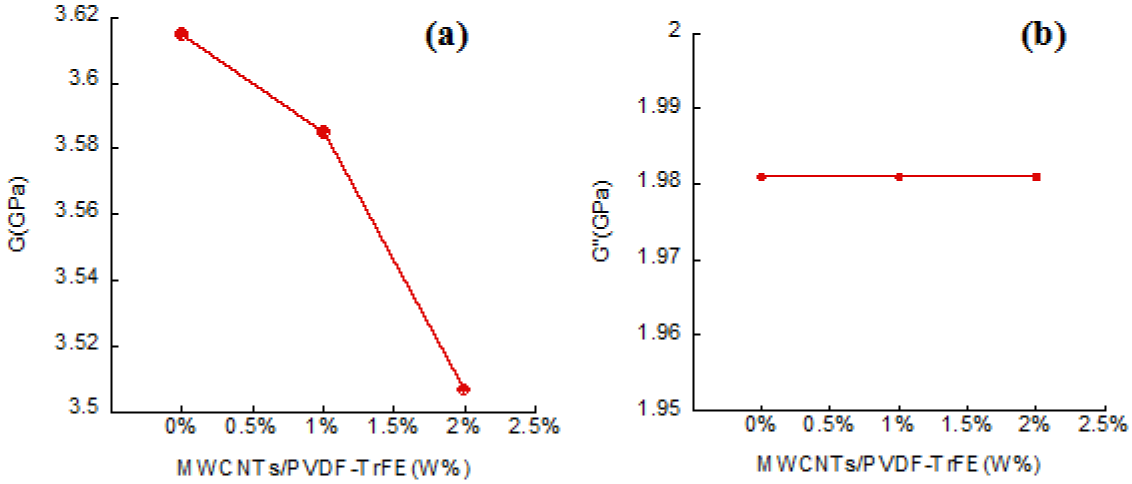

Figure 3.6. (a) Storage modulus of PVDF-TrFE/MWCNTs nanocomposite thin films; (b) Loss modulus of PVDF-TrFE/MWCNTs nanocomposite thin films

In addition, it has been found that the addition of carbon nanotubes can cause some non-uniformity such as surface roughness of nanocomposite thin films during deposition process. This non-uniformity is not included in modeling for the acoustic wave resonator [6]. For a better theoretical modeling, the surface roughness should be taken into account. A possible way to include the surface roughness in the theoretical derivation of the electrical impedance/admittance of the acoustic wave resonator is to model the thin film as two layers: one rough layer and one uniform layer [41]. In addition, appropriate surface modification of carbon nanotubes may lead to an improved uniformity of the nanocomposites in the fabrication processing.

3.5 CONCLUSION

The input electrical impedance/admittance of a four-layer acoustic wave resonator sensor is derived using the transfer matrix approach by taking into account the acoustic wave impedance of the polymeric layer. Based on the electrical impedance equation, the complex shear modulus of PVDF-TrFE/MWCNT composite thin films has been extracted through fitting the theoretical curves to the experimental value. The fitting results show that the data fitting process is reliable and accurate in the characterization of complex shear modulus of the coating layer. It has been found that the storage modulus of the nanocomposites decreases slightly with the carbon nanotube concentration, while no significant variation is found for the loss modulus.

4.0 FLOW SENSOR BASED ON QUARTZ TSM RESONATOR

4.1 INTRODUCTION

A flow sensor is a device for sensing the rate of fluid flow. It is a critical component for system operation monitoring and control in many industrial and laboratory applications. Typically a flow sensor is the sensing element used in a flow meter or flow logger, to record the flow of fluids. There are various kinds of flow sensors and flow meters: traditional mechanical devices [45], such as variable area flow meters, pitot tubes and turbine meters, are simple and do not require power supply, however, they are limited by their physical size and mechanical characteristics, especially for many applications that require high integration and feasibility of electronic control. Some invasive methods such as ultrasonic flowmeters [46] and laser doppler anemometers [47], are nonintrusive and high flow rate sensitive, however, they are high-cost and require complex auxiliary electronic parts. Additionally, the wildly used thermal anemometers such as hot -wire anemometer, can measures the flow in a precise location and has extremely high frequency-response, however, for sensor design and practice application, there exist a lot issues include breakage of filament stability, calibration and auxiliary electronics[48].

Acoustic wave devices have been extensively studied for many physical and chemical sensing applications [2]. Also, acoustic wave resonators have been investigated for flow rate measurement, and flow sensors based on SAW resonators have been demonstrated with attractive features of high sensitivity, wide dynamic range and direct digital output [49, 50]. This kind of SAW flow sensor is based on thermal convection: SAW device with heater is placed in the flow path. When the fluid flow passes over the sensor surface, it carries heat and changes the temperature of sensor substrate. Thus the frequency of SAW device changes due to its frequency-temperature dependence. Although the theoretical aspect of this kind sensor is simple and well established, the necessity of a heater for sensor operation may impose practical difficulties in which large power consumption is usually not desirable for compact sensor operation. In addition, the variation of ambient temperature and heater power supply may cause instability of frequency output; to minimize these effects, an additional SAW device that is not exposed to the fluid flow is needed as a reference, which increases system cost and complexity.

On the other hand BAW resonators have not been investigated for flow sensors, although BAW resonators, particularly quartz TSM resonators are often preferable in many sensor applications [51-53].As we have already shown in chapter 1 and 3, a resonator commonly consists of one thin layer of piezoelectric material with two electrodes on both sides. For sensor applications, an external chemical or physical sensitive thin film is usually coated on the top of the resonator. When AC electric field is applied across the resonator electrodes, acoustic waves are generated and propagate in the device due to the piezoelectric property. Variations in coating thin film parameters, including the thickness, density and complex shear modulus and interfacial interactions, affect the amplitude and phase of the acoustic wave propagation in the device, which change the electrical properties of the resonator. Therefore, the measured quantity can be precisely extracted by the resonance characteristics and the electrical spectrum of the resonator.

However, the electrical properties of the resonator, such as resonant frequency shift and mechanical damping not only depend on the mechanical properties of the coating layer and the surface interactions, but also on mechanical or electrical loading conditions since the materials properties of quartz resonators are subjected to changes under electrical or mechanical fields. For example, A. D. Ballato et al. revealed that resonant frequency shift of singly-rotated Y-cut quartz resonator due to the applied force on the rim, is dependant on the force magnitude, crystal cut angle, azimuth angle and the vibration mode [54]. A. Ballato et al. investigated the force-frequency effect of double rotated quartz resonators [55]. Ratajski introduced the force-frequency coefficient for quantifying the force-frequency effect, and he derived an empirical chart based on the normalized experimental results, which can be used to determine the force-frequency behavior of any crystal cut in the singly rotated Y-cut group [56].In papers of Lee et al., two dimensional governing equations were derived for theoretical analysis of force-frequency effect; the initial stress distribution was computed to study the plate vibration; formula for predicting the resonant frequency shift was developed and compared with experimental results[57, 58]. Numerical methods including finite element method (FEM) were also used to investigate the force-frequency effect of quartz resonators [59, 60]. Thus, it is often desirable to minimize force-frequency effect when the resonators are used for frequency control and signal processing applications. On the other hand, through the force-frequency effect quartz acoustic wave resonators have also found applications as force sensors, pressure sensors, or accelerometers [61-63]. Therefore, it is possible to apply resonator for flow measurement if the mechanical load due to the flow can significantly change the frequency response of acoustic wave resonators due to linear or nonlinear response of the device by choosing appropriate flow path and mechanical boundary conditions.

In this study, quartz acoustic wave resonator is investigated as flow sensor for in-situ and real time detection of fluid (water) flow rate at room temperature. Considering the structural simplicity and high mechanical quality factor, quartz TSM resonator is particularly chosen as the sensing element. For flow rate measurement, the quartz resonator is edge-bonded at the sensor mounting port in a specially designed flow chamber. At first the relation of resonant frequency shift with flow rate is theoretically discussed based on the nonlinear response of the resonator. The resonant frequency shifts of fundamental thickness shear mode and overtones are then monitored as the sensor responses to different flow rates. The sensitivity and repeatability of the acoustic wave flow sensor are experimentally studied. Finally a brief discussion is given on the flow sensor optimization and potential applications.

4.2 MATERIAL AND METHOD

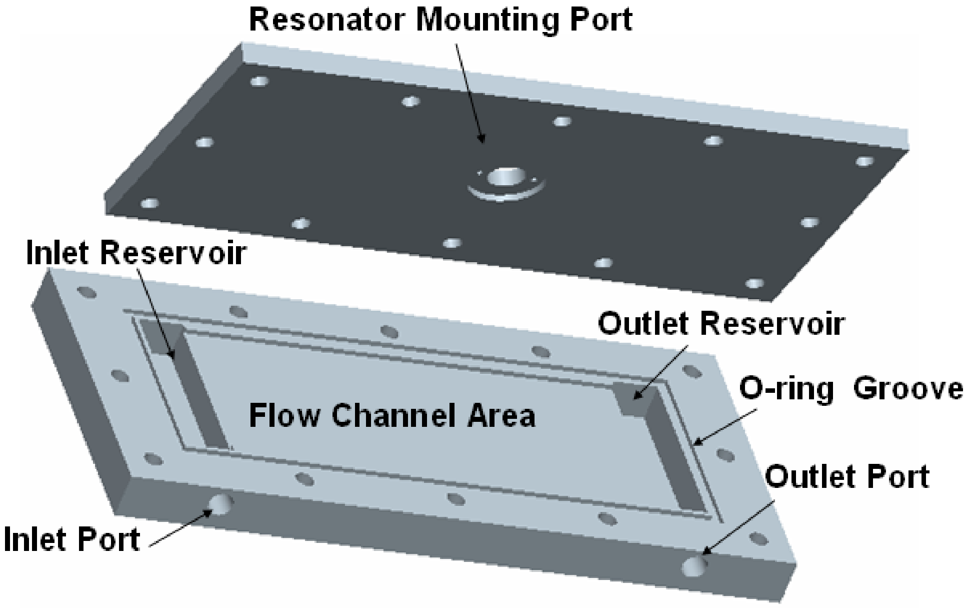

(a)

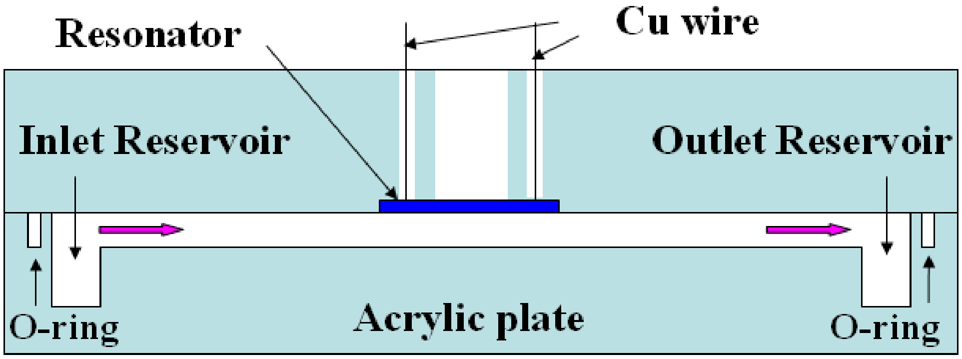

(b)

Figure 4.1. Schematic of flow chamber: (a) Top and bottom plate, (b) Cross section

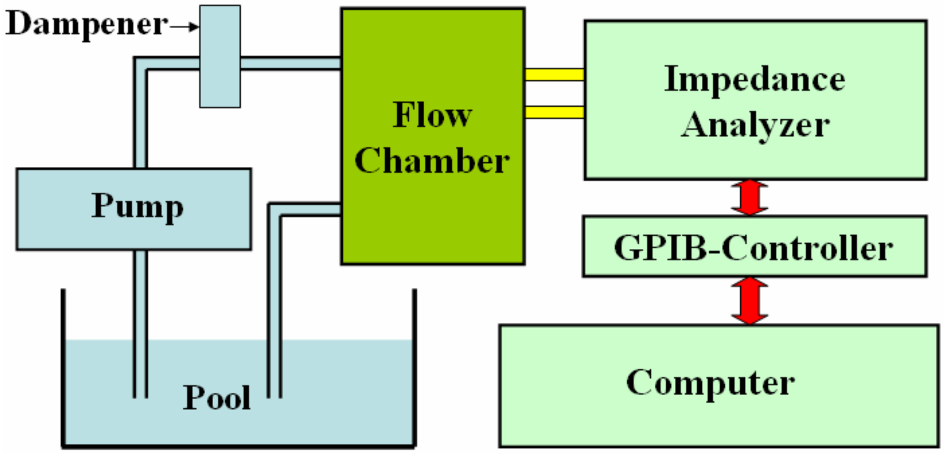

Figure 4.2. The experiment setup for flow rate measurement

5MHz At-cut quartz TSM resonator (Stanford Research Systems, Inc., Sunnyvale, CA) with 25.4 mm diameter was used in this study as a flow sensor. A flow chamber was designed according to the method proposed by Chuang et al. [64]. Figure 4.1 shows the schematic of the chamber, which is composed of two parallel acrylic plates, in which a rectangular flow channel, inlet and outlet reservoir, one sensor mounting port, one inlet port and outlet port are formed. These two plates were hold together through bolts and an O-ring between them to prevent the liquid leakage. The top plate was machined to form a sensor mounting port, and the quartz resonator was edge-bonded at the port using epoxy of ECCOBOND® 45 Clear (Ellsworth Adhesives, Germantown, WI) such that one surface of the resonator is exposed to the flowing liquid and the other surface is exposed to the air. Two fine Cu wires were bonded to the resonator electrodes through silver paste, which provides electrical connection for resonator impedance measurement. The rectangular flow channel, inlet reservoir, outlet reservoir, inlet port and outlet port were formed in the bottom plate. During flow measurement, fluid entered inlet reservoir through inlet port, passed through rectangular flow channel, flowed into outlet reservoir and exited through the outlet port. Plastic pipes were connected to inlet and outlet port for flow delivery. The dimension of flow channel is 165.10mm×69.85mm×0.51mm ($L \times w \times h$), and dimension for these two reservoirs is 19.05mm×76.0mm×15.24mm.

Figure 4.2 shows the measurement setup, which is made of water pool, Manostat Preston pump (Barrinton, IL), pulse dampener (Cole-Parmer Instrument Company, Vernon Hills, Illinois), flow chamber, Agilent 4294A Precision Impedance (Agilent Technologies, Palo Alto, CA), Hi-Speed GPIB Controller (NI, Austin, Texas) and computer. The pool was used to store the fluid: deionized (DI) water, which was driven by the pump. The pulse dampener was adopted to smooth the flow considering the unstable flow due to the pulse pump. The resonator admittance impedance spectra near the resonant frequencies were recorded by the impedance analyzer. Through data fitting the admittance impedance spectra, the resonant frequencies were precisely extracted. 1st (fundamental), 3rd, 5th, 7th and 9th series resonant frequencies as the sensor response were monitored and recorded during flow measurement. Water flow rates up to 3000ml/min were used in this study, all of which are limited to laminar flow; corresponding Reynolds numbers were 0 to 822.

4.3 METHOD OF FLOW MEASUREMENT

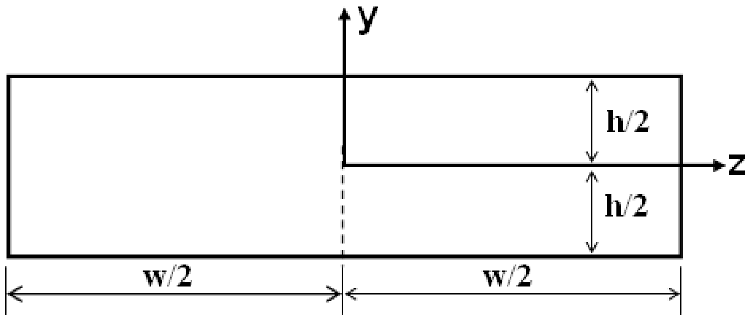

(a) yz plane

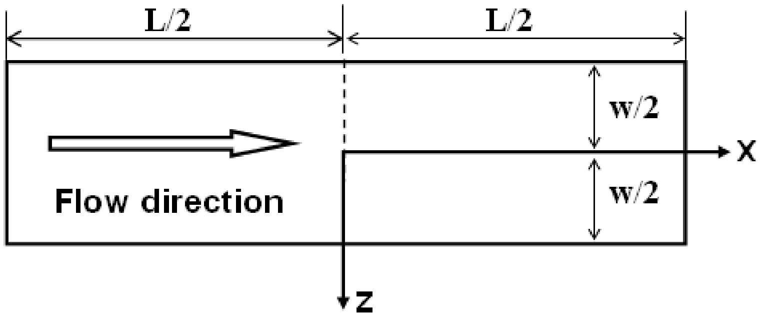

(b) xz plane

Figure 4.3. Cross sections of the flow channel: (a) yz plane, (b) xz plane

Figure 4.3 shows cross sections of the rectangular flow channel and a rectangular Cartesian coordinate system (x, y, z) built for further flow discussion. The top and bottom plate is located at $y = h/2$ and $y = -h/2$. The lateral walls are located at $z = \pm w/2$. In the rectangular flow channel, the relation of pressure p and volumetric flow rate Q is given by Eq. (4.1) [64, 65]:

$$Q = \frac{h^3 w}{12\mu}\left(-\frac{\mathrm{dp}}{\mathrm{dx}}\right)\left(1 - \frac{192h}{\pi^5 w}\sum_{n=1,3,5.....}^{\infty}\frac{1}{n^5}\tanh\left(\frac{n\pi w}{2h}\right)\right) \qquad (4.1)$$

where μ , L , w and h are the viscosity of fluid, the length, width and height of the flow channel. Shear stress τ at the wall ($y = \pm h/2$) is given by Eq. (4.2) [64]:

$$\tau = \frac{h}{2}\left(-\frac{\mathrm{dp}}{\mathrm{dx}}\right)\left[1-\frac{8}{\pi^2}\sum_{n=1,3,5...}^{\infty}\frac{1}{n^2}\frac{\cosh\left(\frac{n\pi z}{h}\right)}{\cosh\left(\frac{n\pi w}{2h}\right)}\right] \tag{4.2}$$

From Eq. (4.1) we can get:

$$\frac{\mathrm{dp}}{\mathrm{dx}} = -\frac{12Q\mu}{h^3 w\left(1-\frac{192h}{\pi^5 w}\sum_{n=1,3,5.....}^{\infty}\frac{1}{n^5}\tanh\left(\frac{n\pi w}{2h}\right)\right)} \tag{4.3}$$

We know that the resonator is located at (0, $h/2$, 0). Thus, when Q is constant, the normal pressure difference ΔP on resonator two sides can be obtained:

$$\Delta P = \int_{L/2}^{0}\frac{dp}{dx}dx + \frac{8\mu L_p}{\pi R_p^4}Q = \frac{6Q\mu L}{h^3 w\left(1-\frac{192h}{\pi^5 w}\sum_{n=1,3,5.....}^{\infty}\frac{1}{n^5}\tanh\left(\frac{n\pi w}{2h}\right)\right)} + \frac{8\mu L_p}{\pi R_p^4}Q \tag{4.4}$$

The first term in Eq. (4.4) represents the pressure drop from the resonator position to the outlet port, and the second term is the expression of the pipe pressure drop from the outlet port to back side of resonator. Also, we can get shear stress τ_r on the resonator surface through substituting the resonator position into Eq. (4.2):

$$\tau_r = \frac{h}{2}\left(-\frac{\mathrm{dp}}{\mathrm{dx}}\right)\left[1-\frac{8}{\pi^2}\sum_{n=1,3,5...}^{\infty}\frac{1}{n^2}\frac{\cosh\left(\frac{n\pi z}{h}\right)}{\cosh\left(\frac{n\pi w}{2h}\right)}\right] = \frac{6\mu Q}{h^2 w}\frac{\left[1-\frac{8}{\pi^2}\sum_{n=1,3,5...}^{\infty}\frac{1}{n^2\cosh\left(\frac{n\pi w}{2h}\right)}\right]}{\left[1-\frac{192h}{\pi^5 w}\sum_{n=1,3,5...}^{\infty}\frac{1}{n^5}\tanh\left(\frac{n\pi w}{2h}\right)\right]} \tag{4.5}$$

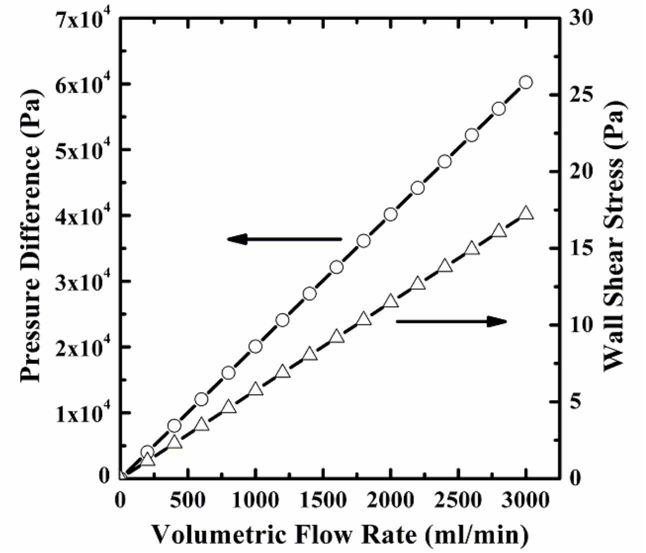

Figure 4.4. The normal pressure difference and wall shear stress versus volumetric flow rate

Figure 4.4 plots the results of ΔP and τ_r calculated through Eqs. (4.4) and (4.5), which show that both ΔP and τ_r are proportional to the flow rate. When the flow is applied, the resonator will be deformed due to ΔP and τ_r. In Figure 4.5(a) the dotted line indicates the middle plane, which has a flexure w. During the deformation, the quartz disc is subjected to either compression or tension on the 2 sides of middle plane. According to the first-order perturbation integral [66], this anti-symmetrical deformation has no effect on the resonant frequencies. However, the stretch of middle plane and the contraction of thickness cause a second-order (or nonlinear) frequency shift [67].

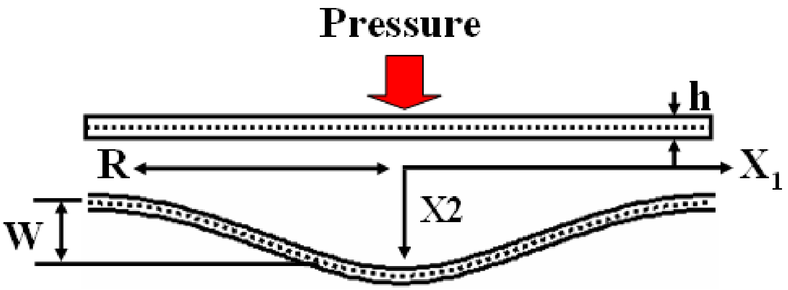

(a) Lateral view

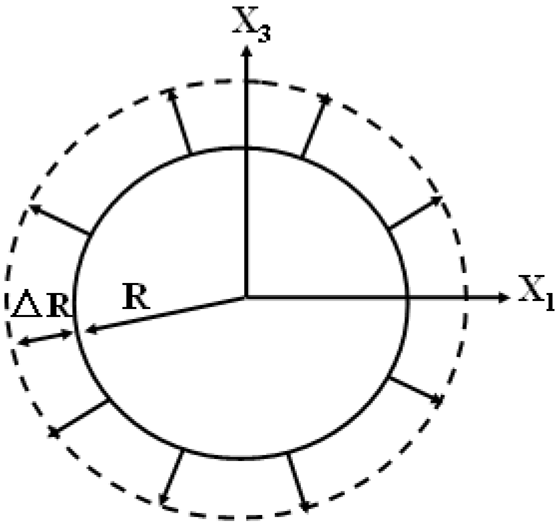

(b) Top view

Figure 4.5. Deflection of a quartz resonator disk subjected to normal pressure caused by fluid flow: (a) Lateral view, (b) Top view

It is found that the resonant frequencies are affected by zero-order strains through the second and third order elastic stiffness coefficient, and also by first order strain gradients through the third-order elastic stiffness [58]. In other words, resonant frequency shift will be induced by the mechanical strain or stress. For a given flow rate in the flow path of the flow chamber, finite element analysis (FEA) was performed using ANSYS, it is found that the magnitude of ΔP is significantly (around 3500 times) higher than τ_r, and compared with ΔP the strain or stress induced by τ_r can be ignored. Thus ΔP could be the primary factor for resonant frequency shift of the quartz resonator, and the effect of τ_r on frequency change is then ignored in the later analysis.

In the theoretical analysis of force-frequency relationship for quartz resonators, the isotropic assumption is often made for the calculation of the stress distribution, and the results were found to be very consistent with the experimental results [58, 68]. For the determination of the mechanical deflection of quartz resonators subjected a steady fluid flow rate, we assume that the quartz resonator is isotropic plate with Poisson's ratio υ, Young's modulus E and thickness h_r. Thus, for an isotropic plate with clamped edge, the deflection w due to the uniform normal load ΔP on the surface can be achieved by [69]:

$$w = \frac{\Delta P}{64D}\left(R^2 - r^2\right)^2 \tag{4.6}$$

where $D = \frac{Eh_r^3}{12\left(1-\upsilon^2\right)}$ is the rigidity of the quartz plate. ΔP, R and r are the normal pressure difference on resonator two sides, the radius and the radial distance of the point of interest in the middle plane. Therefore, the radius of the middle plane will be elongated from R to $R + \Delta R$, as was schematically shown in Figure 4.5(B), and ΔR is given by:

$$\begin{aligned} \Delta R &= \int_0^R \left[\left(1+\left(w'\right)^2\right)^{1/2} - 1\right] dr \\ &\cong \int_0^R \frac{1}{2}\left(w'\right)^2 dr \\ &= \frac{R^7}{6720D^2}\Delta P^2 \end{aligned} \tag{4.7}$$

The resonant frequency shift can be determined by the force-induced strain distribution [58], and the main terms for fundamental resonant frequency are given [67]:

$$\frac{\Delta f}{f} = A_1\varepsilon_1^o + A_2\varepsilon_2^o + A_3\varepsilon_3^o \tag{4.8}$$

where the coefficients A_1, A_2 and A_3 are determined by the second-order and third-order elastic constants. ε_1^o, ε_2^o and ε_3^o are initial strains of middle plain due to the pressure. Here, for estimation, the average strains are used [67], and the expression can be easily found for ε_1^o and ε_3^o:

$$\varepsilon_1^o = \varepsilon_3^o \cong \frac{\Delta R}{R} = \frac{R^6}{6720D^2}\Delta P^2 \tag{4.9}$$

Since the normal stress along the thickness direction is approximately zero for a very thin plate, according to strain and stress relations, ε_2^0 can be given: ε_2^0

$$\varepsilon_2^o = -\frac{C_{21}}{C_{22}}\varepsilon_1^o - \frac{C_{23}}{C_{22}}\varepsilon_3^o = -\frac{(C_{21}+C_{23})R^6}{6720 C_{22} D^2}\Delta P^2 \tag{4.10}$$

where C_{ij} is the quartz stiffness.

From Eq. (4.1) to (4.10), finally the relation between the fundamental resonant frequency shift and flow rate is found as:

$$\begin{aligned}\frac{\Delta f}{f} &= \left[(A_1+A_3)-\left(\frac{C_{21}+C_{23}}{C_{22}}\right)A_2\right]\frac{R^6}{6720D^2}\Delta P^2\\ &= \left[(A_1+A_3)-\left(\frac{C_{21}+C_{23}}{C_{22}}\right)A_2\right]\frac{R^6}{6720D^2}\left(\frac{6\mu L}{h^3 w(1-\frac{192h}{\pi^5 w}\sum_{n=1,3,5.....}^{\infty}\frac{1}{n^5}\tanh(\frac{n\pi w}{2h}))}+\frac{8\mu L_p}{\pi R_p^4}\right)^2 \mathrm{Q}^2\end{aligned} \tag{4.11}$$

It can be seen from Eq. (4.4) that the normal pressure difference is proportional to the flow rate; And Eqs. (4.8)- (4.10) show that the resonant frequency shift of the resonator has a quadratic relation with normal pressure difference. Thus, as shown in Eq. (4.11), the resonant frequency shift of quartz resonator caused by fluid flow is in a quadratic relation with the flow rate. For sensor design and application, it is often desirable that linear or first-order transduction relation between the measure and the output electrical signal can be established. With frequency as the output signal, nonlinear relationship is still quite convenient for sensor applications.

4.4 RESULTS AND DISCUSSION

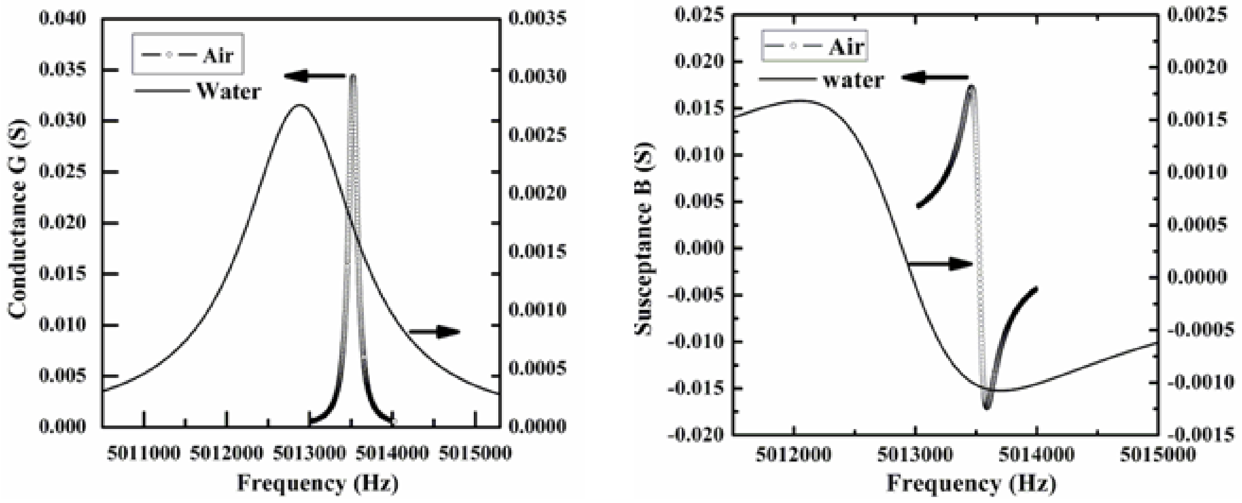

(a) (b)

Figure 4.6. Admittance (Y=G+jB) spectrum near fundamental resonant frequency in the air and water: (a) Conductance G; (b) Susceptance B

The electrical admittance spectra of TSM quartz resonator are first measured in the air and de-ionized (DI) water with zero flow rate. Figure 4.6 shows the admittance-frequency spectra of the resonator near the fundamental resonant frequency. G is conductance, the real part of admittance (Y), and B is susceptance, the imaginary part of admittance. It can be seen that resonant frequency is decreased due to the liquid load, and the spectrum is widened and the peak is greatly decreased due to increased viscous damping. The increased damping is reflected from the change of motional resistance (R) and mechanical Q of the resonator. The motional resistance and Q factor of the resonator are found to be 29Ω and 39477 in the air, and 362Ω and 3077 in the water. The 1st resonance frequency shift due to water load is around 645 Hz, which is very close to the theoretical value 669Hz calculated according to the Kanazawa equation [6, 70].

$$\Delta f = \frac{f_0^{3/2}(\rho_L \eta_L)^{1/2}}{(\pi \rho_q \mu_q)^{1/2}} \tag{4.12}$$

where f_0, ρ_L, η_L, ρ_q and μ_q are 1st resonant frequency in the air, density of liquid, viscosity of liquid, density of quartz and piezoelectric stiffened shear modulus. ρ_L =1000 (Kgm^{-3}), η_L =8.7048×10^{-4}(Pa•s), ρ_q =2651(Kgm^{-3}) and μ_q =2.947×10^{10} (Nm^{-2}) were used for the calculation. The resonant frequency of resonator in the DI water with zero flow rate is used as the baseline for the frequency shift of device under different flow rates.

It is found that the flow variation due to the pulse pump makes the resonator admittance spectrum unstable under a certain flow rate, which induces some errors in extracting resonant frequencies. Even when a pulse damper is adopted, the effect of flow variation can still be seen in the admittance spectrum, as shown in Figure 4.7(A). To reduce the measurement noise, 5-times average values are taken for each data point in the electrical admittance-frequency spectrum, which is an average measurement algorithm provided by the Precision Impedance Analyzer. From Figure 4.7(B) it can be seen the admittance spectrum after average becomes stable and smooth, which improves the precision of extracting resonant frequency.

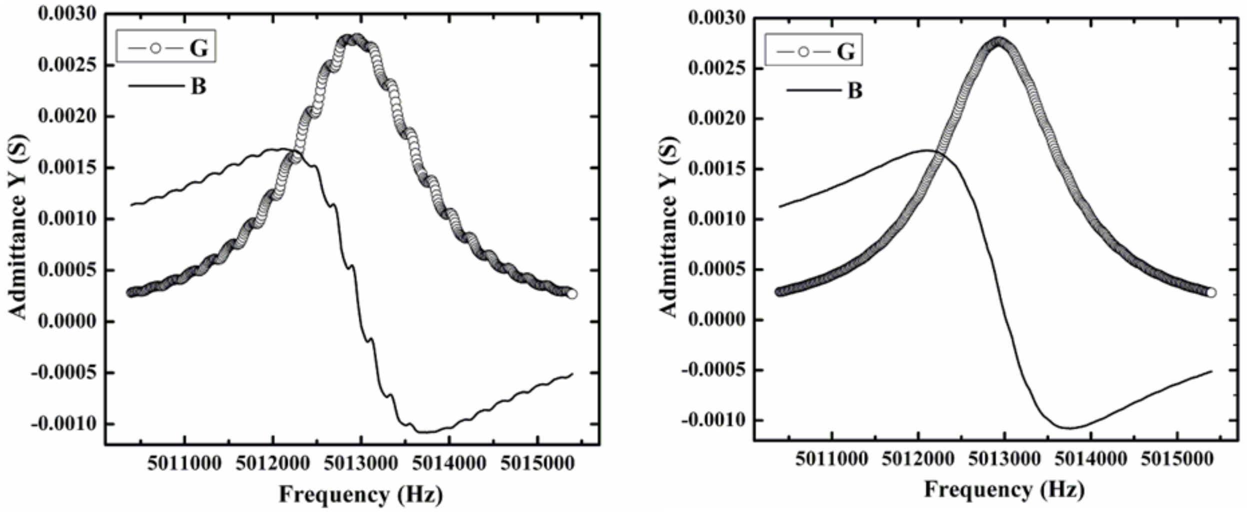

(a) Without average

(b) After 5 time average

Figure 4.7. Typical electrical admittance (Y=G+jB) spectra of quartz resonator flow sensor: (a) Without average; (b) After 5 time average

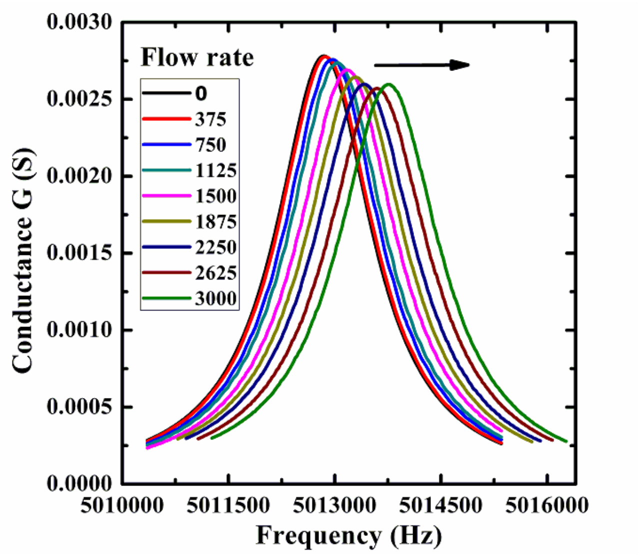

(a) 1st mode

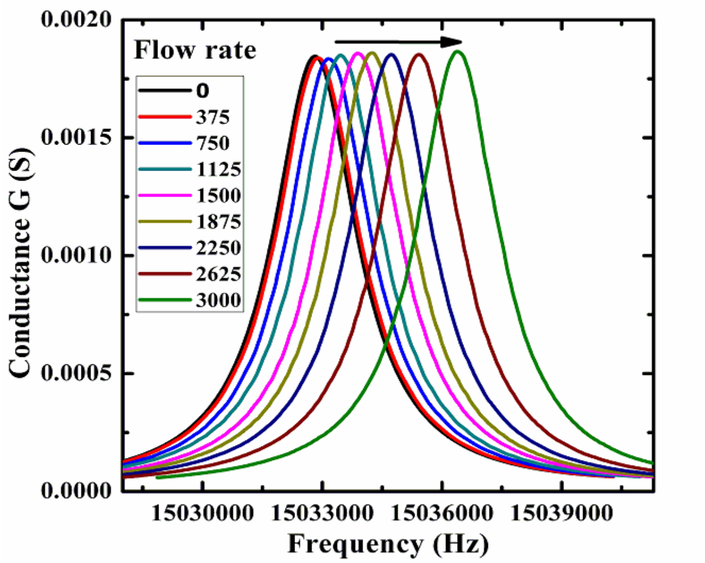

(b) 3rd mode

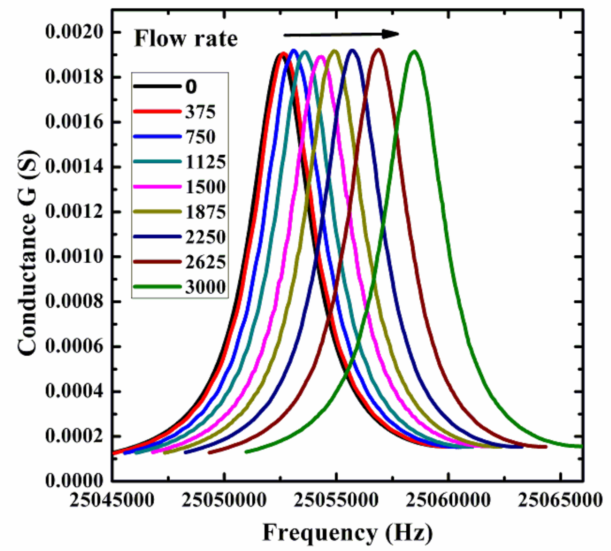

(c) 5th mode

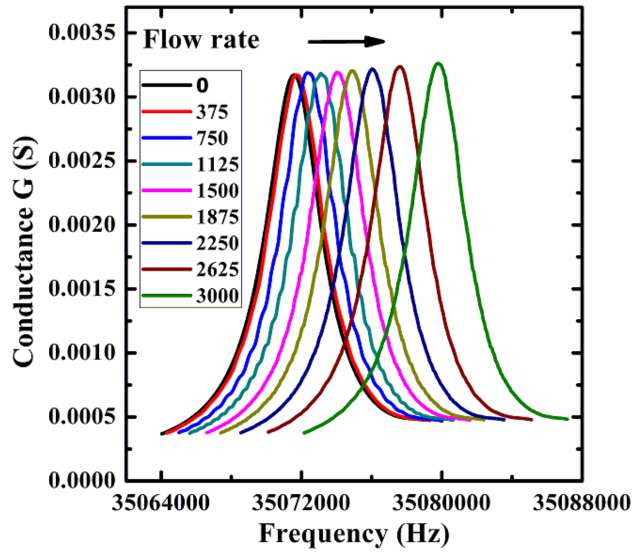

(d) 7th mode

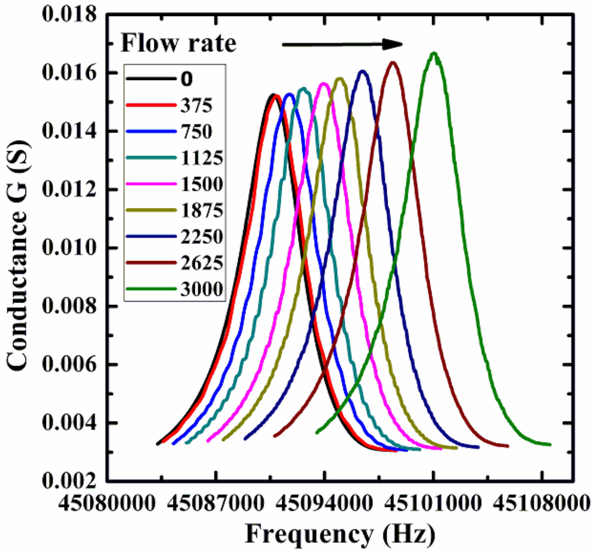

(e) 9th mode

Figure 4.8. Frequency shift of quartz resonator conductance spectrum under different flow rates (a) 1st mode; (b) 3rd mode; (c) 5th mode; (d) 7th mode; (e) 9th mode. Along the arrow direction, the flow rate increases from 0 to 3000 ml/min, and the conductance spectrum moves from left to right accordingly.

For flow measurement, nine different flow rates (0, 375, 750, 1125, 1500, 1875, 2250, 2625 and 3000 ml/min) were chosen in the acoustic wave flow sensor test by justifying the pumping speed in the water circulation setup. Figure 4.8 shows the frequency shifts for fundamental shear mode and higher order resonances of the quartz acoustic wave resonator under these flow rates. It can be seen that resonant frequency increases with flow rate. In addition, the peak value of conductance-frequency spectrum (*G* - *f*) has different trend to flow rate for different mode. For the fundamental mode, the peak decreases for the first 8 flow rates, and increase at the 9th flow rate. For 3rd, 5th and 7th modes, it seems that the G peak has not clear trend with flow rate. For 9th mode, the peak increases with the flow rate. Compared with conductance peak value, it is clear that the frequency shift is an indication of flow rate thus can be used as the sensor output for the acoustic wave flow sensor.

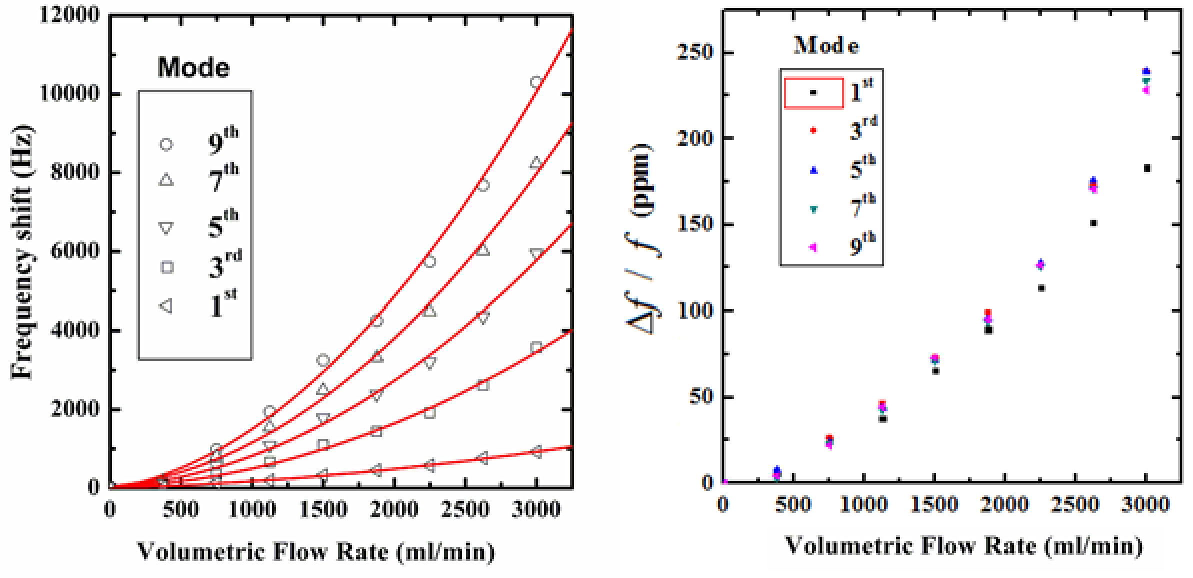

(a) (b)

Figure 4.9. Resonant frequency shifts of fundamental mode and overtones versus flow rate (a) absolute frequency shift; (b) fractional frequency shift

Figure 4.9 plots the results of different mode resonant frequency shifts versus flow rate. It is found that the resonant frequency shift has a nearly perfect quadratic relation with flow rate (shown in Figure 4.9 (a)), agreeing very well the prediction of Eq. (4.11). It is also found that the resonant frequency shifts of all the overtones are basically the same for a certain flow rate when compared in terms of fractional frequency shift ($\frac{\Delta f}{f}$), shown in Figure 4.9 (b), and the fundamental resonant frequency shift is a little lower than the overtones. For example, the fractional frequency shifts of fundamental and overtones (3rd, 5th, 7th and 9th) for a flow rate 2250 ml/min are found to be 118 ppm, 127.6 ppm, 127.7 ppm, 127.6 ppm and127.2 ppm.

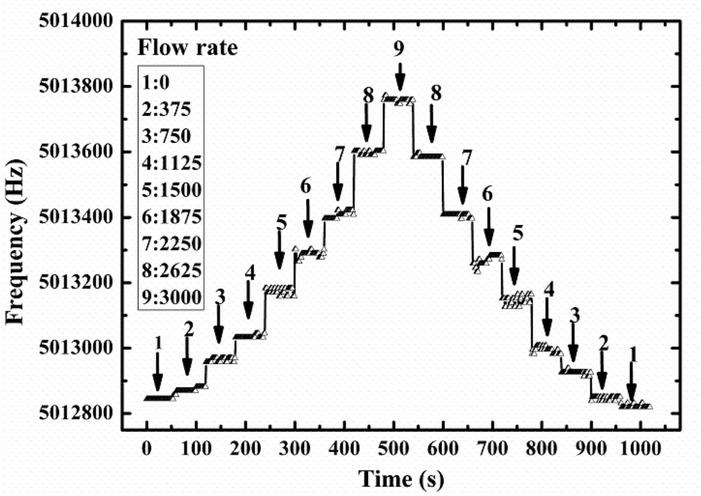

Figure 4.10. Repeatability of fundamental resonant frequency change under nine different flow rate levels

The repeatability of the resonator was also investigated. Nine flow rate levels were subsequently applied from 0 up to 3000 ml/min and from 3000 back to 0 ml/min. For each flow rate, the duration time is 1 minute, and the resonant frequencies were real- time monitored through a Labview program. Figure 4.10 plots the result of the fundamental shear mode resonant frequency shift with time. It can be seen that the resonator has an excellent repeatability for different flow rates. Variations of the frequency shift with time are also observed, particularly under 5th and 6th flow rate levels, which may reduce the output resolution of the acoustic wave flow sensor. This variation is mainly attributed to the flow rate instability in the flow path of the flow chamber. Another possible reason for this variation is the decrease of Q due to liquid load, which broadens the admittance spectrum and makes it more difficult in identifying the peak frequency of spectrum since the resonant frequency is extracted through searching the peak of conductance spectrum.

The experimental results indicate some attractive features of the TSM quartz acoustic wave flow sensor. One is its structural simplicity; no coating layer or other auxiliary sensing component is needed in the construction of the flow sensor cell. Another feature is that the operation of acoustic wave flow sensor is very simple: the frequency shift of the quartz resonator is a convenient output that can be easily read by a simple oscillator circuit and frequency counter. In addition, a wide range of flow rates can be measured by using the quartz acoustic wave flow sensor. Moreover, for many industrial applications, one is interested, not in the resolution of flow rate, but in the threshold of flow rate or pressure for monitoring the operational parameters of electromechanical or energy systems. Thus, compared with the conventional expensive and complex flow sensing devices, the acoustic wave flow sensor studied in this paper may provides an alternative method for flow rate monitoring with substantially simple sensor cell structure and low operation cost.

It should be noticed that before the practical implementation of this acoustic wave flow sensor, some issues need to be considered. Firstly, due to the unique of flow chamber geometry and the well-defined relation between the flow pressure and flow rate, the flow rate can be extracted by the measurement of pressure at one point using one quartz resonator. However, as shown in Eq. (4.4), the flow rate measurement is related to the outlet pressure (second term in Eq. (4.4)), which is unpredictable in real application. Thus, In order to get rid of the outlet pressure, the resonator side facing to the air before needs to connect with the outlet port, and Eq. (4.11) will be changed to

$$\frac{\Delta f}{f}=\left[\left(A_1+A_3\right)-\left(\frac{C_{21}+C_{23}}{C_{22}}\right)A_2\right]\frac{R^6}{6720D^2}\left(\frac{6\mu L}{h^3w(1-\frac{192h}{\pi^5 w}\sum_{n=1,3,5.....}^{\infty}\frac{1}{n^5}\tanh(\frac{n\pi w}{2h}))}\right)^2 \mathrm{Q}^2 \quad (4.13)$$

Now Δf is only dependant on Q and can be used for flow measurement when the flow chamber is plugged into the measured flow path.

Another option is to adopt two resonators configuration: If two same resonators are installed in the flow chamber with one side contacting liquid and another side exposed to air.

Assuming they are located at (x_1, $h/2$, 0) and (x_2, $h/2$, 0), then, according to Eq. (4.1) and (4.11) we can get:

$$Q = \frac{h^3 w}{12\mu}\left(-\frac{\mathrm{dp}}{\mathrm{dx}}\right)\left(1-\frac{192h}{\pi^5 w}\sum_{n=1,3,5.....}^{\infty}\frac{1}{n^5}\tanh\left(\frac{n\pi w}{2h}\right)\right)$$
$$= -\frac{h^3 w}{12\mu}\left(1-\frac{192h}{\pi^5 w}\sum_{n=1,3,5.....}^{\infty}\frac{1}{n^5}\tanh\left(\frac{n\pi w}{2h}\right)\right)\frac{P(x_2)-P(x_1)}{x_2-x_1} \qquad (4.14a)$$

$$\frac{\Delta f_1}{f_1} = \left[(A_1+A_3)-\left(\frac{C_{21}+C_{23}}{C_{22}}\right)A_2\right]\frac{R^6}{6720D^2}\Delta P_1^{\,2} \qquad (4.14b)$$

$$\frac{\Delta f_2}{f_2} = \left[(A_1+A_3)-\left(\frac{C_{21}+C_{23}}{C_{22}}\right)A_2\right]\frac{R^6}{6720D^2}\Delta P_2^{\,2} \qquad (4.14c)$$

where $P(x_i)$, ΔP_i and $\frac{\Delta f_i}{f_i}$ are pressure at $x = x_i$ in the flow channel, pressure difference on resonator two sides and fractional frequency shift of the resonator. It is easy to find:

$$P(x_2) - P(x_1) = \Delta P_2 - \Delta P_1 \qquad (4.15)$$

Combining Eq. (4.14) and (4.15), we obtain:

$$Q = -\frac{h^3 w}{12\mu(x_2-x_1)}\left(1-\frac{192h}{\pi^5 w}\sum_{n=1,3,5.....}^{\infty}\frac{1}{n^5}\tanh\left(\frac{n\pi w}{2h}\right)\right)\frac{\left(\sqrt{\frac{\Delta f_2}{f_2}}-\sqrt{\frac{\Delta f_1}{f_1}}\right)}{\sqrt{\left[(A_1+A_3)-\left(\frac{C_{21}+C_{23}}{C_{22}}\right)A_2\right]\frac{R^6}{6720D^2}}} \qquad (4.16)$$

From Eq. (4.16), we can see that flow measurement is independent on outlet pressure and Q can be read out by the frequency shift of two resonators.

Secondly, the sensitivity of the TSM quartz acoustic wave flow sensor seems not as high as the flow sensors based on SAW device, which has a frequency shift greater than 142 kHz (1900 ppm) for gas flow rate in the range from 0 to 1000 ml/min [49]. The experimental results in this work show for 1000 ml/min flow rate a frequency shift less 190 Hz (40 ppm) for the fundamental shear mode resonance and 2000 Hz (43 ppm) for the 9^{th} mode. This is due to that a nonlinear (second-order effect) frequency shift of quartz resonator is used for the signal transduction, which is usually much smaller than linear effect. The 9^{th} overtone has a frequency shift 10,300 Hz (228 ppm) for 3,000 ml/min flow rate, which is equal to 0.076 ppm/(ml/min). If we assume that the resonators have a temperature effect of 1ppm on the frequency shift, the calculated resolution is 13 ml/min. In addition, considering the effect of the liquid viscosity/density that may vary in a practical sense, the 13 ml/min resolution is generous.

Thirdly, since this acoustic wave flow sensor is based on the second order pressure-frequency effect, theoretically it is applicable to the flow rate measurement for any type of fluid such as air, oil and others; and other conduit materials and geometry such as round metal pipes, as long as the fluid pressure is not so high that the sensor is broken.

In addition, considering that the resonant behavior can be affected by the chemical reactions or physical adsorption occurring on the resonator electrode, the electrode facing the fluid needs to be protected, particularly when it is exposed to reactive or abrasive fluid. For this purpose, in the measurement of abrasive fluids the electrode material should be anti-abrasive or a protective thin film needs to be coated on the electrode of the resonator sensor. Further study is also needed to investigate the resonator behavior under higher pressure and determine the maximum pressure that the resonator can endure, since the highest pressure in the experiment study is about 6×10^4 Pa, which is not enough for some real applications where it can be up to a few or even tens of atmospheric pressure. Furthermore, it is well known that the flow is laminar and the velocity profile is parabolic for low Reynolds numbers (generally under 2,000), and the flow becomes turbulent for Reynolds numbers over 4,000. The Reynolds numbers of the current experiments spanned from 0 to 822, therefore, experiments at high Reynolds numbers are still needed to investigate the influence of the turbulent flow profile on the resonator response.

4.5 CONCLUSION

This study has demonstrated that quartz TSM resonator sensor can be used for laminar flow rate measurement with structural simplicity, fast response, and good repeatability. Both theoretical and experimental studies have indicated that the frequency shift of quartz resonator caused by fluid flow can be attributed to the nonlinear (quadratic) frequency response of device due to the normal pressure imposing on the sensor disk through the fluid flow. The resonant frequencies of different modes can be adopted as the sensor output for flow rate monitoring, and the fundamental, 3rd, 5th, 7th, and 9th resonant frequency shift was found to be around 920 (Hz), 3572 (Hz), 5947 (Hz), 8228 (Hz) and 10300 (Hz) for flow rate variation from 0 to 3000 ml/min or Reynolds number change from 0 to 822. For practical applications, the resonator side facing to the air needs to connect with the outlet port, or an extra resonator is installed, so that the flow rate measurement is not limited by the outlet pressure. In addition, considering that the resonant behavior can be affected by the chemical reactions or physical adsorption occurring on the resonator electrode, the electrode facing the fluid may need to be protected, particularly when it is exposed to reactive or abrasive fluids. Further experiment studies under higher pressure and high Reynolds numbers are needed to determine the pressure limit and the flow profile influence on resonator response.

5.0 ANALYTICAL STUDY OF DUAL MODE RESONATORS BASED ON ZNO AND ALN FILMS WITH TILTED C-AXIS ORIENTATION

5.1 INTRODUCTION

Recently, in the RF and microwave frequency control and signal processing field FBARs have received great attention due to their small size, low insertion loss and power consumption [71-75]. Especially, filters based on AlN FBARs which can be operated in low and medium GHZ range, have been fabricated for signal processing and communication devices [76-78]. Also, FBARs show good promising in sensor application. In the case of mass sensor application as the quartz micro-balance (QCM), it is well known that the resonant frequency will change due to surface mass change, and the absolute frequency is proportional to the square of the operating frequency. Therefore, using FBAR structures, whose operation frequency can be high to tens of GHz, can greatly improve the sensor sensitivity. For example, ZnO and AlN FBARs have shown much higher sensitivity and resolution comparable to QCM as biosensors for DNA and protein molecules detection [13], chemical sensors for ion detection such as K^+ [14], and gas sensors for low concentration detection of H_2, CO and ethanol [15].

FBARs mentioned above are usually operated in longitudinal mode. For sensor application in liquid, the performance of thickness longitudinal mode FBARs will be adversely affected because the acoustic wave energy is radiated into liquid through compressional motion, resulting in excessive damping of resonator [79]. On the other hand, shear acoustic waves do not produce compressional motion and thus are relatively undamped by liquid. Therefore, shear mode is a preferred choice for liquid operation of FBAR, just as the operation of QCM [2]. Now the question becomes what kind of AlN or ZnO thin films can excite the shear mode.

In recent studies, it has been shown that thickness shear mode resonance can be excited in piezoelectric thin films with tilted c-axis (polarization off-normal) orientations. Foster et al. theoretically and experimentally analyzed the excitation of longitudinal and shear wave in ZnO transducer, which showed the shear-wave excitation greatly exceeded the longitudinal wave excitation when the c-axis was inclined at angles near 40^0 [16]. Wittstruck et al. reported the fabrication of the $Mg_xZn_{1-x}O$ through metal organic chemical vapor deposition (MOCVD); the c-axis of the $Mg_xZn_{1-x}O$ film was lying in the plane surface, providing a possibility for thickness shear wave sensing in a liquid environment [80]. Yanagitani et al. reported pure thickness shear mode FBARs made of $(10\bar{1}0)$ and $(11\bar{2}0)$ textured ZnO films [81, 82]. Link et al fabricated SMRs using 18° c-axis inclined ZnO thin films; mechanical quality factors of 192 were determined in water, indicating these devices attractive for sensing applications in liquids [17].Wu et al. theoretically analyzed bulk acoustic wave properties of all crystalline plane oriented sputtered and epitaxial ZnO films using Christoffel equation; it showed that different crystalline plane oriented ZnO films formed different acoustic wave modes and properties [83].

In the case of AlN, Bjurström and Wingqvist et al. investigated a sputtering system to achieve c-axis tilted AlN films; the variation of the electromechanical coupling coefficient and the quality factor of FBARs based on these c-axis tilted AlN films were examined; combined with a micro-fluidic transport system these FBARs were investigated for liquid applications [18-21]. Martin et al. presented solidly mounted FBARs based on c-axis tilted AlN films; the resonant frequencies of resonators could be high to around 8GHz for longitudinal mode and 4 GHz for shear mode [84, 85]. Chuang et al. fabricated SMRs using 0^0,15^0 and 30^0 c-axis tilted AlN films, and experimentally investigated the effect of mass loading on the resonators [86]. Chen et al. analyzed the input impedance of a dual mode AlN FBAR by ignoring the coupling of longitudinal and shear mode, which showed the coexistence of dual mode was dependent on the tilt angle [87].

In this study, we presented the theoretical analysis of thickness longitudinal and thickness shear dual-mode FBARs based on c-axis tilted ZnO and AlN films. Following a similar procedure [16], the equation for predicting electric impedance of FBARS was derived by the basic piezoelectric equations. The material properties including elastic, dielectric and piezoelectric constants were calculated with a tilt angle range from 0^0 to 180^0, which were used to determine the bulk wave properties of films including acoustic velocity and electromechanical coupling coefficient. The response of dual mode resonator was compared with reported experiment results. And the mass sensitivity of FBARs was analyzed through the calculation of resonant frequency shift for small mass loading.

5.2 THEORY

5.2.1 Dual mode FBARs

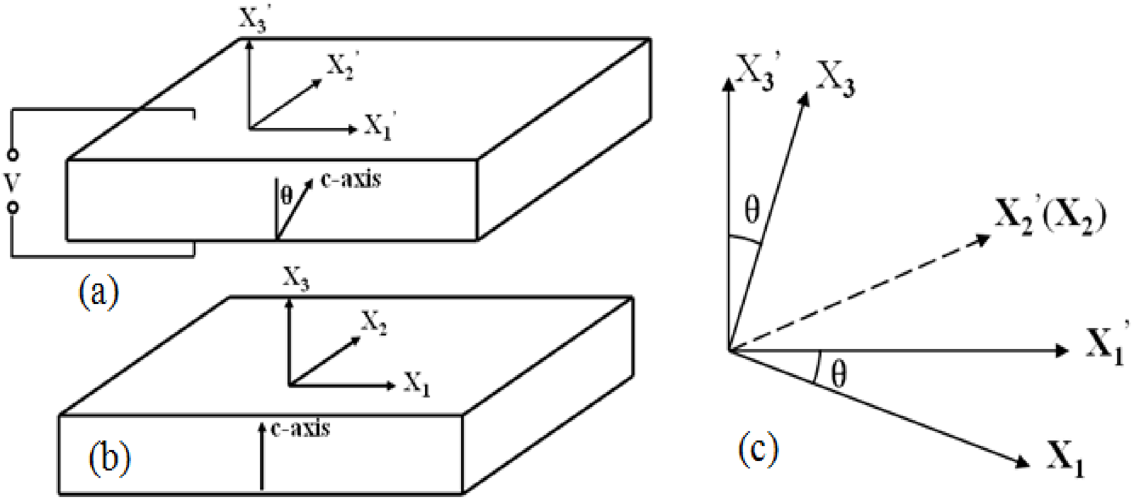

Figure 5.1. The schematic of FBAR and coordinate systems. (a) Schematic of FBAR and $(x_1^{'}, x_2^{'}, x_3^{'})$ coordinate system; (b) (x_1, x_2, x_3) coordinate system; (c) the relation of $(x_1^{'}, x_2^{'}, x_3^{'})$ and (x_1, x_2, x_3) coordinate system

Figure 5.1(a) shows the schematic of tilted c-axis ZnO or AlN FBARs, where the top and bottom electrode are ignored. A rectangular Cartesian coordinate system ($x_1^{'}, x_2^{'}, x_3^{'}$) was chosen with top electrode on $x_3^{'} = h$ and bottom electrode on $x_3^{'} = 0$. The c-axis of ZnO or AlN films is tilted at an angle θ to the $x_3^{'}$ direction. Figure 5.1(b) shows the c-axis normal coordinate (x_1, x_2, x_3). Coordinate system ($x_1^{'}, x_2^{'}, x_3^{'}$) can be treated as the result of rotation of (x_1, x_2, x_3) about x_2 with an angle θ, as shown in Figure 5.1(c).

5.2.2 Material properties of ZnO and AlN films

For the characterization of tilted c-axis ZnO or AlN FBARs, the material properties in ($x_1^{'}$, $x_2^{'}$, $x_3^{'}$) need to be known. Assuming the dielectric permittivity, piezoelectric stress coefficient and elastic stiffness are ($\varepsilon^{'}$, $e^{'}$, $c^{'}$) for coordinate system ($x_1^{'}$, $x_2^{'}$, $x_3^{'}$), and (ε, e, c) for coordinate system (x_1, x_2, x_3), the material properties in new coordinate system can be computed through properties in original coordinate system with the aids of matrix algebra [88]:

$$\varepsilon^{'} = a\varepsilon a^{t} \tag{5.1}$$

$$e^{'} = aeM^{t} \tag{5.2}$$

$$c^{'} = McM^{t} \tag{5.3}$$

$$a = \begin{bmatrix} a_{11} & a_{12} & a_{13} \\ a_{21} & a_{22} & a_{23} \\ a_{31} & a_{32} & a_{33} \end{bmatrix} = \begin{bmatrix} \cos(\theta) & 0 & \sin(\theta) \\ 0 & 1 & 0 \\ -\sin(\theta) & 0 & \cos(\theta) \end{bmatrix} \tag{5.4}$$

$$M = \begin{bmatrix} a_{11}^2 & a_{12}^2 & a_{13}^2 & 2a_{12}a_{13} & 2a_{11}a_{13} & 2a_{11}a_{12} \\ a_{21}^2 & a_{22}^2 & a_{23}^2 & 2a_{22}a_{23} & 2a_{21}a_{23} & 2a_{21}a_{22} \\ a_{31}^2 & a_{32}^2 & a_{33}^2 & 2a_{32}a_{33} & 2a_{31}a_{33} & 2a_{31}a_{32} \\ a_{21}a_{31} & a_{22}a_{32} & a_{23}a_{33} & a_{22}a_{33}+a_{23}a_{32} & a_{21}a_{33}+a_{23}a_{31} & a_{21}a_{32}+a_{22}a_{31} \\ a_{11}a_{31} & a_{12}a_{32} & a_{13}a_{33} & a_{12}a_{33}+a_{13}a_{32} & a_{11}a_{33}+a_{13}a_{31} & a_{11}a_{32}+a_{12}a_{31} \\ a_{11}a_{21} & a_{12}a_{22} & a_{13}a_{23} & a_{12}a_{23}+a_{13}a_{22} & a_{11}a_{23}+a_{13}a_{21} & a_{11}a_{22}+a_{12}a_{21} \end{bmatrix} \tag{5.5}$$

where θ is the tilt angle, a^{t} is the transpose of a, and M^{t} is the transpose of M.

5.2.3 Impedance of FBARs

According to the acoustic field equations and piezoelectric constitution equations [88, 89], we have:

$$\begin{bmatrix} \dfrac{\partial}{\partial x_1^{'}} & 0 & 0 & 0 & \dfrac{\partial}{\partial x_3^{'}} & \dfrac{\partial}{\partial x_2^{'}} \\ 0 & \dfrac{\partial}{\partial x_2^{'}} & 0 & \dfrac{\partial}{\partial x_3^{'}} & 0 & \dfrac{\partial}{\partial x_1^{'}} \\ 0 & 0 & \dfrac{\partial}{\partial x_3^{'}} & \dfrac{\partial}{\partial x_2^{'}} & \dfrac{\partial}{\partial x_1^{'}} & 0 \end{bmatrix} \begin{bmatrix} T_1 \\ T_2 \\ T_3 \\ T_4 \\ T_5 \\ T_6 \end{bmatrix} = \rho \begin{bmatrix} \dfrac{\partial^2 u_1}{\partial t^2} \\ \dfrac{\partial^2 u_2}{\partial t^2} \\ \dfrac{\partial^2 u_3}{\partial t^2} \end{bmatrix} \tag{5.6}$$

$$\begin{bmatrix} S_1 \\ S_2 \\ S_3 \\ S_4 \\ S_5 \\ S_6 \end{bmatrix} = \begin{bmatrix} \partial / \partial x_1^{'} & 0 & 0 \\ 0 & \partial / \partial x_2^{'} & 0 \\ 0 & 0 & \partial / \partial x_3^{'} \\ 0 & \partial / \partial x_3^{'} & \partial / \partial x_2^{'} \\ \partial / \partial x_3^{'} & 0 & \partial / \partial x_1^{'} \\ \partial / \partial x_2^{'} & \partial / \partial x_1^{'} & 0 \end{bmatrix} \begin{bmatrix} u_1 \\ u_2 \\ u_3 \end{bmatrix} \tag{5.7}$$

$$T_p = c_{pq}^{E\,'} S_q - e_{kp}^{'} E_k \tag{5.8}$$

$$D_i = e_{iq}^{'} S_q + \varepsilon_{ik}^{S\,'} E_k \tag{5.9}$$

where T_p, S_q, D_i and E_k are the components of stress, strain, electric displacement and electric field intensity, $c_{pq}^{E\,'}$ are the elastic stiffness constants under constant electric field intensity, $e_{kp}^{'}$ are the piezoelectric stress constants, $\varepsilon_{ik}^{S\,'}$ are the permittivity constants under constant strain, and u_i is the displacement in the direction of $x_i^{'}$ ($i, k = 1, 2, 3$ and $p, q = 1, 2, 3, 4, 5, 6$). Since the thickness of the piezoelectric layer is much smaller than the lateral dimensions, the thickness vibration of the resonator can be treated as a one-dimensional problem; hence, we may have:

$$\frac{\partial T_i}{\partial x_1^{'}} = \frac{\partial T_i}{\partial x_2^{'}} = 0 \tag{5.10a}$$

$$E_1 = E_2 = 0, E_3 \neq 0 \tag{5.10b}$$

$$\frac{\partial D_3}{\partial x_3^{'}} = 0 \tag{5.11}$$

From (5.6) - (5.10), we can obtain:

$$T_4 = c_{44}^{E'} \frac{\partial u_2}{\partial x_3'} + c_{34}^{E'} \frac{\partial u_3}{\partial x_3'} + c_{45}^{E'} \frac{\partial u_1}{\partial x_3'} - e_{34}' E_3 \tag{5.12}$$

$$\frac{\partial T_4}{\partial x_3'} = \rho \frac{\partial^2 u_2}{\partial t^2} \tag{5.13}$$

$$T_5 = c_{55}^{E'} \frac{\partial u_1}{\partial x_3'} + c_{35}^{E'} \frac{\partial u_3}{\partial x_3'} + c_{45}^{E'} \frac{\partial u_2}{\partial x_3'} - e_{35}' E_3 \tag{5.14}$$

$$\frac{\partial T_5}{\partial x_3'} = \rho \frac{\partial^2 u_1}{\partial t^2} \tag{5.15}$$

$$T_3 = c_{33}^{E'} \frac{\partial u_3}{\partial x_3'} + c_{35}^{E'} \frac{\partial u_1}{\partial x_3'} + c_{34}^{E'} \frac{\partial u_2}{\partial x_3'} - e_{33}' E_3 \tag{5.16}$$

$$\frac{\partial T_3}{\partial x_3'} = \rho \frac{\partial^2 u_3}{\partial t^2} \tag{5.17}$$

$$D_3 = e_{35}' \frac{\partial u_1}{\partial x_3'} + e_{34}' \frac{\partial u_2}{\partial x_3'} + e_{33}' \frac{\partial u_3}{\partial x_3'} + \varepsilon_{33}^{S'} E_3 \tag{5.18}$$

For any tilt angle θ, it is found:

$$c_{34}^{E'} = c_{45}^{E'} = e_{34}{}' = 0 \tag{5.19}$$

From (12), (13) and (19), we can see that u_2 is uncoupled with u_1, u_3 and E_3; hence u_2 needn't to be considered and can be set to 0 in this one dimension problem. Substituting (5.14) into (5.15) and substituting (5.16) into (5.17), we have:

$$\overline{c_{55}^{E'}} \frac{\partial^2 u_1}{\partial x_3'^2} + \overline{c_{35}^{E'}} \frac{\partial^2 u_3}{\partial x_3'^2} = \rho \frac{\partial^2 u_1}{\partial t^2} \tag{5.20}$$

$$\overline{c_{33}^{E'}} \frac{\partial^2 u_3}{\partial x_3'^2} + \overline{c_{35}^{E'}} \frac{\partial^2 u_1}{\partial x_3'^2} = \rho \frac{\partial^2 u_3}{\partial t^2} \tag{5.21}$$

where

$$\overline{c_{33}^{E'}} = c_{33}^{E'} + \frac{\left(e_{33}^{'}\right)^2}{\varepsilon_{33}^{S'}} \tag{5.22a}$$

$$\overline{c_{35}^{E'}} = c_{35}^{E'} + \frac{e_{33}^{'}e_{35}^{'}}{\varepsilon_{33}^{S'}} \tag{5.22b}$$

$$\overline{c_{55}^{E'}} = c_{55}^{E'} + \frac{\left(e_{35}^{'}\right)^2}{\varepsilon_{33}^{S'}} \tag{5.22c}$$

For a sinusoidal excitation, the solution to (5.20) and (5.21) is given by

$$\begin{bmatrix} u_1 \\ u_3 \end{bmatrix} = \begin{bmatrix} \sin(\alpha) & \cos(\alpha) \\ \cos(\alpha) & -\sin(\alpha) \end{bmatrix} \begin{bmatrix} u_L \\ u_S \end{bmatrix} \tag{5.23a}$$

$$u_L = (A_L \sin(\omega x_3^{'} / v^{(L)}) + B_L \cos(\omega x_3^{'} / v^{(L)})e^{jwt} \tag{5.23b}$$

$$u_S = (A_S \sin(\omega x_3^{'} / v^{(S)}) + B_S \cos(\omega x_3^{'} / v^{(S)}))e^{jwt} \tag{5.23c}$$

where

$$w = 2\pi f \tag{5.24a}$$

$$\alpha = \frac{1}{2}\arctan\left(\frac{2\overline{c_{35}^{E'}}}{\overline{c_{33}^{E'}} - \overline{c_{55}^{E'}}}\right) \tag{5.24b}$$

$$v^{(L)} = \left[\frac{\overline{c_{33}^{E'}} + \overline{c_{55}^{E'}}}{2\rho} + \sqrt{\left(\frac{\overline{c_{33}^{E'}} - \overline{c_{55}^{E'}}}{2\rho}\right)^2 + \left(\frac{\overline{c_{35}^{E'}}}{\rho}\right)^2}\right]^{1/2} \tag{5.24c}$$

$$v^{(S)} = \left[\frac{\overline{c_{33}^{E'}} + \overline{c_{55}^{E'}}}{2\rho} - \sqrt{\left(\frac{\overline{c_{33}^{E'}} - \overline{c_{55}^{E'}}}{2\rho}\right)^2 + \left(\frac{\overline{c_{35}^{E'}}}{\rho}\right)^2}\right]^{1/2} \tag{5.24d}$$

f is the excitation frequency, $v^{(L)}$ and $v^{(S)}$ are the acoustic velocities for longitudinal mode and shear mode respectively, and A_L, B_L, A_S, B_S are the unknown amplitudes determined by the boundary conditions. The stress can be solved through substituting (5.23), (5.24) into (5.14), (5.16), given by

$$\begin{bmatrix} T_5 \\ T_3 \end{bmatrix} = \begin{bmatrix} \sin(\alpha) & \cos(\alpha) \\ \cos(\alpha) & -\sin(\alpha) \end{bmatrix} \begin{bmatrix} T_L \\ T_S \end{bmatrix} \tag{5.25a}$$

$$T_L = wZ_L(A_L \cos(\omega x_3^{'} / v^{(L)}) - B_L \sin(\omega x_3^{'} / v^{(L)}))e^{jwt} - (\frac{e_L}{\varepsilon_{33}^{S'}})D_3 \tag{5.25b}$$

$$T_S = wZ_S(A_S \cos(\omega x_3^{'} / v^{(S)}) - B_S \sin(\omega x_3^{'} / v^{(S)}))e^{jwt} - \left(\frac{e_S}{\varepsilon_{33}^{S'}}\right)D_3 \tag{5.25c}$$

where

$$Z_L = \rho v^{(L)} \tag{5.26a}$$

$$Z_S = \rho v^{(S)} \tag{5.26b}$$

$$e_L = e_{35}^{'} \sin(\alpha) + e_{33}^{'} \cos(\alpha) \tag{5.26c}$$

$$e_S = e_{35}^{'} \cos(\alpha) - e_{33}^{'} \sin(\alpha) \tag{5.26d}$$

The voltage across the piezoelectric layer is found from (5.11), (5.18), (5.26c) and (5.26d) to be

$$\begin{aligned} V &= \int_0^h E_3 dx_3^{'} \\ &= -\frac{e_L}{\varepsilon_{33}^{S'}}[u_L(h) - u_L(0)] - \frac{e_S}{\varepsilon_{33}^{S'}}[u_S(h) - u_S(0)] + \frac{D_3 h}{\varepsilon_{33}^{S'}} \end{aligned} \tag{5.27}$$

where A is the area of the electrodes. The current I can be expressed by

$$I = \frac{dQ}{dt} = jwAD_3 \tag{5.28}$$

The traction force at the boundary ($x_3^{'} = 0, h$) is zero, thus we have:

$$T_5(0) = T_5(h) = T_3(0) = T_3(h) = 0 \tag{5.29}$$

Using (5.23), (5.25) and (5.29) we find that

$$u_L(h) - u_L(0) = \frac{2e_L D_3 \tan(\frac{\omega h}{2v^{(l)}})}{wZ_L \varepsilon_{33}^{S\,'}} \tag{5.30a}$$

$$u_S(h) - u_S(0) = \frac{2e_S D_3 \tan(\frac{\omega h}{2v^{(S)}})}{wZ_S \varepsilon_{33}^{S\,'}} \tag{5.30b}$$

Hence, substituting (5.30) into (5.27) and using (5.28) the impedance of FBAR is found that

$$Z = \frac{V}{I} = \frac{1}{j\omega C_0}(1 - k_L^2 \frac{\tan(\gamma_L / 2)}{\gamma_L / 2} - k_S^2 \frac{\tan(\gamma_S / 2)}{\gamma_S / 2}) \tag{5.31}$$

where

$$\gamma_L = \frac{\omega h}{v^{(L)}} \tag{5.32a}$$

$$\gamma_S = \frac{\omega h}{v^{(S)}} \tag{5.32b}$$

$$C_0 = \varepsilon_{33}^{S\,'} A / h \tag{5.32c}$$

$$k_L{}^2 = \frac{(e_L)^2}{\varepsilon_{33}^{S\,'} \rho (v^{(L)})^2} \tag{5.32d}$$

$$k_S{}^2 = \frac{(e_S)^2}{\varepsilon_{33}^{S\,'} \rho (v^{(S)})^2} \tag{5.32e}$$

Here, k_L and k_S are respectively defined as the electromechanical coupling coefficient for the longitudinal and shear mode.

5.3 RESULTS AND DISCUSSION

5.3.1 Dependence of ZnO and AlN material properties on the tilt angle θ

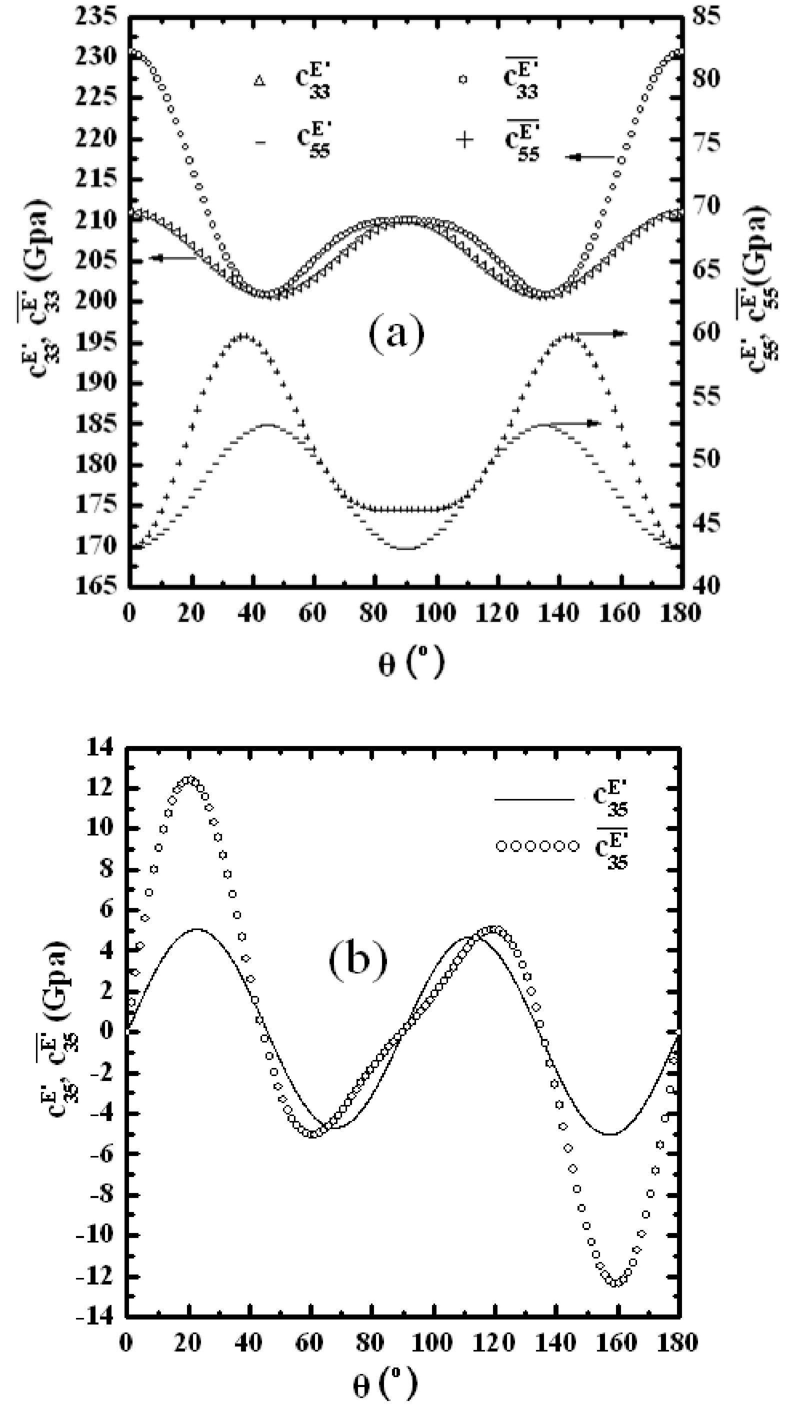

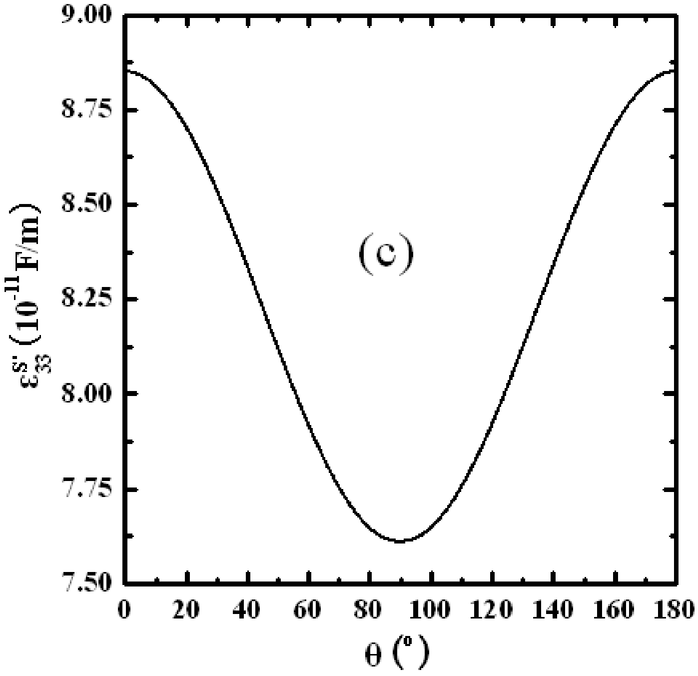
9.00
8.75
8.50
8.25
8.00
7.75
7.50
0
20
40
60
80
100
120
140
160
180
$\varepsilon_{33}^{S'}$ (10^{-11}F/m)
(c)
θ (°)

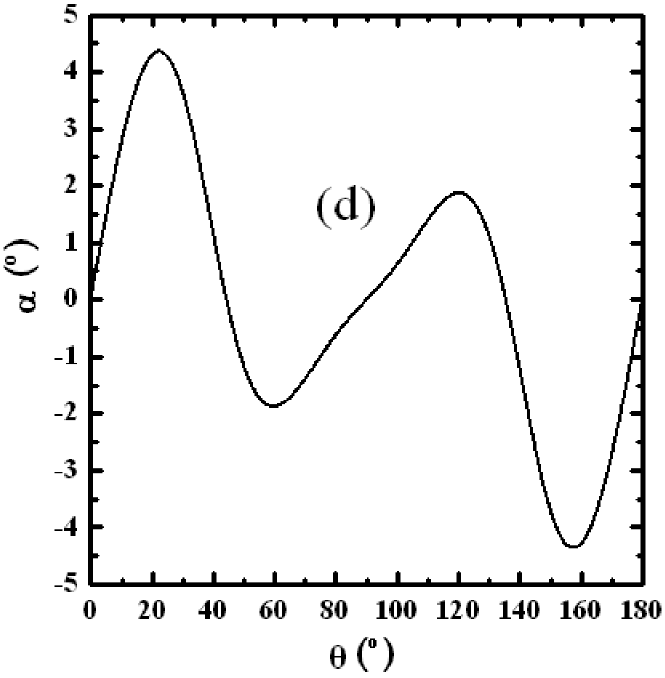
5
4
3
2
1
0
-1
-2
-3
-4
-5
0
20
40
60
80
100
120
140
160
180
α (°)
(d)
θ (°)

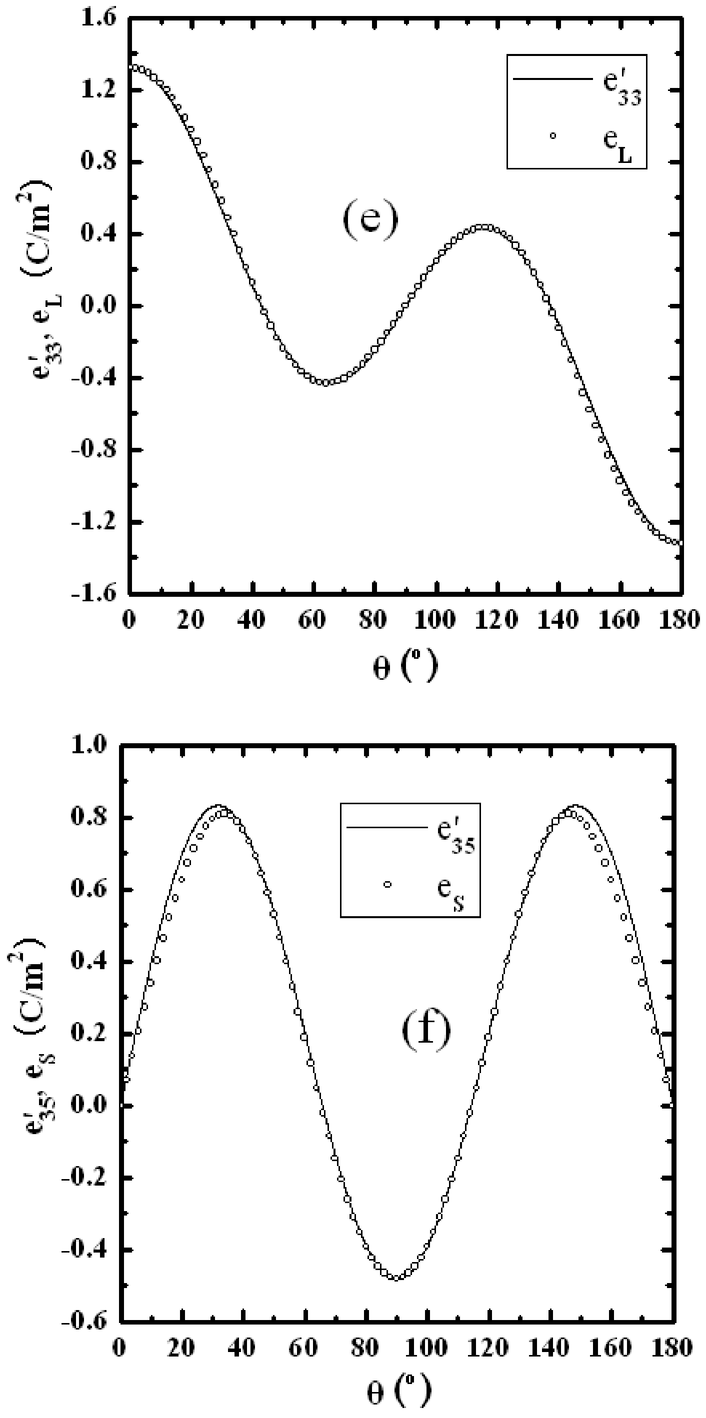

Figure 5.2. ZnO material properties and effective parameters in $(x_1^{'}, x_2^{'}, x_3^{'})$ coordinate system. (a) $c_{33}^{E'}$, $\overline{c_{33}^{E'}}$, $c_{55}^{E'}$ and $\overline{c_{55}^{E'}}$; (b) $c_{35}^{E'}$ and $\overline{c_{35}^{E'}}$; (c) $\varepsilon_{33}^{S'}$; (d) α; (e) $e_{33}^{'}$ and e_L; (f) $e_{35}^{'}$ and e_S

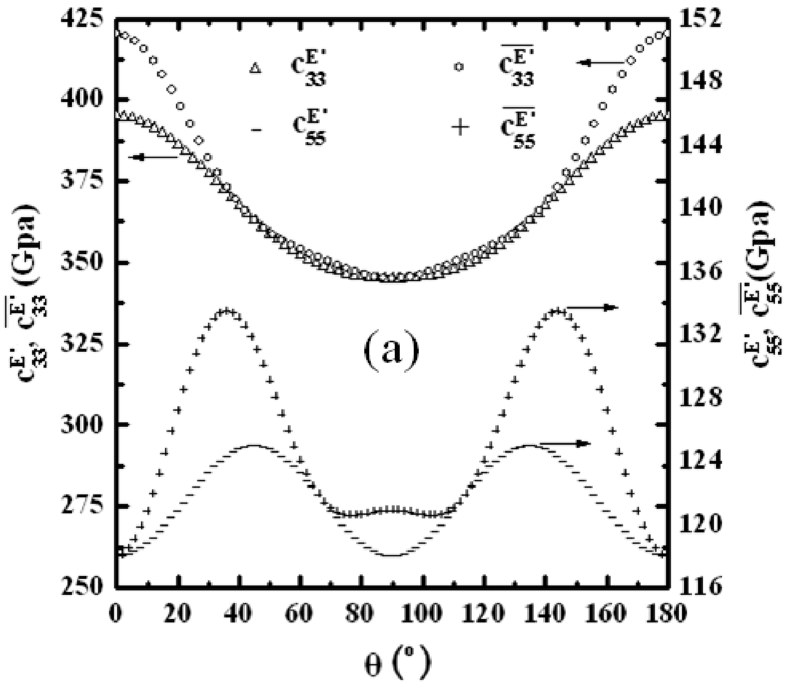
(a)
$c_{33}^{E'}$
$\overline{c_{33}^{E'}}$
$c_{55}^{E'}$
$\overline{c_{55}^{E'}}$
$c_{33}^{E'}$, $\overline{c_{33}^{E'}}$ (Gpa)
$c_{55}^{E'}$, $\overline{c_{55}^{E'}}$ (Gpa)
θ (°)
425
400
375
350
325
300
275
250
152
148
144
140
136
132
128
124
120
116
0
20
40
60
80
100
120
140
160
180

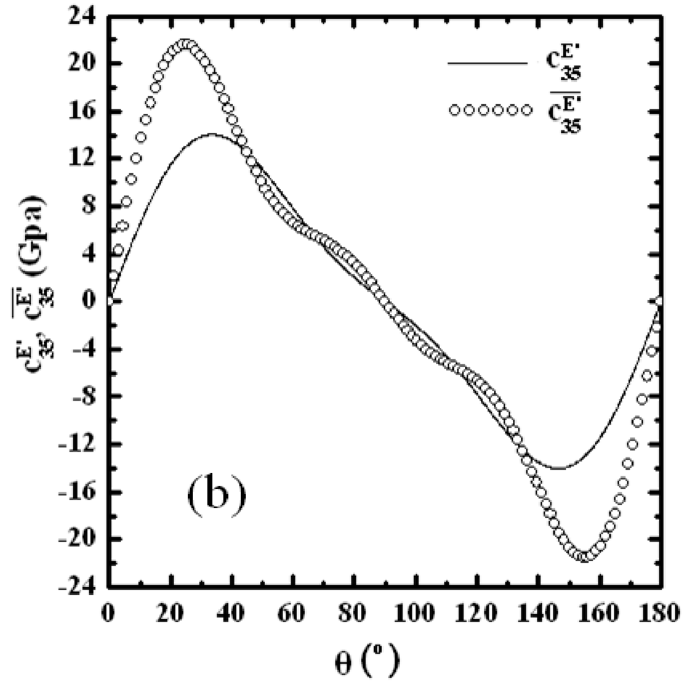
(b)
$c_{35}^{E'}$
$\overline{c_{35}^{E'}}$
$c_{35}^{E'}$, $\overline{c_{35}^{E'}}$ (Gpa)
θ (°)
24
20
16
12
8
4
0
-4
-8
-12
-16
-20
-24
0
20
40
60
80
100
120
140
160
180

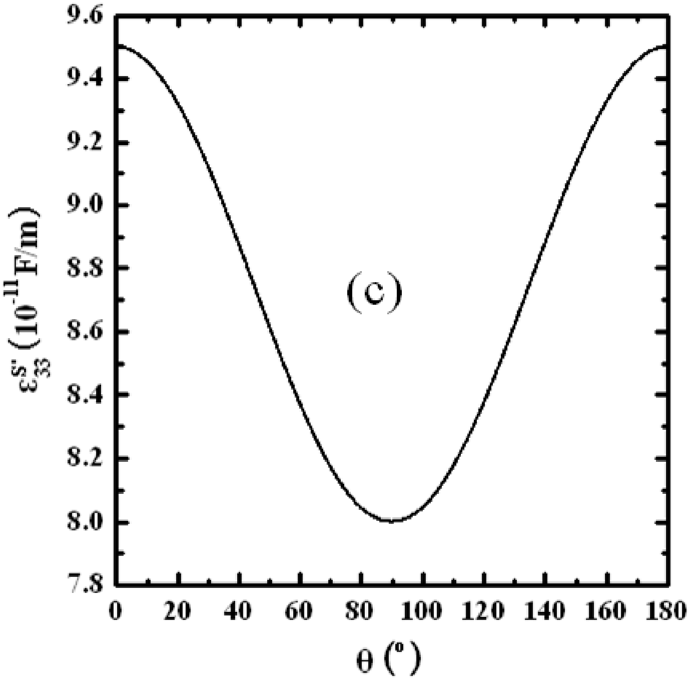

(c)
$\varepsilon_{33}^{S'}$ (10^{-11}F/m)
9.6
9.4
9.2
9.0
8.8
8.6
8.4
8.2
8.0
7.8
0 20 40 60 80 100 120 140 160 180
θ (°)

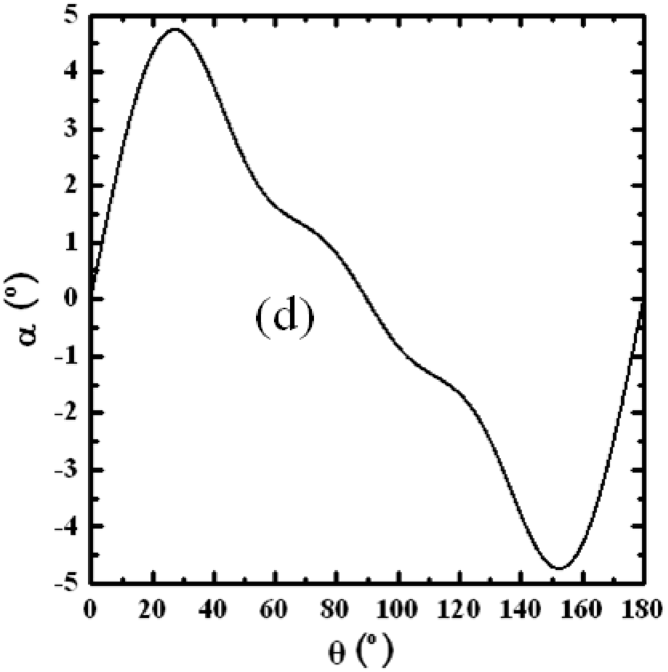

(d)
α (°)
5
4
3
2
1
0
-1
-2
-3
-4
-5
0 20 40 60 80 100 120 140 160 180
θ (°)

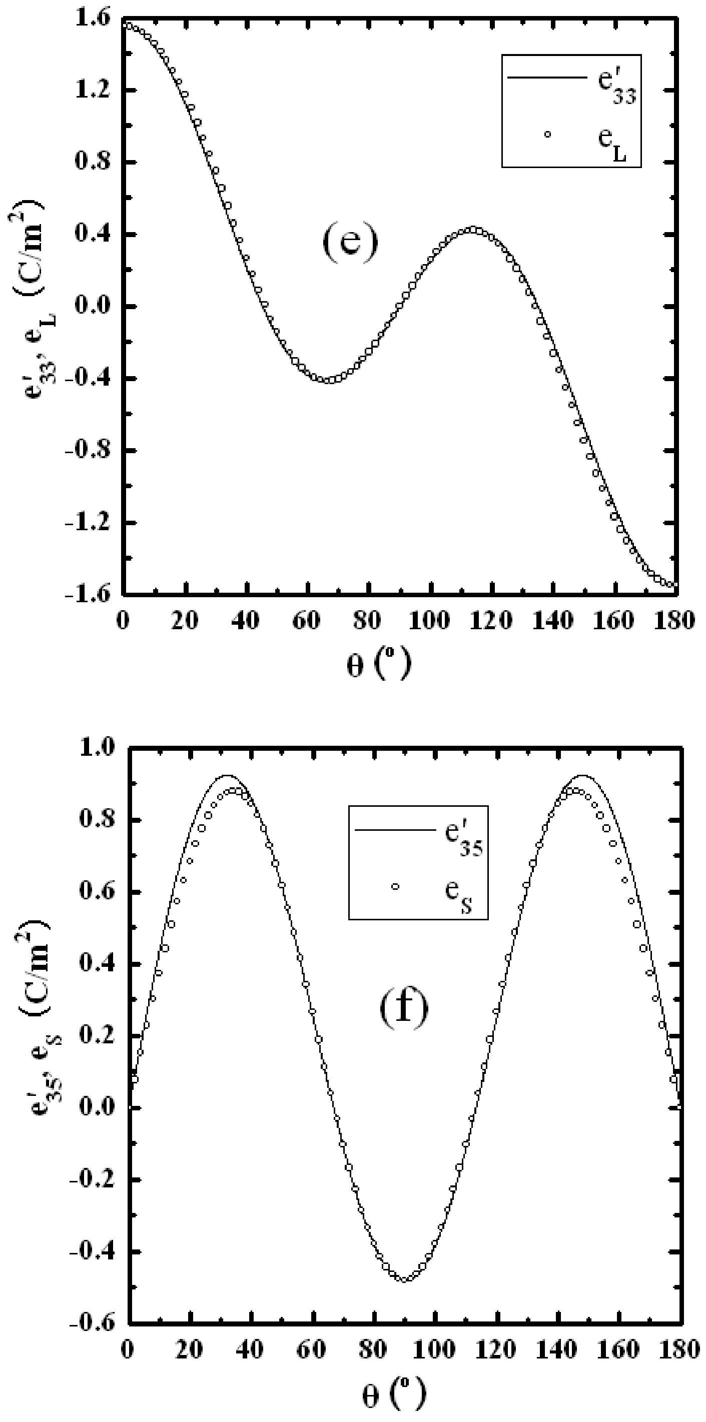

Figure 5.3. AlN material properties and effective parameters in (x_1', x_2', x_3') coordinate system. (a) $c_{33}^{E'}$, $\overline{c_{33}^{E'}}$, $c_{55}^{E'}$ and $\overline{c_{55}^{E'}}$; (b) $c_{35}^{E'}$ and $\overline{c_{35}^{E'}}$; (c) $\varepsilon_{33}^{S'}$; (d) α; (e) e_{33}' and e_L; (f) e_{35}' and e_S

The material properties of ZnO [90, 91] and AlN [92] in (x_1, x_2, x_3) coordinate system are listed in Table 5.1.

Table 5.1. Material properties of ZnO and AlN

Property		AlN	ZnO
Density (Kg/cm^3)	ρ	3260	5700
Elastic stiffness (Gpa) $c^E = \begin{bmatrix} c_{11} & c_{12} & c_{13} & 0 & 0 & 0 \\ c_{12} & c_{11} & c_{13} & 0 & 0 & 0 \\ c_{13} & c_{13} & c_{33} & 0 & 0 & 0 \\ 0 & 0 & 0 & c_{44} & 0 & 0 \\ 0 & 0 & 0 & 0 & c_{44} & 0 \\ 0 & 0 & 0 & 0 & 0 & c_{66} \end{bmatrix}$	c_{11}^E	345	210
	c_{12}^E	125	121
	c_{13}^E	120	105
	c_{33}^E	395	211
	c_{44}^E	118	43.0
	c_{66}^E	110	44.5
Piezoelectric stress constant (C/m^2) $e = \begin{bmatrix} 0 & 0 & 0 & 0 & e_{15} & 0 \\ 0 & 0 & 0 & e_{15} & 0 & 0 \\ e_{31} & e_{31} & e_{33} & 0 & 0 & 0 \end{bmatrix}$	e_{31}	-0.58	-0.57
	e_{33}	1.55	1.32
	e_{15}	-0.48	-0.48
Dielectric permittivity (10^{-11}F/m) $\varepsilon^S = \begin{bmatrix} \varepsilon_{11}^S & 0 & 0 \\ 0 & \varepsilon_{11}^S & 0 \\ 0 & 0 & \varepsilon_{33}^S \end{bmatrix}$	ε_{11}^S	8.0	7.61
	ε_{33}^S	9.5	8.85

Using (5.1)-(5.5), (5.22), (5.26c) and (5.26d), the material properties and effective parameters in $(x_1^{'}, x_2^{'}, x_3^{'})$ coordinate system are calculated and shown in Figure 5.2 and Figure 5.3, which can clearly show that elastic stiffness, dielectric permittivity and piezoelectric coefficient are tilt angle dependent. According to (5.22), $\overline{c_{33}^{E'}}$ and $\overline{c_{55}^{E'}}$ can be regarded as piezoelectrically stiffened $c_{33}^{E'}$ and $c_{55}^{E'}$, respectively; and have larger values as shown in Figure 5.2(a) and Figure 5.3(a). The value of $\overline{c_{35}^{E'}}$, as shown in Figure 5.2(b) and Figure 5.3(b), is much smaller compared with

$\overline{c_{33}^{E'}}$ and $\overline{c_{55}^{E'}}$, which induces the calculated angle α through (5.24 b) very small, in a range of 0°-5° shown in Figure 5 2(d) and Figure 5.3(d). The small value of α makes the calculated e_L and e_S through (5.26) much close to $e_{33}^{'}$ and $e_{55}^{'}$, respectively, which can be clearly seen from Figure 5.2(e), 5.2(f) and Figure 5.3(e), 5.3(f). The calculated $\varepsilon_{33}^{S'}$, as shown in Figure 5.2(c) and Figure 5.3(c), varies from 7.61×10^{-11} to 8.85×10^{-11} F/m for ZnO and 8.00×10^{-11} to 9.50×10^{-11} F/m for AlN, respectively.

5.3.2 Bulk acoustic wave properties of ZnO and AlN

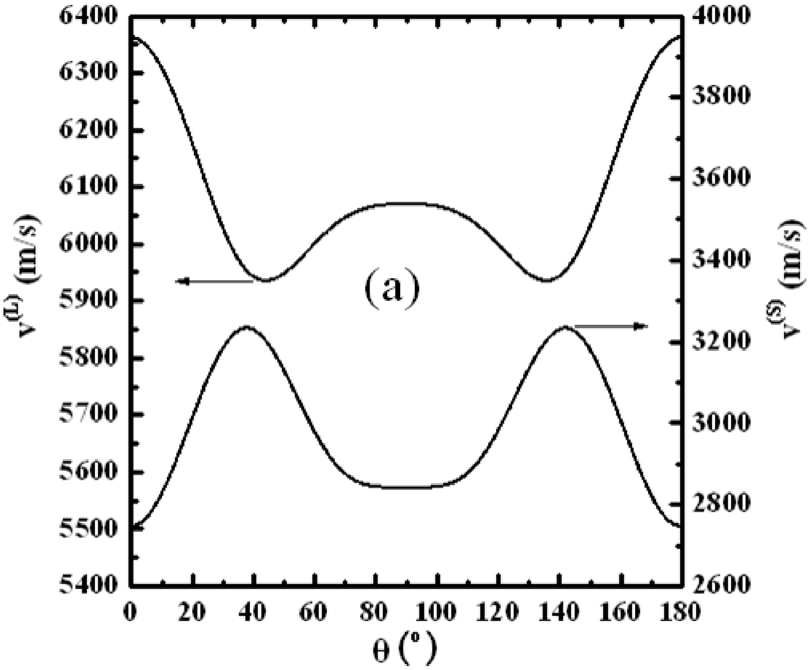

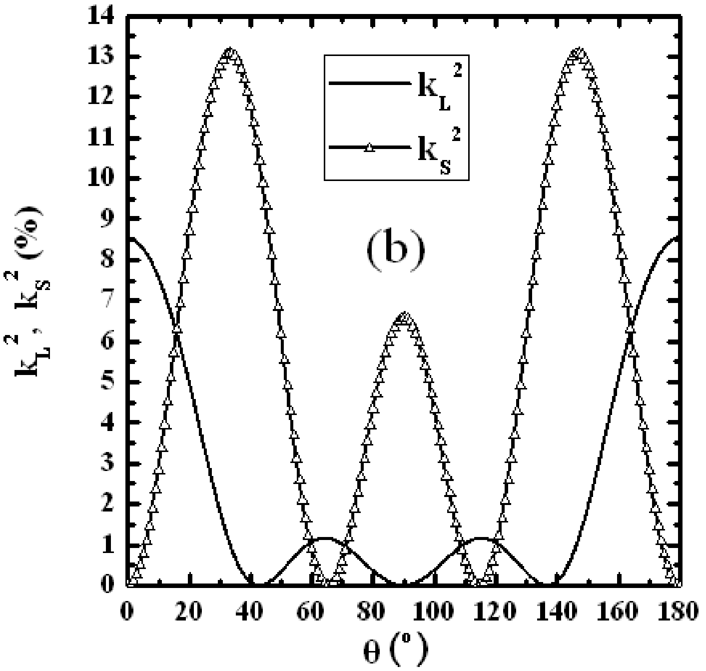

Figure 5.4. Bulk acoustic wave properties of ZnO. (a) acoustic velocity ; (b) electromechanical coupling coefficient

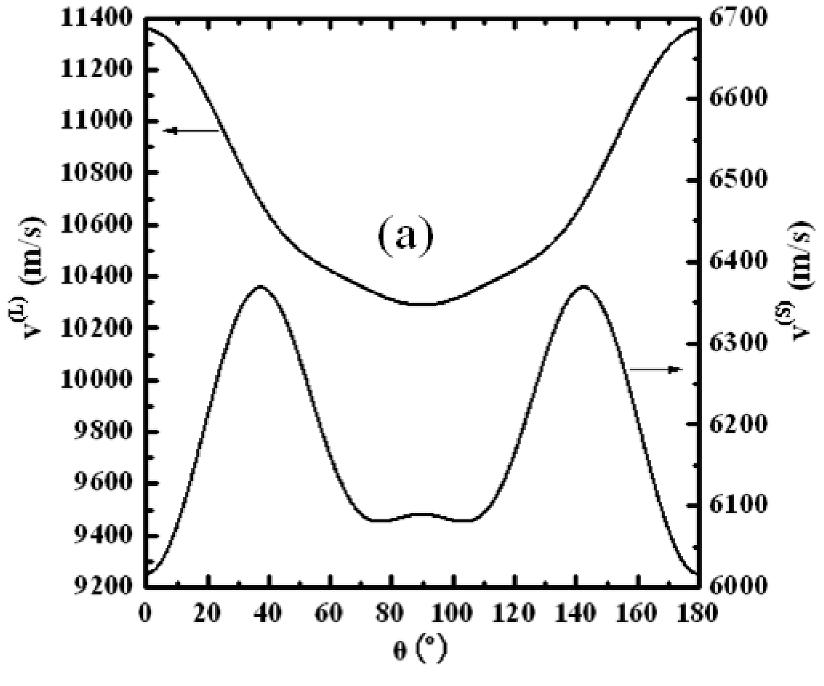

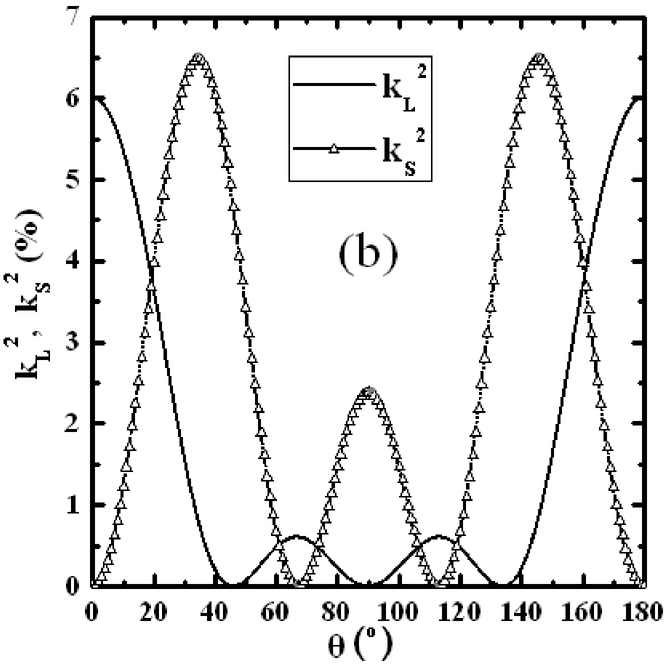

Figure 5.5. Bulk acoustic wave properties of AlN. (a) acoustic velocity ; (b) electromechanical coupling coefficient

It is necessary to know acoustic velocity and electromechanical coupling coefficient of ZnO and AlN films with different tilt angle, since they are two important bulk acoustic wave properties for FBAR design. Figure 5.4(a) and Figure 5.5(a) show the acoustic velocity of ZnO and AlN films for longitudinal and shear mode based on (5.24c) and (5.24d); Figure 5.4(b) and Figure 5.5(b) show electromechanical coupling coefficient of ZnO and AlN films for longitudinal and shear mode based on (5.32d) and (5.32e). The longitudinal and shear velocity of AlN are found in the range of 10287 m/s - 11354 m/s and 6016 m/s - 6368 m/s, respectively; and for ZnO the longitudinal and shear velocity are in the range of 5935 m/s - 6362 m/s and 2747 m/s - 3233 m/s, respectively. For most tilt angles the longitudinal electromechanical coefficient (k_L^2)of ZnO varying from 0% to 8.53% is higher than that of AlN varying from 0 to 6.0%, and the shear electromechanical coefficient (k_S^2) of ZnO varying from 0 to 13.1% is higher than that of AlN varying from 0 to 6.5%.

Table 5.2. Bulk acoustic wave properties of ZnO

Tilt angle (^{0})	Mode	Velocity (m/s)		Electromechanical couplingcoefficient (%)	
		v_L	v_S	$(k_L)^2$	$(k_S)^2$
0.0	Pure longitudinal	6362	2747	8.5	0
33.3	Quasi shear longitudinal	5992	3216	1.1	13.1(max)
43.0	Pure shear	5936	3213	0	10.4
65.4	Pure longitudinal	6028	2916	1.2	0
90.0	Pure shear	6070	2842	0	6.6

Table 5.3. Bulk acoustic wave properties of AlN

Tilt angle (^{0})	Mode	Velocity (m/s)		Electromechanical coupling coefficient (%)	
		v_L	v_S	$(k_L)^2$	$(k_S)^2$
0	Pure longitudinal	11354	6016	6.0	0
34.5	Quasi shear and longitudinal	10749	6363	0.8	6.5 (max)
46.1	Pure shear	10548	6325	0	4.6
67.1	Pure longitudinal	10380	6104	0.6	0
90	Pure shear	10287	6089	0	2.4

Based on the electric impedance expression (5.31), it can be found that the conditions for a single mode is $k_L = 0$ (for pure shear mode) or $k_S = 0$ (for pure longitudinal mode), which is corresponding to to $e_L = 0$ or $e_S = 0$ according to (5.32d) and (5.32e). The tilt angle for pure mode are numerically solved and summarized in Table 5.2 and 5.3, which also include the special tilt angle where the maximum shear electromechanical coupling coefficient occurs. For ZnO, the pure longitudinal mode is excited at $\theta = 0^0$ with $k_L^{\ 2} = 8.5\%$ and $\theta = 65.4^0$ with $k_L^{\ 2} = 1.2\%$; the pure shear mode is excited at $\theta = 43^0$ with $k_S^{\ 2} = 10.4\%$ and $\theta = 90^0$ with $k_S^{\ 2} = 6.6\%$; and the maximum of electromechanical coupling coefficient for shear mode is 13.1% at $\theta = 33.3^0$. For AlN, the pure longitudinal mode is excited at $\theta = 0$ with $k_L^{\ 2} = 6\%$ and $\theta = 67.1^0$ with $k_L^{\ 2} = 0.6\%$; the pure shear mode is excited at $\theta = 46.1^0$ with $k_S^{\ 2} = 4.6\%$ and $\theta = 90^0$ with $k_S^{\ 2} = 2.4\%$; and the maximum of electromechanical coupling coefficient for shear mode is 6.5% at $\theta = 34.5^0$.

The trends of modern mobile communication systems are increasing the need for filters with wider bandwidths, which requires higher electromechanical coupling coefficient of piezoelectric material for FBAR based filter. Hence, compared with the longitudinal electromechanical coupling coefficient ($k_L^{\ 2}$) up to 8.5% ($\theta = 0^0$) for ZnO and 6.0% ($\theta = 0^0$) for AlN, the higher value of shear electromechanical coupling coefficient ($k_S^{\ 2}$) up to 13.1% ($\theta = 33.3^0$) for ZnO and 6.5% ($\theta = 34.5^0$) for AlN provides a better choice for the design of higher bandwidth filter.

5.3.3 Simulation of electric impedance spectra of FBARs based on c-axis tilted ZnO and AlN films

It is well known that the mechanical quality factor (Q) of thin films vary with the thin film deposition processing conditions. The reported Q value of ZnO and AlN is around several hundreds [14, 17, 18, 20]. Here, for simplification, Q_L(mechanical quality factor of longitudinal mode) is assumed 350 for ZnO and 400 for AlN; Q_S (mechanical quality factor of shear mode) assumed 350 for ZnO and 400 for AlN. Thus, the new acoustic velocity v_L' (longitudinal mode) and v_S' (shear mode) are adopted for impedance calculation when Q_S and Q_L are taken into consideration [10]:

$$v_L' = v_L + j\frac{v_L}{2Q_L} \tag{5.33a}$$

$$v_S' = v_S + j\frac{v_S}{2Q_S} \tag{5.33b}$$

In addition, the thickness of ZnO or AlN films is assumed to be 2 μm and the electrode area is assumed to $9\times10^{-8}\,\mathrm{m}^2$. Due to the symmetry, tilt angle from 0 to 90 is adopted in the simulation. Figure 5.6 and 5.7 show the calculated impedance spectra of ZnO and AlN FBARs with different tilt angles, respectively, where the resonance frequencies of shear and longitudinal mode are fairly separated due to the difference of the acoustic velocities. For ZnO, the resonance frequencies of thickness longitudinal and shear modes are found in the range of 1.4 GHz to 1.6 GHz and 0.68 GHz to 0.81 GHz, respectively; the ratio of longitudinal and shear resonance frequency varies from 1.84 to 2.32. Link et al reported that the ratio of longitudinal and shear resonance frequency was around 2.0 for 18° c-axis inclined ZnO thin film [17], which is consistent with our theoretically calculated value 2.09 ($\theta = 18^0$). For AlN, the resonance frequencies of thickness longitudinal and shear modes are found in the range of 2.57 GHz to2.84 GHz and 1.50 GHz to 1.60 GHz respectively, and the ratio of longitudinal and shear resonance frequency varies from 1.66 to 1.89. For a specific tilt angle ($\theta = 28^0$) of AlN, the theoretical value are found to 1.726, which agrees well with 1.72 calculated through the experiment result of Wingqvist et al. [21]. For another tilt angle ($\theta = 30^0$) of AlN, the theoretical value are found to 1.713, which are also close to 1.76 calculated by the experiment result of Chuang et al. [86].

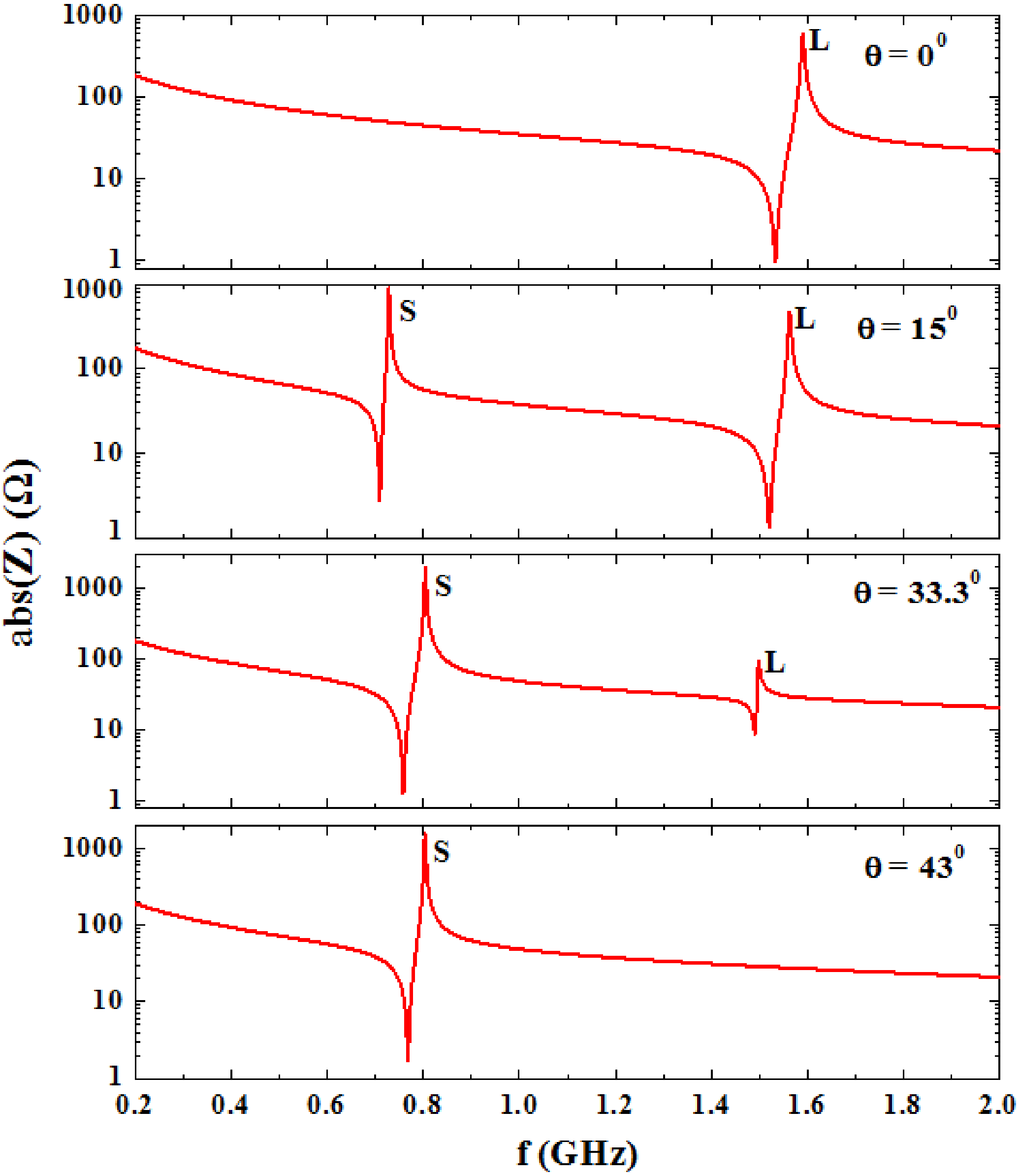

abs(Z) (Ω)
1000
100
10
1
θ = 0°
L
θ = 15°
S
L
θ = 33.3°
S
L
θ = 43°
S
0.2
0.4
0.6
0.8
1.0
1.2
1.4
1.6
1.8
2.0
f (GHz)

(a)

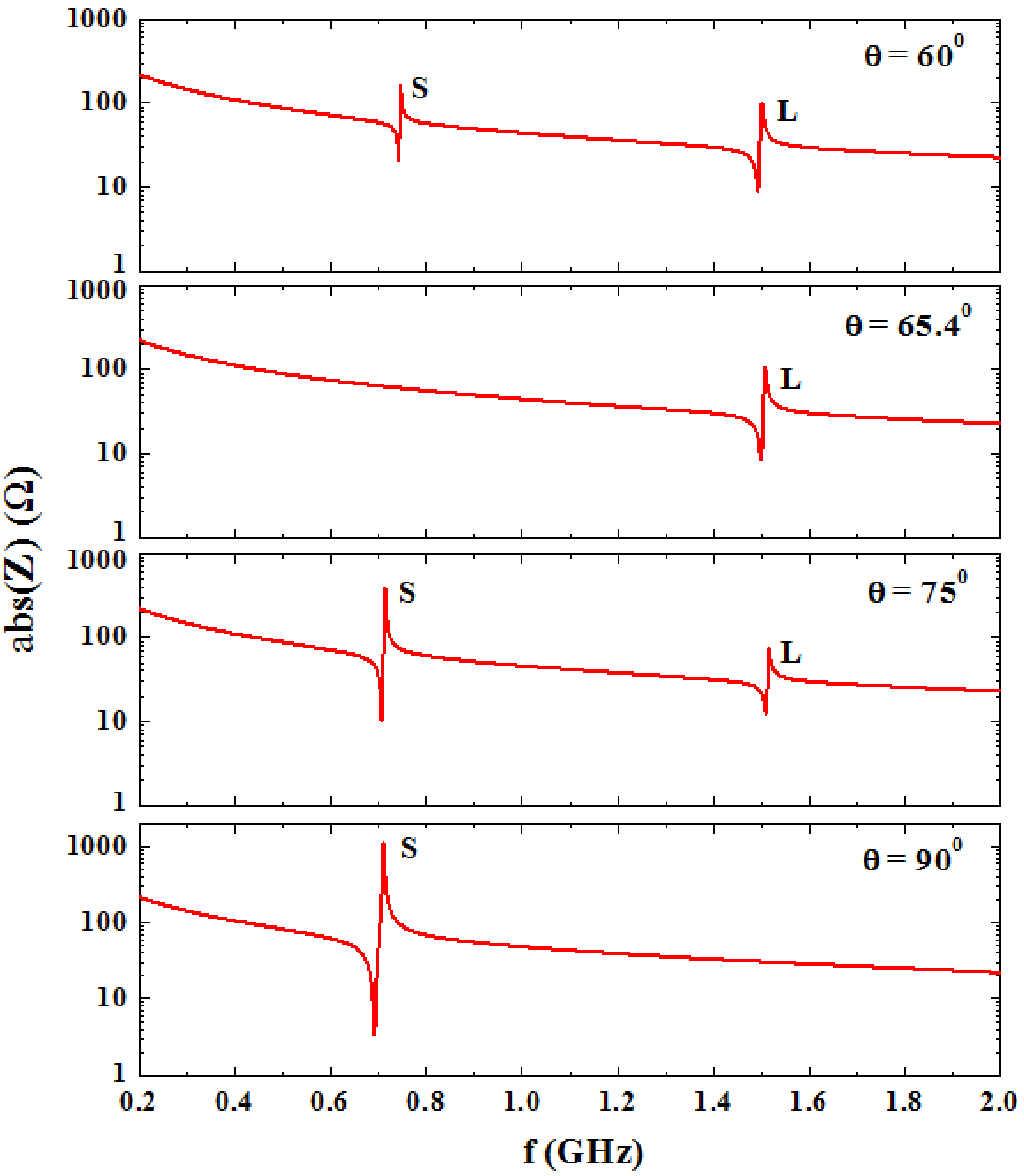

(b)

Figure 5.6. Impedance spectrum simulation of FBAR based on c-axis tilted ZnO film (S: Shear mode, L: Longitudinal Mode). (a) $\theta = 0^{0}, 15^{0}, 33.3^{0}, 43^{0}$; (b) $\theta = 60^{0}, 65.4^{0}, 75^{0}, 90^{0}$

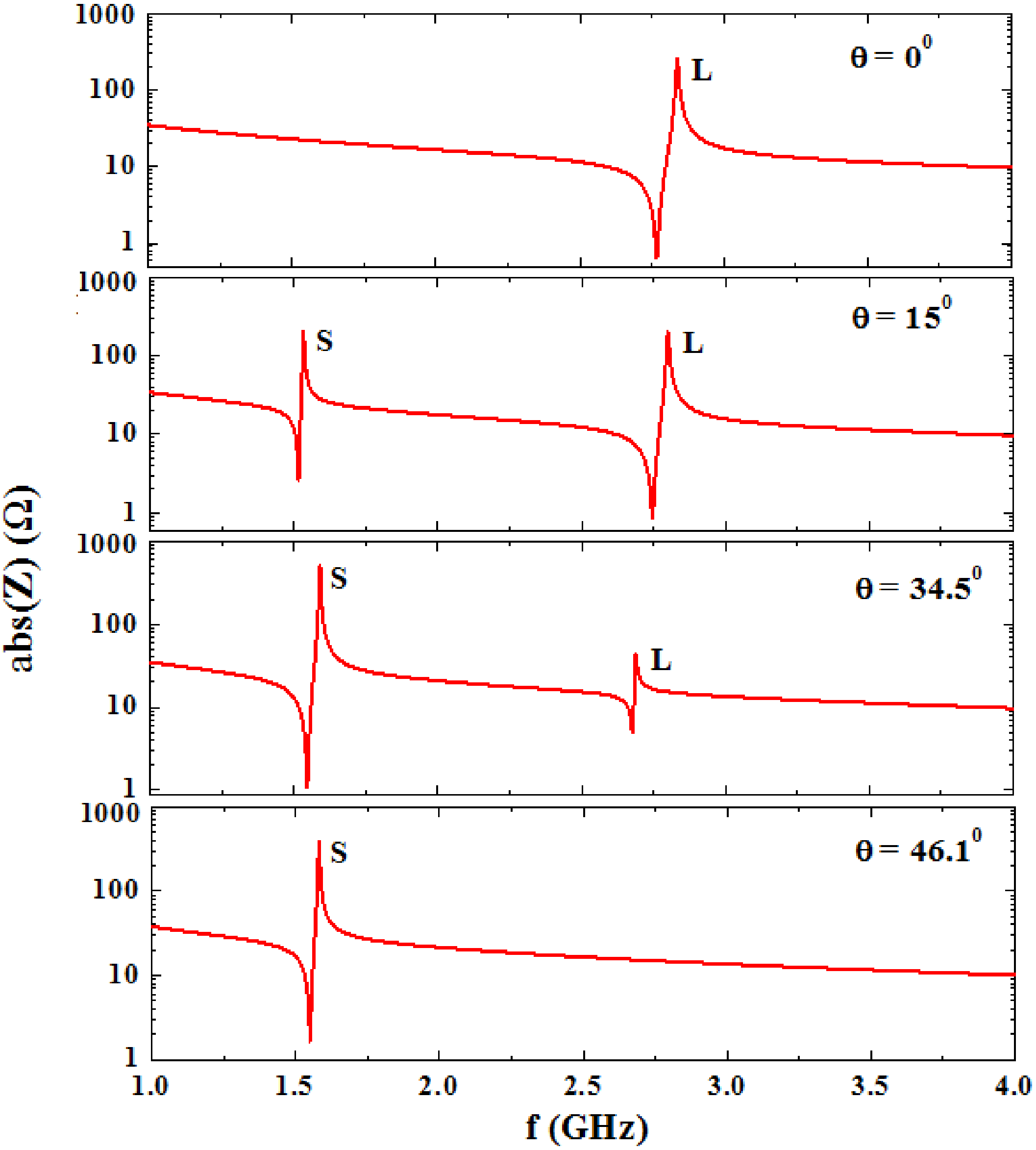
θ = 0⁰
L
θ = 15⁰
S
L
θ = 34.5⁰
S
L
θ = 46.1⁰
S
1000
100
10
1
abs(Z) (Ω)
1.0
1.5
2.0
2.5
3.0
3.5
4.0
f (GHz)

(a)

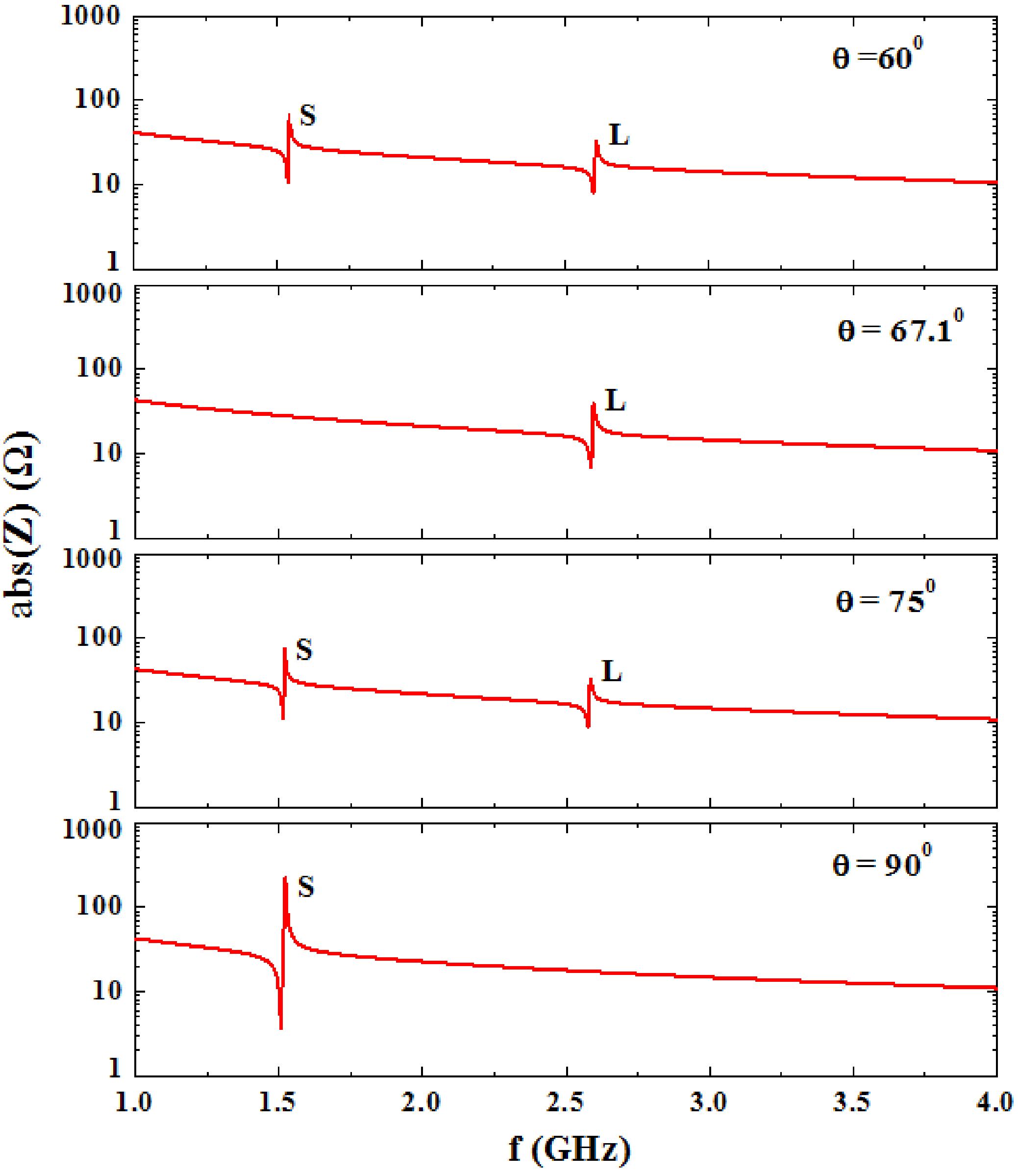

(b)

Figure 5.7. Impedance spectrum simulation of FBAR based on c-axis tilted AlN film (S: Shear mode, L: Longitudinal Mode). (a) $\theta = 0^0, 15^0, 34.5^0, 46.1^0$; (b) $\theta = 60^0, 67{,}1^0, 75^0, 90^0$

It also can be seen from Figure. 6 and 7 that resonance peaks of the spectra are different with the change of tilt angle. Interestingly, besides tilt angle 0^0 (i.e., normal polarization) a pure thickness longitudinal mode occurs at 65.4^0 for ZnO, and 67.1^0 for AlN, respectively, with smaller electromechanical coefficient. In addition, besides tilt angle 90^0 (i.e., in-plane polarization) a pure thickness shear mode occurs at 43^0 for ZnO, and 46.1^0 for AlN, respectively, with higher electromechanical coefficient. The strongest resonance peak of thickness shear mode for ZnO occurs at 33.3^0, where the maximum shear mode electromechanical coupling coefficient is found to be 13.1%. For AlN, the strongest resonance peak of thickness shear mode occurs at 34.5^0, where the maximum shear mode electromechanical coupling coefficient is found to be 6.5%. From Figure 5.4(b) and Figure 5.5(b), it can also be found that two peaks for $k_S{}^2$ exist at tilt angle $\theta = 33.3^0, 90^0$ for ZnO, and $\theta = 34.5^0, 90^0$ for AlN, respectively. It is noticed that low electromechanical coupling coefficient of shear mode will lead to deterioration of resonator operation in liquid [21]. Hence, tilt angle close to 33.3^0, 90^0 for ZnO films, and 34.5^0, 90^0 for AlN films are good options for sensor applications of FBARs in liquid environment. In fact, Wingqvist et al [21] presented AlN FBARs with a tilt angle around 30^0, which showed a strong shear resonance around 1.2 GHz with high Q_S around 150 in the water; and the viscous load experiments indicated the potential of FBARs for biosensor bioanalytical tools as well as for liquid sensing in general.

5.3.4 Sensitivity of ZnO and AlN FBAR for mass sensor application

Figure 5.8. The schematic of FBAR for mass sensor application

When bulk acoustic wave resonators are used for mass sensor application such as QCM, the resonant frequency will change due to surface mass change, and the absolute frequency is proportional to the square of the operating frequency. Hence, it is believed that sensor sensitivity will be greatly improved considering high operation frequency of FBARs. For analyzing sensor performance of FBAR, the impedance expression of FBAR with loading needs to be addressed. Usually the resonator is coated a sensitive layer (mass loading layer) for sensor application, as shown in Figure 5.8. Compared with mass loading layer, the acoustic impedance of electrodes is very small, for simplify the problem, we ignore the electrodes. For derivation of impedance expression, we still adopt equation (5.1)-(5.28), but the traction forces at the boundary ($x_3{}' = 0, h$) need change to:

$$T_5(0) = T_3(0) = 0 \tag{5.34a}$$

$$\begin{bmatrix} T_5(h) \\ T_3(h) \end{bmatrix} = \begin{bmatrix} -j\omega Z_{sl}^S & 0 \\ 0 & -j\omega Z_{sl}^L \end{bmatrix} \begin{bmatrix} u_1(h) \\ u_3(h) \end{bmatrix} \tag{5.34b}$$

Z_{sl}^L and Z_{sl}^S are the longitudinal and shear acoustic impedance of the sensitive layer (mass loading layer), which can be expressed by

$$Z_{sl}^L = j\rho_{sl} v_{sl}^L \tan(\gamma_{sl}^L) \tag{5.34c}$$

$$Z_{sl}^S = j\rho_{sl} v_{sl}^S \tan(\gamma_{sl}^S) \tag{5.34d}$$

$$v_{sl}^L = \sqrt{\frac{c_{sl}^{33}}{\rho_{sl}}}, v_{sl}^S = \sqrt{\frac{c_{sl}^{55}}{\rho_{sl}}}, \gamma_{sl}^L = \frac{\omega v_{sl}^L}{l_{sl}}, \gamma_{sl}^S = \frac{\omega v_{sl}^S}{l_{sl}} \tag{5.34e}$$

where v_{sl}^L and v_{sl}^S are longitudinal and shear acoustic velocity of sensitive layer; γ_{sl}^L and γ_{sl}^s are longitudinal and shear phase delay in mass loading layer; ρ_{sl} and l_{sl} are the density and thickness of mass loading layer; c_{sl}^{33} and c_{sl}^{55} are the elastic constants of mass loading layer.

According to the boundary condition (5.34) and equations (5.1)-(5.28), the impedance of coated FBAR can be solved:

$$Z = \frac{1}{j\omega C_0}\left(1-(k^L)^2 p^L \frac{\tan(\gamma_L/2)}{\gamma_L/2}-(k^S)^2 p^S \frac{\tan(\gamma_S/2)}{\gamma_S/2}\right) \tag{5.35a}$$

Where

$$C_0 = \frac{\varepsilon_{33}^{S'} A}{h} \tag{5.35b}$$

$$(k^L)^2 = \frac{(e_L)^2}{\varepsilon_{33}^{S'} \rho (v^{(L)})^2} \tag{5.35c}$$

$$(k^S)^2 = \frac{(e_S)^2}{\varepsilon_{33}^{S'} \rho (v^{(S)})^2} \tag{5.35d}$$

$$\gamma_L = \frac{\omega h}{v^{(L)}} \tag{5.35e}$$

$$\gamma_S = \frac{\omega h}{v^{(S)}} \tag{5.35f}$$

$$p^L = 1+\frac{\left[e_L \sin^2\left(\frac{\gamma^L}{2}\right)\left(\frac{Z_{sl}^L Z_{sl}^S}{Z_L Z_S}\cos(\gamma^s)+j\frac{Z_{sl}^{LL}}{Z_L}\sin(\gamma^S)\right)+je_S\sin^2\left(\frac{\gamma^S}{2}\right)\frac{Z_{sl}^{SL}}{Z_S}\sin(\gamma^L)\right]}{e_L\times\begin{pmatrix}\frac{Z_{sl}^L Z_{sl}^S}{Z_L Z_S}\cos(\gamma^L)\cos(\gamma^S)-\sin(\gamma^L)\sin(\gamma^S)+\\ j\left(\frac{Z_{sl}^{LL}}{Z_L}\cos(\gamma^L)\sin(\gamma^S)+\frac{Z_{sl}^{SS}}{Z_S}\sin(\gamma^L)\cos(\gamma^S)\right)\end{pmatrix}} \tag{5.35g}$$

$$p^S = 1+\frac{\left[e_S \sin^2\left(\frac{\gamma^S}{2}\right)\left(\frac{Z_{sl}^L Z_{sl}^S}{Z_L Z_S}\cos(\gamma^L)+j\frac{Z_{sl}^{SS}}{Z_S}\sin(\gamma^L)\right)+je_L\sin^2\left(\frac{\gamma^L}{2}\right)\frac{Z_{sl}^{SL}}{Z_L}\sin(\gamma^S)\right]}{e_S\times\begin{pmatrix}\frac{Z_{sl}^L Z_{sl}^S}{Z_L Z_S}\cos(\gamma^L)\cos(\gamma^S)-\sin(\gamma^L)\sin(\gamma^S)+\\ j\left(\frac{Z_{sl}^{LL}}{Z_L}\cos(\gamma^L)\sin(\gamma^S)+\frac{Z_{sl}^{SS}}{Z_S}\sin(\gamma^L)\cos(\gamma^S)\right)\end{pmatrix}} \tag{5.35h}$$

$$Z_{sl}^{LL} = Z_{sl}^L \cos^2(\alpha)+Z_{sl}^S \sin^2(\alpha) \tag{5.35i}$$

$$Z_{sl}^{SS} = Z_{sl}^{S}\cos^2(\alpha) + Z_{sl}^{L}\sin^2(\alpha) \tag{5.35j}$$

$$Z_{sl}^{SL} = (Z_{sl}^{S} - Z_{sl}^{L})\sin(\alpha)\cos(\alpha) \tag{5.35k}$$

Through analyzing (5.35), the condition for pure longitudinal mode is $\alpha = 0, e_S = 0$, which is equivalent to $c_{35}^{E'} = 0, e_{35}^{'} = 0$; the condition for pure shear mode is $\alpha = 0, e_L = 0$, which is equivalent to $c_{35}^{E'} = 0, e_{33}^{'} = 0$. Hence, from Figure 5.2 and 5.3, we can conclude that the pure longitudinal mode for ZnO and AlN is excited at $\theta = 0^0$, and for pure shear mode it is $\theta = 90^0$.In addition, α is small due to the small value of $c_{35}^{E'}$, then longitudinal mode is predominant when $e_S = 0$ and shear mode is predominant when $e_L = 0$, therefore, at $\theta = 65.4^0$ for ZnO and $\theta = 67.1^0$ for AlN, it can be approximate to pure longitudinal mode; at $\theta = 43^0$ for ZnO and $\theta = 46.1^0$ for AlN, it can be approximate to pure shear mode.

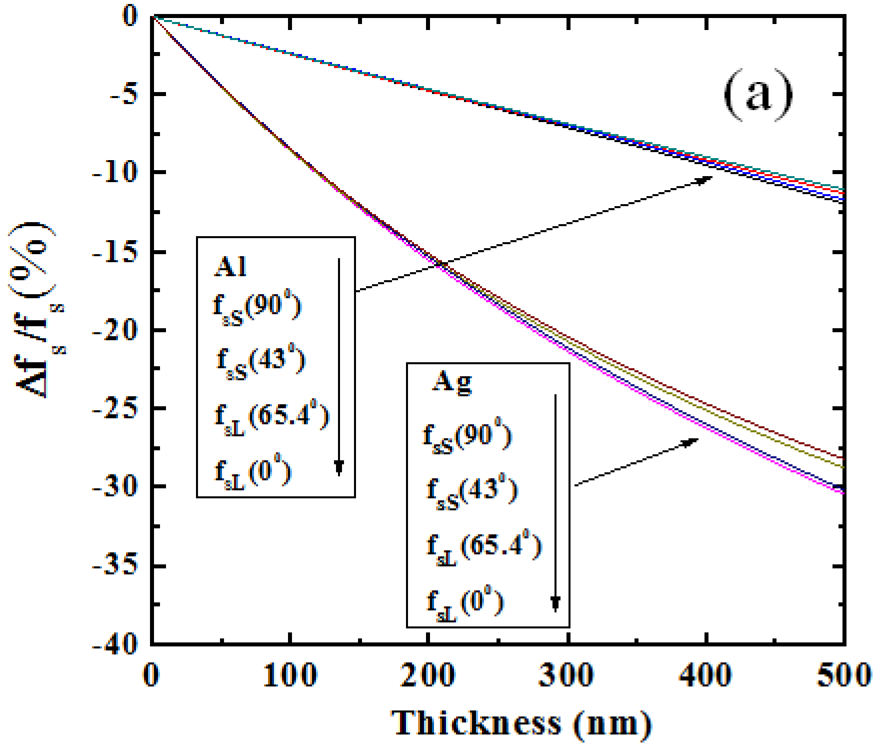

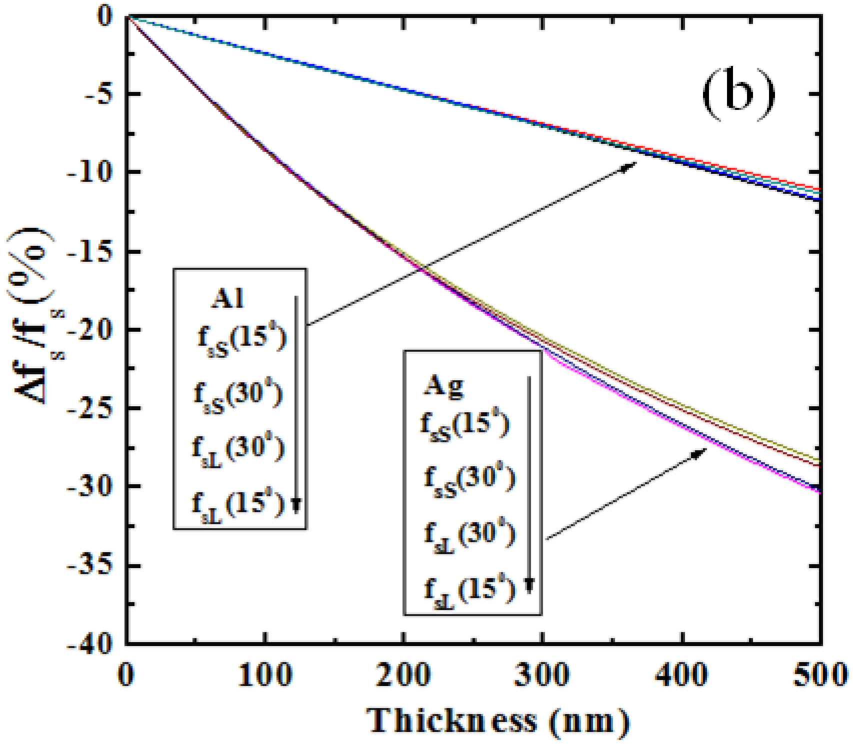

Figure 5.9. Resonant frequency shift of FBAR based on c-axis tilted ZnO film vs thickness of mass loading.

(a) $\theta = 0^0, 43^0, 65.4^0, 90^0$; (b) $\theta = 15^0, 30^0$

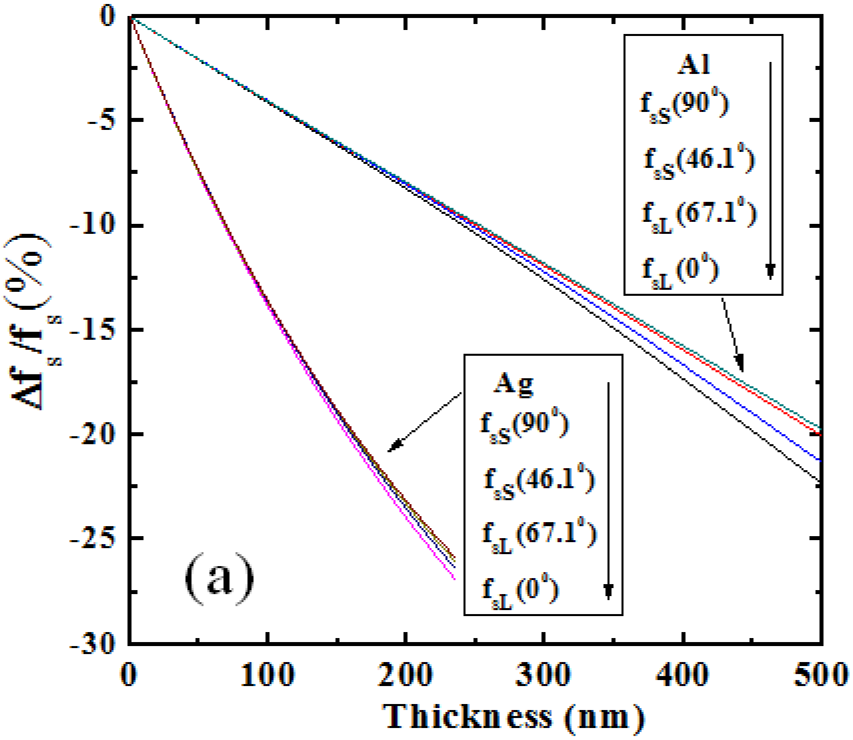

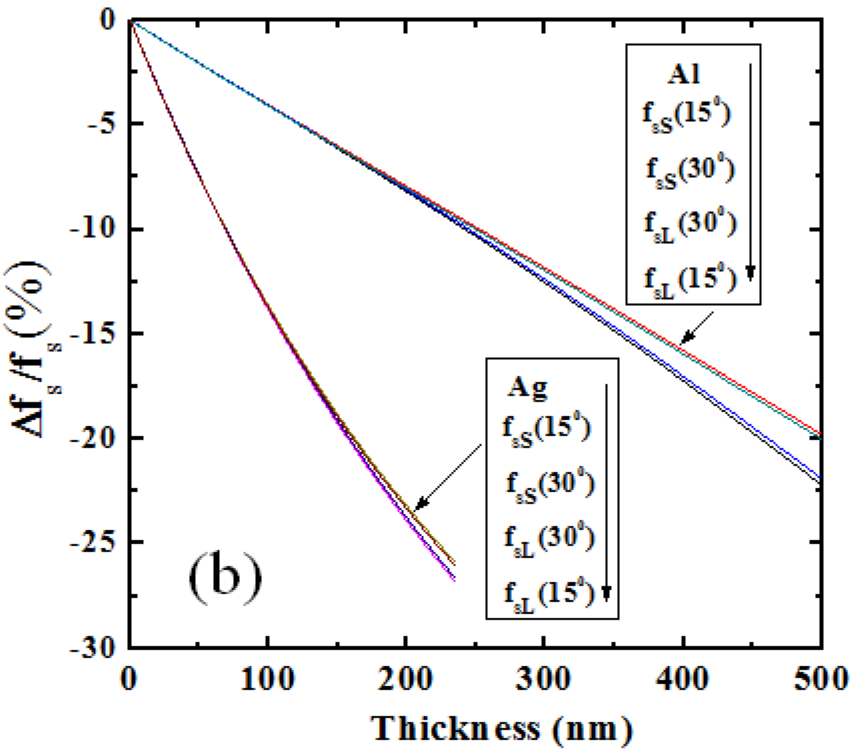

Figure 5.10. Resonant frequency shift of FBAR based on c-axis tilted AlN film vs thickness of mass loading. (a) $\theta = 0^0, 46.1^0, 67.1^0, 90^0$; (b) $\theta = 15^0, 30^0$

Table 5.4. Parameters for calculation of $f_{sL}(\theta)$ and $f_{sS}(\theta)$.

Mass loading layer	Density (kg/m^3)	Thickness (nm)	Young's modulus (GPa)	Poisson's ratio	Q_L	Q_S
Al	2700	0-500	70	0.35	1000	1000
Ag	10490	0-500	83	0.37	1000	1000

To have an overall understanding of dual mode FBAR as mass sensor, we gradually increase the mass loading and investigate the change of the resonant frequency f_s, which is corresponding to maximum conductance and usually adopted for sensor output. Here, $f_{sL}(\theta)$ and $f_{sS}(\theta)$ are used to express the longitudinal and shear resonant frequency of FBAR based on AlN or ZnO with c-axis tilt angle θ. Figure 5.9 and 5.10 shows the change of $f_{sL}(\theta)$ and $f_{sS}(\theta)$ with the thickness of mass loading layer for some specific tilt angles. In the simulation, Al and Ag are the materials for mass loading layer, and Table 5.4 lists their parameters for calculation of $f_{sL}(\theta)$ and $f_{sS}(\theta)$ using (5.35). As shown in Figure 5.9 and 5.10, for mass loading Al and Ag, both $f_{sL}(\theta)$ and $f_{sS}(\theta)$ linearly decrease when the thickness of mass loading layer is small. For the same thickness of mass loading, the resonant frequency shift for Ag is higher than Al, because Ag has higher density than Al, inducing higher acoustic loading.

Table 5.5. Mass sensitivity of FBAR based on c-axis tilted ZnO.

tilt angle (^{0})	$f_{sL}(\theta)$ (GHz)	$f_{sS}(\theta)$ (GHz)	$S_L(\theta)$ (cm^2/g)		$S_S(\theta)$ (cm^2/g)	
			Al	Ag	Al	Ag
0	1.533439408	____	-904	-904	____	____
15	1.520757366	0.709173538	-896	- 894	-896	-896
30	1.496097496	0.751143640	-882	-879	-926	-919
43	____	0.767714844	____	____	-911	-909
65.4	1.499892844	____	-881	-877	____	____
90	____	0.690955092	____	____	-896	-896

Table 5.6. Mass sensitivity of FBAR based on c-axis tilted AlN

tilt angle (^{0})	$f_{sL}(\theta)$ (GHz)	$f_{sS}(\theta)$ (GHz)	$S_L(\theta)$ (cm^2/g)		$S_S(\theta)$ (cm^2/g)	
			Al	Ag	Al	Ag
0	2.767650148	____	-1570	-1558	____	____
15	2.746620142	1.517122380	-1556	-1548	-1548	-1539
30	2.695601826	1.541801144	-1541	-1531	-1570	-1560
46.1	____	1.550894306	____	____	-1563	-1548
67.1	2.588555566	____	-1548	-1525	____	____
90	____	1.507487836	____	____	-1548	-1535

The mass sensitivity of dual mode FBARs is defined as below:

$$S_L(\theta) = \frac{\Delta f_{sL}(\theta) / f_{sL}(\theta)}{\Delta m} \tag{5.36a}$$

$$S_S(\theta) = \frac{\Delta f_{sS}(\theta) / f_{sS}(\theta)}{\Delta m} \tag{5.36b}$$

$$\Delta m = \rho_m t_m \tag{5.36c}$$

where $S_L(\theta)$ is the mass sensitivity of longitudinal mode for FBAR based on AlN or ZnO with c-axis tilt angle θ, and $S_S(\theta)$ is the mass sensitivity of shear mode; $\Delta f_{sL}(\theta)$ and $\Delta f_{sS}(\theta)$ are resonant frequency shift due to mass loading Δm; ρ_m and t_m are the density and thickness of mass loading layer. The mass sensitivity of FBARs in a linear range ($\Delta f_s(\theta) / f_s(\theta) \leq 5\%$) is evaluated through measuring resonant frequency shift for 5nm Al or Ag mass loading. And the calculated mass sensitivity for some special angles according to (5.36), is listed in Table 5.5 and 5.6. It can be seen from Table 5.5 and 5.6 that $S_L(\theta)$ and $S_S(\theta)$ of ZnO are around -900(cm^2/g), and $S_L(\theta)$ and $S_S(\theta)$ o f AlN are around -1550(cm^2/g), which is greatly higher than -14(cm^2/g), the mass sensitivity of a 6M QCM [93]. Due to the small value of α or $c_{35}^{E'}$ for all θ, the coupling between longitudinal and shear mode is weak, so the resonator can be approximate to a simple combination of two single mode. On the other hand, we know the mass sensitivity (S_m) of single mode resonator is only dependant on the density (ρ_p) and thickness (d_p) of the piezo layer [93].

$$S_m = \frac{-1}{\rho_p d_p} \tag{5.37}$$

Hence, for ZnO or AlN FBAR, $S_L(\theta)$ and $S_S(\theta)$ have close value, and do not change much with tilt angel, which also can be seen in Table 5.5 and 5.6.

It should be pointed out that in (5.35) the mass loading layer is assumed isotropic. When the mass loading layer is replaced with electrode material, (5.35) can be used to analyze the effect of electrode, which actually has been shown in mass sensitivity calculation. Moreover, through replacing the acoustic impedance of sensitive layer with acoustic impedance of multilayer, (5.35) can be used for analysis of multilayer loading, so long as the multilayer is isotropic and non-piezo.

5.4 CONCLUSION

FBARs based on ZnO and AlN films have been theoretically studied. Due to the crystal orientation dependence of material properties including elastic constants, piezoelectric constants and dielectric constants, the acoustic velocity, electromechanical coefficient and impedance of

FBARs also depend on the crystal orientation. The equation for predicting impedance of FBAR has been derived through the basic piezoelectric equations, which shows the coexistence of longitudinal and shear mode when c-axis tilt angle changes. The simulation results show that the pure longitudinal mode occurs at 0^0 and 65.4^0, and the pure shear mode occurs at 43^0 and 90^0 for ZnO; the pure longitudinal mode occurs at 0^0 and 67.1^0, and the pure shear mode occurs at 46.1^0 and 90^0 for AlN. Two peaks of shear electromechanical coefficient are found at $\theta = 33.3^0, 90^0$ for ZnO and $\theta = 34.5^0, 90^0$ for AlN. ZnO and AlN films with tilt angle around these two peaks are good options for FBAR application in liquid, considering their strong shear resonance with high electromechanical coefficients. Compared with QCM, the mass sensitivity of FBAR based ZnO and AlN are pretty high, which shows good promising in mass sensor application.

6.0 CONCLUSIONS AND FUTURE WORK

6.1 MAJOR ACCOMPLISHMENTS

The research in this dissertation is focused on experimental investigation and modeling of bulk acoustic wave resonator sensor. The following is a summary of our major accomplishments.

(1) Apply Quartz TSM resonator for extracting viscoelastic properties of polymer nanocomposite thin films deposited on the resonators surface.

- The input electric impedance/admittance of multilayer loaded Quartz TSM acoustic wave resonator was derived using transfer matrix method, which reveals the relation between the viscosity of coating layer and the electrical impedance/admittance of coated quartz TSM resonator. Based on this relation, we characterized viscoelastic properties of PVDF-TrFE/CNT nanocomposite thin films using Quartz TSM resonator.
- The complex shear modulus of PVDF-TrFE/MWCNT composite thin films has been extracted through fitting the theoretical curves to the experimental admittance spectra of naonocomposite coated quartz TSM resonaotrs. It has been found that the storage modulus of the nanocomposites decreases slightly with the carbon nanotube concentration, while no significant variation is found for the loss modulus.

(2) Investigate Quartz TSM resonator to monitor flow rate in liquid.

- A special flow chamber was fabricated to assist Quartz TSM resonator for flow measurement. The parallel plate flow region of the flow chamber was designed to make liquid pressure linear with flow rate, so that resonance frequency shift of resonator due to pressure has a well-defined relation with flow rate.
- A theoretical model of clamped Quartz TSM resonator to predict the resonant frequency shift due to normal pressure has been developed, which agrees well the experiment results.
- Experimental study of Quartz TSM resonator for flow measurement has been performed, which shows a quadratic relation between the frequency shift and volumetric flow rate. Compared with the conventional expensive and complex flow-sensing devices, our acoustic wave flow sensor provides an alternative method for flow-rate monitoring with substantially concise structure, low cost and high operation convenience.
- A dual resonator configuration was proposed for practical application, which works as differential pressure flowmeters for the separation of the flow pressure from the outlet pressure.

(3) Theoretically analyze FBARs based on c-axis tilted ZnO and AlN

- The analytical study of FBARs using ZnO and AlN films with a c-axis tilt angle (off-normal) from 0^0 to 180^0 has been performed. It was found that the tilted c-axis orientation induces normal plane and in-plane polarizations, which leads to the coexistence of the longitudinal mode and shear mode in the resonator.
- The equation for predicting electric impedance of FBARs was derived from the basic piezoelectric constitutive equations. Material properties including elastic, dielectric and piezoelectric coefficients, bulk wave properties including acoustic velocity and

electromechanical coupling coefficient, and impedance of FBARs were calculated and showed strong dependence on the tilt angle.

- It was found that for ZnO FBAR, pure thickness longitudinal modes occur at 0^0 and 65.4^0, and pure thickness shear modes occur at 43^0 and 90^0. For AlN FBAR, pure longitudinal modes occur at 0^0 and 67.1^0, and pure shear modes occur at 46.1^0 and 90^0.The electromechanical coupling coefficient of shear mode has a maximum value 13.1% at $\theta=33.3^0$ for ZnO, and 6.5% at $\theta=34.5^0$ for AlN; the maximum electromechanical coupling coefficient of longitudinal mode occurs at $\theta=0^0$ with a value of 8.5% for ZnO, and 6% for AlN. The appearance of strong shear resonance makes ZnO or AlN FBARs possible for sensor application in liquid; the higher electromechanical coupling coefficient of shear mode provides more options for filter design; the simulation results showed that the mass sensitivity of FBAR based ZnO and AlN are pretty high compared with QCM, which shows good promising in mass sensor application.

6.2 FUTURE WORK

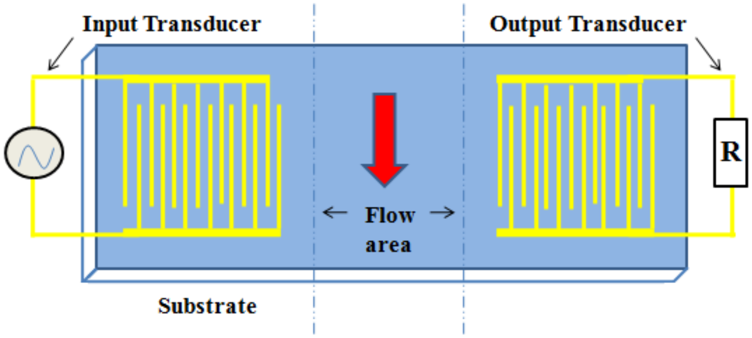

Figure 6.1. Schematic of a flow sensor based on SAW device

It has been shown that the Quartz bulk acoustic wave resonator can be used to monitor flow rate with high simplicity. However, the sensitivity of the TSM quartz acoustic wave flow sensor seems not high. On the other hand, SAW device usually has higher sensitivity for sensor application compared with BAW device. Hence, I propose to develop a flow sensor based on SAW device, as shown in Figure 6.1. The SAW device has a two-port structure: two IDTs are deposited on the piezo substrate as input and output transducer. When an AC voltage is applied on input transducer, a periodic electric field is imposed on the piezoelectric substrate. Due to the piezoelectricity, a periodic strain field is created in the substrate, which produces a standing surface acoustic wave. This acoustic wave is parallel to the surface and propagates in both directions away from the input transducer. When the wave is incident on output transducer, a potential is produced due to the piezoelectricity and a current is induced; the current can be optimized when the frequency of input signal equals to resonant frequency, which is determined by the geometry of transducers and the piezoelectric constants of substrate. For flow measurement, the central of SAW device exposed to fluid is on the way of acoustic wave propagation. When there is flow passing, due to flow pressure, the center of SAW will be deformed, and the induced strain changes the acoustic wave path. As a result, the electric properties of SAW device changes with the flow rate. For example, we may get the information of flow rate through measurement of acoustic transfer time between input and output transducer, since the distance between these two transducers change with flow rate. In addition, to prevent the liquid from affecting the IDTs, it is better to deposit the IDTs on the backside of substrate, which also simplify the connection for device measurement.

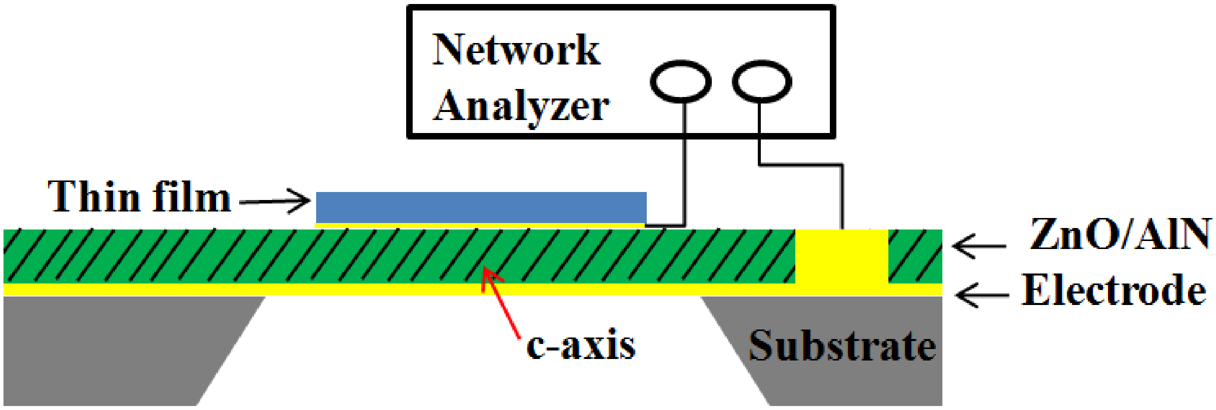

Figure 6.2. Schematic of ZnO/AlN FBAR for thin film characterization

It also has been demonstrated that TSM resonator can be used to extract complex shear modulus of thin films; similarly the longitudinal mode resonator could be able to extract the corresponding elastic constants. On the other hand, our theoretical analysis has shown that ZnO or AlN resonator can excite longitudinal and shear mode at same time when c-axis of ZnO or AlN is tilted. Therefore, it is anticipated that using dual mode resonator can provide more mechanical properties of thin film compared with single mode resonator. In the future, we can investigate ZnO/AlN dual mode resonator for thin film characterization through the admittance/ impedance measurement, as shown in Figure 6.2.

BIBLIOGRAPHY

1. ANSI/IEEE Std. 176-1987, IEEE Standard on Piezoelectricity, The Institute of Electrical and Electronics Engineers, Inc, 1988, New York, NY, USA.

2. D. S. Ballantine, R. M. White, S. J. Martin, A. J. Ricco, G. C. Frye, E. T. Zellars, H. Wohltjen, Acoustic wave sensors: theory, design, and physico-chemical applications, San Diego , Academic Press, c1997

3. Janshoff, A. and C. Steinem. Quartz crystal microbalance for bioanalyticalapplications, Sensors Update, vol.9, pp.313-354, 2001.

4. Stephen J. Martin, Victoria Edwards Granstaff and Gregory C. Frye, Characterization of a quartz crystal microbalance with simultaneous mass and liquid loading, Anal. Chem., vol. 63, pp. 2272-2281, 1991.

5. G. Sauerbrey, Verwendung con Schwingquarzen zur Wagung dunner Schichten und zur Mikrowagung, Zeitschrift fur Physik, vol. 155, pp. 206-222, 1959.

6. Ralf Lucklum and Peter Hauptmann, Transduction mechanism of acoustic-wave based chemical and biochemical sensors, Meas. Sci. Technol., vol. 14, pp. 1854-1864, 2003.

7. Krimholtz, R., Leedom, D.A. and Matthaei, G.L., New equivalent circuits for elementary piezoelectric transducers, Electronics Letters, vol. 6, pp. 398-399, 1970.

8. K. M. Lakin and J. S. Wang, Acoustic bulk wave composite resonators, Appl. Phys. Lett., vol. 38, pp.125-127, 1981.

9. R. Aigner, Volume manufacturing of BAW-filters in a CMOS fab, Proceedings of the 2nd International Symposium on Acoustic Devices for Future Communication Systems, Chiba University, Japan, Mar. 3-5, pp. 129-134, 2004.

10. Qingming Chen and Qing-Ming Wang, The effective electromechanical coupling coefficient of piezoelectric thin-film resonators, Appl. Phys. Lett., vol. 86, pp. 022904-022904-3, 2005.

11. A. Müller, D. Neculoiu, G. Konstantinidis, A. Stavrinidis, D. Vasilache, A. Cismaru, M. Danila, M. Dragoman, G. Deligeorgis, and K. Tsagaraki, 6.3-GHz Film Bulk Acoustic

Resonator Structures Based on a Gallium Nitride/Silicon Thin Membrane, IEEE Electron Device Letters, vol. 30, pp. 799-801, 2009.

12. Qingming Chen, Fabrication and Characterization of AlN Thin Film Bulk Acoustic wave Resonator, Ph. D. thesis (Mechanical Engineering, University of Pittsburgh, 2006).

13. R. Gabl, H. -D. Feucht, H. Zeininger, G. Eckstein, M. Schreiter, R. Primig, D. Pitzer, and W. Wersing, First results on label-free detection of DNA and protein molecules using a novel integrated sensor technology based on gravimetric detection principles, Biosensors and Bioelectronics, vol. 19, pp. 615-620, 2004.

14. H. Zhang, M. S Marma, E. S. Kim, C. E McKenna, and M. E Thompson, A film bulk acoustic resonator in liquid environments, J. Micromech. Microeng., vol. 15, pp. 1911–1916, 2005.

15. M. Benetti, D. Cannatà, and F. Di Pietrantonio, Microbalance chemical sensor based on thin-film bulk acoustic wave resonators, Appl. Phys. Lett., vol. 87, pp. 173504-17350-3, 2005.

16. N. F. Foster, G. A. Coquin, G. A. Rozgonyi, F.A.Vannatta, Cadmium Sulphide and Zinc Oxide Thin-Film Transducers, IEEE Transactions on Sonics and Ultrasonics, vol. 15, pp. 28-40, 1968.

17. M. Link, M. Schreiter, J. Weber, R. Primig, D. Pitzer, and R. Gabl, Solidly mounted ZnO Shear Mode Film Bulk Acoustic Resonators for Sensing Applications in Liquids, IEEE Trans. Ultrason., Ferroelect., Freq. Contr., vol. 53, pp. 492-496, 2006

18. J. Bjurström, D. Rosén, I. Katardjiev, V. M. Yanchev, and I. Petrov, Dependence of the Electromechanical Coupling on the Degree of Orientation of c-Textured Thin AlN Films, IEEE Trans. Ultrason., Ferroelect., Freq. Contr., vol. 51, pp. 1347-1353, 2004.

19. G. Wingqvist, J. Bjurström, L. Liljeholm, I. Katardjiev, and A. L. SpetZ, Shear mode AlN thin film electroacoustic resonator for biosensor applications, IEEE Sensor Proceedings, pp. 492-495, 2005.

20. J. Bjurström, G. Wingqvist, and I. Katardjiev, Synthesis of Textured Thin Piezoelectric AlN Films With a Nonzero C-Axis Mean Tilt for the Fabrication of Shear Mode Resonators, IEEE Trans. Ultrason., Ferroelect., Freq. Contr., vol. 53, pp. 2095-2100, 2006.

21. G. Wingqvist, J. Bjurström, L. Liljeholm, V. Yantchev, and I. Katardjiev, Shear mode AlN thin film electro-acoustic resonant sensor operation in viscous media, Sensors and Actuator B, vol. 123, pp. 466-473, 2007.

22. S. M. Spearing, Materials Issues in Microelectromechanical Systems, Acta Mater., vol. 48, pp. 179-196, 2000.

23. M.A. Haque and M.T.A. Saif, A Novel Technique for Tensile Testing of Submicron Scale Freestanding Specimens in SEM and TEM, Experimental Mechanics, vol. 42, pp. 123-130, 2002.

24. R. D. Emery and G .L. Povirk, Tensile behavior of free-standing gold films, Acta Mater. vol. 51, pp. 2067-2087, 2003

25. H. D. Espinosa, B. C.Prorok and M. Fischer, A methodology for determining mechanical properties of freestanding thin films and MEMS materials, J. Mech. Phys. Solids, vol. 51, pp. 47-67, 2003.

26. D. S. Gianola and W. N. Sharpe, Techniques for testing thin films in tension, Experimental Techniques, vol. 28, pp. 23-27, 2004.

27. R. Lucklumy, C. Behlingy, P. Hauptmann, Role of mass accumulation and viscoelastic film properties for the response of acoustic-wave-based chemical sensors, Anal. Chem. vol. 71, pp. 2488-2496, 1999.

28. R. Lucklumy, C. Behlingy, R. W. Cernosekz and S. J. Martin, Determination of complex shear modulus with thickness shear mode resonators, J. Phys. D: Appl. Phys., vol. 30, pp. 346–356, 1997.

29. Kino, G.S.,. Acoustic Waves: Devices, Imaging and Analog Signal Processing. Prentice-Hall Englewood Cliffs, NJ, 1987

30. B. Morray, S. Li, J. Hossenlopp, R. W. Cernosek, and F. Josse, PMMA polymer characterization using thickness-shear mode (TSM) quartz resonator, Proc. IEEE Freq. Cont. Symp and PDA Exhibition., pp. 294-300, 2002.

31. L. Jiang, J. Hossenlopp, R. Cernosek, and F. Josse , Characterization of Epoxy Resin SU-8 Film Using Thickness-Shear Mode (TSM) Resonator, Proc. IEEE Freq. Cont. Symp and PDA Exhibition Jointly with the 17th European Frequency and Time Forum., pp. 986-992, 2003.

32. H. Nowotny and E. Benes, General one-dimensional treatment of the layered piezoelectric resonator with two electrodes, J. Acoust. Soc. Am., vol. 82, pp. 513–521, 1987.

33. R. W. Cernosek, S. J. Martin, A. R. Hillman, and H. L. Bandey, Comparison of Lumped-Element and Transmission-Line Models for Thickness-Shear-Mode Quartz Resonator Sensors, IEEE Transactions on Ultrasonics, Ferroelectrics, and Frequency Control, 45(1998), pp. 1399-1407.

34. H. Ohigashi, Electromechanical properties of polarized polyvinylidene fluoride films as studied by the piezoelectric resonance method, Journal of Applied Physics, vol.47, pp. 949-955, 1976.

35. A. L. Robinson, Flexible PVF2 film: An exceptional polymer or transducers, Sczence, vol. 200, pp. 1371-1374, 1978.

36. P. Benech, E. Chambered, C. Monllor, Acceleration measurement using PVDF, IEEE Transactions on Ultrasonics, Ferroelectrics, and Frequency Control, vol.43, pp. 838-843, 1996.

37. K. Liao and S. Li, Interfacial characteristics of a carbon nanotube–polystyrene composite system, Applied Physics Letters, vol. 79, pp. 4225-4227, 2001.

38. M. Cadek, Morphological and mechanical properties of carbon-nanotube-reinforced semicrystalline and amorphous polymer composites, Applied Physics Letter, vol. 81, pp. 5123-5125, 2002.

39. X. Xu, M. M. Thwe, C. Shearwood, and K. Liao., Mechanical properties and interfacial characteristics of carbon-nanotube-reinforced epoxy thin films, Applied Physics Letters, vol. 81, pp. 2833-2835, 2002.

40. D. Qian, G. J. Wagner, W. K. Liu, M.-F. Yu and R. S. Ruoff, Mechanics of carbon nanotubes, Applied Mechanics Reviews, vol. 55, pp. 499-533, 2002.

41. Y. Jim´enez, R. Fern´andez, R. Torres, and A. Arnau, A Contribution To Solve the Problem of Coating Properties Extraction in Quartz Crystal Microbalance Applications, IEEE Transactions on Ultrasonics, Ferroelectrics, and Frequency Control, vol. 53, pp. 1057-1072, 2006.

42. L. Qin, H. Cheng and Q.-M. Wang, Characterization of Polymer Nanocomposite ThinFilms Using Quartz Resonator Sensor, IEEE Frequency Control Symposium, Miami, FL, USA , 2006.

43. F. T. Fisher, R. D. Bradshaw, and L. C. Brinson, Fiber waviness in nanotube-reinforced polymer composites: I. Modulus predictions using effective nanotube properties, Composites Science and Technology, vol. 63, pp. 1689-1703, 2003.

44. Fisher, F. T., R. D. Bradshaw, L. C. Brinson , Effects of nanotube waviness on the modulus of nanotube-reinforced polymers, Applied Physics Letters, vol. 80, pp. 4647-4649, 2002.

45 R. W. Miller, Flow Measurement Engineering Handbook, 2nd ed., McGraw-Hill, New York, 1989.

46 L. C. Lynnworth, Ultrasonic Measurements for Process Control, Academic Press, New York, 1989.

47 K. Shirai, T. Pfister, L. Büttner, J. Czarske, H. Müller, S. Becker, H. Lienhart and F. Durst, Highly spatially resolved velocity measurements of a turbulent channel flow by a fiber-optic heterodyne laser-Doppler velocity-profile sensor, Experiments in Fluids, vol.40, pp.473-481, 2006.

48 C. G. Lomas, Fundamentals of Hot Wire Anemometry. Cambridge Univ. Press, New York, 1986.

49 S. G. Joshi, Surface-Acoustic-Wave (SAW) Flow Sensor, IEEE Transactions on Ultrasonics, Ferroelectrics, and Frequency Control, Vol.38, pp.148-154, 1991.

50 D. Rebièrea, C. Déjousa, J. Pistréa, J.-L. Aucouturiera, C. Tiretb and R. Planadeb, Acoustic wave devices to measure gas flow: Comparison between surface acoustic wave (SAW) and shear horizontal acoustic plate mode (SH-APM) oscillators, Sensors and Actuators A, vol. 42, pp.384-388, 1994.

51 D. A. Buttry and M. D. Word, Measurement of Interfacial Processes at Electrode Surfaces with the Electrochemical Quartz Crystal Microbalance, Chem. Rev., vol. 92, pp.1355-1379, 1992.

52 A. Janshoff, H.-J. Galla and C. Steinem, Piezoelectric Mass-Sensing Devices as Biosensors - An Alternative to Optical Biosensors?, Angew. Chem. Int. Ed., vol.39, pp. 4004-4032, 2000.

53 K. A. Marx, Quartz Crystal Microbalance: A Useful Tool for Studying Thin Polymer Films and Complex Biomolecular Systems at the Solution-Surface Interface, Biomacromolecules, vol. 4, pp. 1099 -1120, 2003.

54 A. D. Ballato and R. Bechmann, Effect of Initial Stress in Vibrating Quartz Plates, Proc. IRE, Vol. 48, pp. 261-262, 1960.

55 A. Ballato, E. P. EerNisse and T. Lukaszek, The force–frequency effect in doubly rotated quartz resonators, 31st Annual Symposium on Frequency Control, pp.8-16, 1977.

56 J. M. Ratajski, Forced-frequency coefficient of singly-rotated vibrating quartz crystals, IBM J. Res. Dev., vol. 12, pp. 92–96, 1968.

57 P. C. L. Lee, Y. S. Wang, and X. Markenscoff, High frequency vibrations of crystal plates under initial stresses, J. Acoust. Soc. Am., vol. 57, pp. 95-105, 1975.

58 P. C.Y. Lee, Y. S. Wang, and X. Markenscoff, Nonlinear effects of initial bending on the vibrations of crystal plates, J. Acoust. Soc. Am., vol. 59, pp. 90-96, 1976.

59 L. D. Clayton and E. P. EerNisse, Frequency shift calculations for quartz resonators, Proc. 45th Annu. Symp. Freq. Contr., pp. 309–320, 1991.

60 Z. Wang, Y. Dong, H. Zhu, and G. Feng, Effect of Transverse Force on the Performance of Quartz Resonator Force Sensors, IEEE Transactions on Ultrasonics, Ferroelectrics, and Frequency Control, vol. 51, pp. 470-476, 2004.

61 B. Jakoby, H. Eisenschmid, and F. Herrmann, The Potential of Microacoustic SAW and BAW-Based Sensors for Automotive Applications—A Review, IEEE Sensors Journal, Vol. 2, No. 5, pp.443-452, 2002.

62 E. P. EerNisse, and R. B. Wiggins, Review of Thickness-Shear Mode Quartz Resonator Sensors for Temperature and Pressure, IEEE Sensors Journal, Vol. 1, No. 1, pp. 79-87, 2001.

63 H. Edward Karrer, and J. Leach, A Quartz Resonator Pressure Transducer, IEEE Transaction on Industrial Electronics and Control Instrumentation, Vol. IECI-16, No. 1, July 1969.

64 B.J. Chung, A.M. Robertson, D.G. Peters, et al., The numerical design of a parallel plate flow chamber for investigation of endothelial cell response to shear stress, Computers and Structures, Vol. 81, pp. 535–546, 2003.

65 C.-S. Yih, Fluid Mechanics, corrected ed., West River Press, Ann Arbor, MI, 1979.

66 H. F. Tiersten, Perturbation theory for linear electroelastic equations for small fields superposed on a bias, J. Acoust. Soc. Am., vol. 64, pp. 832–837, 1978.

67 J. Yang and S. Guo, An estimate on the second-order normal acceleration sensitivity of a quartz resonator, IEEE Trans. Ultrason., Ferroelect. Freq. Contr., vol.53, pp. 1562-1563, 2006.

68 D. Janiaud, L. Nissim and J.-J. Gagnepain, Analytical calculation of initial stress effects on anisotropic crystals: application to quartz resonators, 32nd Annual Symposium on Frequency Control, pp. 169–179, 1978.

69 S. Timoshenko and S. Woinowsky-Krieger, Theory of Plates and Shells, 2nd ed., McGraw-Hill, New York, pp.55-56, 1959.

70 K. K. Kanazawa and J. G. Gordon II, Frequency of a Quartz Microbalance in contact with Liquid, Anal. Chem., vol. 57, pp. 1770-1771, 1985.

71 K. M. Lakin, G. R. Kline, R. S. Ketcham, and S. G. Burns, Thin film resonator based low insertion loss filters, IEEE Ultrasonic Symposium, pp. 371–376, 1986.

72 K. M. Lakin, Thin film resonators and filters, IEEE Ultrasonic Symposium, Vol. 2, pp. 895–906, 1999.

73 R. Weigel, D. P. Morgan, J. M. Owens, A. Ballato, K. M. Lakin, K.-y. Hashimoto, and C. C. W. Ruppel, Microwave Acoustic Materials, Devices, and Applications, IEEE Transactions on Microwave Theory and Techniques, vol. 50, pp. 738-749, Mar. 2002.

74 M. Ylilammi, J.Ella, M. Partanen, and J. Kaitila, Thin film bulk acoustic wave filter, IEEE Trans. Ultrason., Ferroelect., Freq. Contr., vol. 49, pp. 535-539, Apr. 2002.

75 H. P. L öbl, M. Klee, R. Milsom, R. Dekker, C. Metzmacher, W. Brand, and P. Lok,, Materials for bulk acoustic wave (BAW) resonators and filters, J. Eur. Ceram. Soc., vol. 21, pp. 2633-2640, 2001.

76 T. Nishihara, T. Yokoyama, T. Miyashita, and Y. Satoh, High performance and miniature thin film bulk acoustic wave filters for 5 GHz, Proc. IEEE Ultrason. Symp., vol. 1, pp. 969-972, 2002.

77 R. Lanz and P. Muralt, Solidly mounted BAW filters for 8 GHz based on AlN thin films, Proc. IEEE Ultrason. Symp., pp. 178–181, 2003.

78 D. Feld, K. Wang, P. Bradley, A. Barfknecht, B. Ly, R. Ruby, A High Performance 3.0 mm x 3.0 mm x 1.1 mm FBAR Full Band Filter for U.S. PCS Handsets, IEEE Ultrasonics Symposium, pp. 913-918, 2002.

79 H. Zhang and E. S. Kim, Micromachined Acoustic Resonant Mass Sensor, Journal of Microelectromechanical systems, vol. 14, 2005.

80 R. H. Wittstruck, X. Tong, N. W. Emanetoglu, P. Wu, Y. Chen, J. Zhu, S. Muthukumar, Y. Lu, and A. Ballato, Characteristics of MgxZn1-xO Thin Film Bulk Acousitc Wave Devices, IEEE Trans. Ultrason., Ferroelect., Freq. Contr., vol. 50, pp. 1272-1278, Oct. 2003.

81 T. Yanagitani, T. Nohara, M. Matsukawa, Y. Watanabe, and T. Otani, Characteristics of $(10\bar{1}0)$ and $(11\bar{2}0)$ Textured ZnO Piezofilms for a Shear Mode Resonator in the VHF-UHF Frequency Ranges, IEEE Trans. Ultrason., Ferroelect., Freq. Contr., vol. 52, pp. 2140-2145, Nov. 2005.

82 T. Yanagitani, N. Mishima, M. Matsukawa, and Y. Watanabe, Electromechanical Coupling Coefficient k_{15} of Polycrystalline ZnO Films with the c-Axes Lie in the Substrate Plane, IEEE Trans. Ultrason., Ferroelect., Freq. Contr., vol. 54, pp. 701-704, Apr. 2007.

83 S. Wu, Z. Lin, M. Lee, and R. Ro, Bulk acoustic wave analysis of crystalline plane oriented ZnO films, J. Appl. Phys., vol. 102, 2007.

84 F. Martin, M.-E. Jan, S. Rey-Mermet, B. Belgacem, D. Su, M. Cantoni, and P. Muralt, Shear Mode Coupling and Tilted Grain Growth of AlN Thin Films in BAW Resonators, IEEE Trans. Ultrason., Ferroelect., Freq. Contr., vol. 53, pp. 1339-1343, 2006.

85 F. Martin, M.-E. Jan, B. Belgacem, M.-A. Dubois, P. Muralt, Shear mode coupling and properties dispersion in 8GHz range AlN thin film bulk acoustic wave (BAW) resonator, Thin Solid Films, vol. 514, pp. 341-343, 2006.

86 C. Chung, Y. Chen, C. Cheng, and K. Kao, Synthesis and Bulk Acoustic Wave Properties on the Dual Mode Frequency Shift of Solidly Mounted Resonators, IEEE Trans. Ultrason., Ferroelect., Freq. Contr., vol. 55, pp. 857-864, 2008.

87 Q. Chen, F. Li, H. Cheng, and Q. Wang, Characteristics of dual mode AlN thin film bulk acoustic wave resonators, IEEE Int. Freq. Control Sym., pp.609-614, 2008

88 H. F. Tiersten, Linear Piezoelectric Plates Vibrations, New York: Plenum Press, 1969.

89 B. A. Auld, Acoustic Fields and Waves in Solids, vol. 1, New York: John Wiley & Sons. Inc., 1973.

90 G. Carlotti, G. Socino, A. Petri, and E. Verona, Elastic Constants of Sputtered ZnO Films, IEEE Ultrasonic Symposium, pp. 295-300, 1987.

91 J. F. Rosenbaum, Bulk Acoustic Waves Theory and Devices, Artech House, 1988.

92 K. Tsubouchi, K. Sugai, N. Mikoshiba, AlN Material Constants Evaluation and SAW Properties on AlN/Al2O3 and AlN/Si, IEEE Ultrasonic Symposium, pp. 375-380, 1981.

93 R. P. O'Toole, S. G. Burns, G. J. Bastiaans and M. D. Porter, Thin aluminum nitride film resonators: miniaturized high sensitivity mass sensors, Anal. Chem., vol. 64, pp. 1289–1294, 1992.